Turbulence in the scrape-off layer of double-null tokamak configurations

Carrie Fiona BEADLE

■ École
polytechnique
fédérale
de Lausanne

2021

Abstract

 Understanding the turbulent dynamics in the outermost region of the tokamak is essential to predict and control the heat and particle loads to the vessel wall, a crucial problem for the entire fusion program. In this thesis, the problem is approached via two-fluid simulations run with the GBS code. We leverage a recent code upgrade to employ coordinate systems independent of the magnetic geometry, allowing the simulation of diverted configurations. We focus on double-null magnetic configurations. A double null configuration is being considered for DEMO due to its practical advantages of spreading the heat load over more strike points than a single null configuration, having a quiescent high field side on which heating antennas can be placed and the possibility to radiate more heat in detached scenarios. From a theoretical point of view, it is simpler to analyse than a single null because the high and low field sides are topologically separated.

Simulations with a balanced double null configuration are run for a range of resistivities and safety factors. The results are used to study the density decay at the outer midplane. A double decay length is observed and a model to predict the two decay lengths is developed. The decay length of the near scrape-off layer is well described as the result of transport driven by a non-linearly saturated ballooning instability, while in the far scrape-off layer the density decay length is described using a model of intermittent transport mediated by blobs. The analytical estimates of the decay lengths agree well with the simulation results and typical experimental values and can therefore be used to guide tokamak design and operation.

Unbalanced double null configurations are then simulated using a new elliptical coordinate system developed for this purpose, allowing more realistic elongation of the magnetic field. The distribution of the heat flux between the four divertor legs is calculated and compared to previous experimental results. We explain the heat flux sharing in terms of the $E \times B$, diamagnetic and parallel flows.

Key words: plasma physics, nuclear fusion, fluid simulations, scrape-off layer, plasma turbulence, plasma transport

Résumé

La compréhension de la dynamique de la turbulence dans la région périphérique du to-kamak est essentielle pour prévoir et contrôler la charge thermique et de particules sur le mur interne du tokamak, un problème crucial pour l'ensemble du programme de fusion. Dans cette thèse, le problème est abordé par des simulations à deux fluides réalisées avec le code GBS. Pour cela, nous utilisons une nouvelle version du code qui est basée sur des systèmes de coordonnées indépendants de la géométrie magnétique, ce qui permet de simuler des configurations dites 'diverted'. Nous nous concentrons sur les configurations magnétiques double-nul. Une configuration double-nul est envisagée pour DEMO en raison de ses avantages pratiques, à savoir la répartition de la charge thermique sur un plus grand nombre de points d'impact qu'une configuration simple-nul, le côté de haut champ inactif sur lequel les antennes de chauffage peuvent être placées, et la possibilité de rayonner plus de chaleur dans des scénarios détachés. D'un point de vue théorique, la configuration double-nul est plus simple à analyser que la configuration simple-nul, car le côté de champ haut est topologiquement séparé du côté de champ bas.

Des simulations avec une configuration double-nul équilibrée sont effectuées pour des valeurs différentes de résistivités et de facteurs de sécurité. Les résultats sont utilisés pour étudier la décroissance de la densité au niveau du plan médian extérieur. Une double longueur de décroissance est observée et un modèle permettant de prévoir les deux longueurs de décroissance est développé. La longueur de la décroissance de la couche d'arrachement proche est bien décrite comme le résultat d'un transport produit par une instabilité ballonnée non linéairement saturée, tandis que dans la couche d'arrachement lointaine, la longueur de la décroissance de la densité est décrite à l'aide d'un modèle de transport intermittent causé par des filaments de plasma. Les estimations analytiques des longueurs de décroissance concordent bien avec les résultats des simulations et les valeurs expérimentales typiques, et peuvent donc être utilisées pour la conception et le fonctionnement du tokamak.

Les configurations double-nul déséquilibrées sont ensuite simulées à l'aide d'un nouveau système de coordonnées elliptiques développé à cet effet, permettant un allongement plus réaliste du champ magnétique. La répartition du flux de chaleur entre les quatre branches du déflecteur est calculée et comparée à des mesures expérimentales. Nous expliquons le partage du flux de chaleur en termes de flux $E \times B$, diamagnétique et parallèle.

Mots clefs : physique des plasmas, fusion nucléaire, simulations fluides, scrape-off layer, transport turbulent

Contents

1 Introduction

1.1 The energy problem

Energy, both in the form of electricity and fuels is fundamentally important to society. Global energy consumption, nowadays mostly provided by fossil fuels, is expected to increase by almost 50% between 2018 and 2050 [43], due largely to improving living standards, especially in developing countries. In addition to reserves of fossil fuels being limited, the driving of climate change by carbon dioxide emissions calls urgently for alternative energy sources to be developed. The alternatives fall broadly into three categories: renewables, nuclear fission and nuclear fusion, and the best solution will probably involve a combination of all three.

The most promising renewable energy technologies are based on the exploitation of wind, sunlight, rainfall or geothermal heat. While their supply will (practically) never be exhausted, they require a lot of land and supply electricity intermittently. To illustrate the former drawback, we borrow an example from the highly insightful Ref. [15], that claims concentrated solar power in deserts (using mirrors to focus light onto solar photovoltaic panels) provides the best land and cost efficiency of the leading renewable energy technologies. Using this technology to supply the population of Europe and North Africa with power equal to current European consumption would require a total land area of $340,000$km^2, an area roughly the size of Germany. This is not impossible - the author suggests breaking it up into 65 plants about the size of Greater London - but it is clear the required infrastructure would be vastly more extensive than typical power plants today. To take another example, the energy density of an onshore wind farm is about $2W/m^2$. This means that to supply the power of a typical nuclear power station (1GW) requires an area of 500km^2; in Vaudoise terms a square of side length Lausanne-Vevey. Of course in Switzerland, hydroelectric power is a more attractive and energy dense alternative to wind, but we are geographically lucky! The second major drawback of renewables is their intermittency, that is, solar panels do not generate anything at night and the wind can be calm for days at a time. Possible solutions include hydroelectric pumped storage and charging electric car batteries at times of surplus, which are again possible but require significant development of infrastructure, land use and raw materials.

The principle of nuclear fission is to harness the energy released when a large atomic nucleus splits into smaller nuclei. Nuclear fission fuel is orders of magnitude more energy dense than releasing energy from fossil fuels by burning, but the supply is still limited. The world's current land-based sources of uranium are expected to last only 100 years if the nuclear fission was the sole power source with current (non-breeder) technology [3]. However, breeder reactors and extracting uranium from seawater could solve this problem. The main limitations of nuclear fission as a power source are the production of long-lived radioactive waste, risk of nuclear proliferation and popular opposition.

1.2 Fusion Energy

Fusion energy eliminates all the intermediate energy transitions involved in renewable energy sources: rather than generating electricity from a process ultimately driven by the Sun, it is developed around the idea of creating our own miniature Sun here on Earth and generating electricity from that. More concretely, the reactions powering the Sun are fusion reactions: two light nuclei join to make one heavier nucleus, releasing energy in the process. This process is difficult to achieve because the electromagnetic repulsion between two positively charged nuclei dominates the attractive strong nuclear force until the two nuclei are very close. Hence the colliding nuclei must approach each other at very high speeds to overcome the electromagnetic repulsion. The most promising approach to solving this problem is to heat the fuel gas so that the thermal energy of the nuclei is very high. The exact temperature required for fusion depends on the particular fusion reaction, the easiest of which is deuterium-tritium (D-T) fusion

$$\ce{^2_1D} + \ce{^3_1T} \rightarrow \ce{^4_2He} \text{ (3.5 MeV) } + \ce{^1_0n} \text{ (14.1 MeV)} \tag{1.1}$$

for which the rate of fusion-producing collisions peaks at approximately 100 keV. This reaction releases $\sim 350\,\text{GJ}$ per gram of fuel, compared to $\sim 40\,\text{kJ}$ per gram of fossil fuels. In fact, everyone in the world could be supplied with energy for 100 million years using D-T fusion making use of the available resources on Earth [3]. No greenhouse gases are produced in this process, nor any radioactive waste. The confinement vessel is radioactively activated by the energetic neutrons, however with the proper choice of materials it becomes safe after roughly 100 years, compared to the millions of years for which fission waste must be safely stored. Further, since fusion is not a chain reaction, there is no risk of meltdown and neither the fuel (hydrogen) nor waste product (helium) is dangerous or presents proliferation risks. Unlike renewables, fusion power promises to be reliable, controllable and take up relatively little space. These advantages have motivated decades of research effort to develop a working reactor.
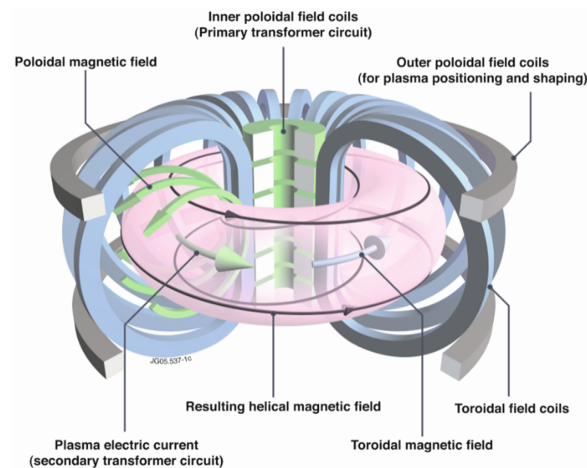
Figure 1.1 – Schematic diagram of a tokamak showing the current coils and magnetic field. Image source: Eurofusion.

1.3   The Tokamak Scrape-Off Layer

Atoms of gas heated to fusion temperatures lose their electrons and become plasma. Since charged particles orbit around magnetic field lines due to the Lorentz force, a magnetic field can be used to confine the plasma; this is the key principle of a tokamak.

The tokamak vessel has a toroidal shape, within which a near vacuum must be maintained to avoid the hydrogen nuclei losing energy via collisions with other species. The helical magnetic field is generated by three sets of current-carrying coils, as shown in Fig. 1.1. The inner poloidal field coils drive a toroidal current in the plasma via transformer action. This heats the plasma and creates the poloidal component of the magnetic field. The toroidal component of the magnetic field, which is greater, is generated by the toroidal field coils. Finally, the outer poloidal field coils are used to adjust the plasma position and shape.

Based on the magnetic field, the tokamak can be divided into two regions: the closed flux region in which magnetic field lines trace out closed toroidal surfaces and the Scrape-Off Layer (SOL) where the field lines intersect the vessel wall. The flux surface dividing the two regions is referred to as the Last Closed Flux Surface (LCFS). The SOL can be in either a limited or diverted configuration. In a limited configuration, a physical barrier protrudes across the flux surfaces and defines the LCFS. In a diverted configuration, shaping coils divert the magnetic field lines, generating one or more X points in the magnetic field; these are locations where the poloidal magnetic field vanishes. The advantage of this configuration over the simpler limiter technique is that the closed flux surfaces are kept well away from any material surface, reducing the impurity level within the closed flux region and improving the plasma confinement. In this configuration, the region in which plasma is in contact with the vessel wall is known as the divertor. In the SOL, the plasma outflowing from the closed flux region is scraped off (hence its name) by the flow along the magnetic field lines. The width of the SOL is
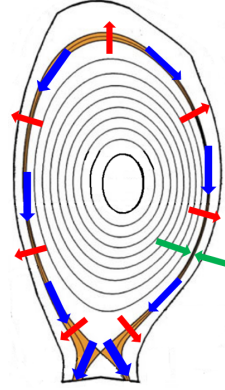
Figure 1.2 – Poloidal cross-section of a tokamak showing the location of the Scrape-Off Layer (yellow) and the main plasma flows. Blue arrows indicate the projection of the parallel flow towards the vessel wall, which is balanced by turbulent outflow from the closed flux region indicated by the red arrows. The green arrows indicate the SOL width, which is typically 1mm-1cm.

determined by the balance between parallel flow and turbulent plasma transport across the magnetic field lines. Since plasma parallel velocity is much higher than the cross field velocity, the SOL is thin compared to the rest of the plasma, typically 1mm-1cm thick (Fig. 1.2).

The SOL has an importance for tokamak operation out of proportion to its size: it is responsible for fuelling the plasma and removing the helium ash, as well as determining the impurity level. It also plays a role in the overall confinement of the plasma. Most importantly, the width of the SOL determines the power exhaust: the heat load onto the wall tiles in contact with the plasma, which is one of the critical issues facing ITER and DEMO [93],[48], [103]. Empirical extrapolations predict that the heat may be exhausted over a narrow region just 1mm thick, exceeding the heat flux limit of 5MW/m^2 required to avoid material damage to the wall [53].

Whilst the lower temperatures in the SOL (a few 10s of eV compared to around 100 keV in the core) allow easier access of experimental diagnostics such as Langmuir probes and Gas Puff Imaging, numerical simulations are still necessary for the understanding of the plasma dynamics in this region. A range of approaches exists for such simulations, from the phenomenological modelling on which ITER predictions are based [46], through two-fluid models including the one used in this thesis [69], [78], [36], [92], [91], [19], [100], [35], to high-fidelity, highly expensive gyrokinetic modelling [89], [88], [13], [66], [17]. Two-fluid models are generally based on the drift-reduced Braginskii equations (DRBE). First derived by Braginskii [9], the equations in their original form describe dynamics on timescales from the electron cyclotron frequency to the tokamak confinement time and length scales from the electron gyroradius to the machine size. Zeiler [98] simplified the Braginskii equations under what is known as the drift reduced approximation. The DRBE are suitable for numerical implementation and constitute an ideal framework to study the plasma dynamics in the SOL.

1.4 SOL Modelling with the drift-reduced Braginskii equations

Many groups use the DRBE to study the SOL plasma dynamics, using codes such as BOUT++ [78], [19], TOKAM3X [92], GRILLIX [91], GBD[100], HESEL [65] and GBS, the simulation tool used in this thesis [69],[36], [74]. The work carried out at the Swiss Plasma Center using the GBS code [69], [36], [74] has focused on developing predictive models for the SOL width and can be summarised as follows. Until recently, first-principles fluid modelling of the SOL has been carried out only for limited configurations, which can be simulated using a coordinate grid aligned to the magnetic field. In this configuration, the density and temperature decay in the SOL have been interpreted using a model based on the growth and saturation of linear instabilites, in particular drift waves and ballooning modes. In Ref. [58] the linear instabilities of the tokamak configuration are studied numerically and analytically from the linearised DRBE, to identify the dominant linear instability as a function of the safety factor, magnetic shear and parallel resisitivity. The instability saturation mechanism was studied in Ref. [75] and removal of the driving background gradient found to be the saturation mechanism in typical tokamak conditions. This analysis of the linear instability together with the gradient removal saturation mechanism is used in Ref. [59] to identify the instability dominating the transport as a function of the same parameters, and hence predict the self-consistent pressure decay length. In Ref. [56] this study is extended to include finite ion temperature effects. Taking the resistive-ballooning mode regime, which is the case for typical limited tokamak parameters, an analytical model was developed and validated against an extensive set of simulations and experimental measurements [39], [38]. This study was extended in Ref. [77] to study the effect of non-circularity of flux surfaces on the instability regimes, in particular the effect of finite aspect ratio, Shafranov shift, elongation and triangularity. It was found that elongation and negative triangularity stabilise the resistive ballooning mode, shortening the pressure decay length.

The simulation domain was then extended to include part of the closed flux region, allowing theoretical study of a narrow heat flux feature close to the LCFS, where the density and temperature gradient is much steeper than further into the SOL. The difference was ascribed to strong shear flow near the LCFS that suppresses the growth of instabilities in this region, so the transport is dominated by turbulent structures generated in the confined region that propagate across the SOL at a velocity determined from the balance of parallel and perpendicular electric currents [37].

Magnetic X points cannot be simulated using a single coordinate grid aligned to the magnetic field [69], presenting a significant difficulty for their simulation. Only recently have solutions to this problem been developed. The GBS approach is to use a fully geometric coordinate grid [69]. This version of the code has been used to valid a theoretical model of blob propagation [68] and following a further upgrade has been used to study the heat flux distribution in snowflake configurations [34]. Other solutions exist. TOKAM3X [92] uses flux coordinates with domain decomposition to treat the X point. The code has been used to study the impact of divertor leg length [32] and midplane flux expansion [30] on the turbulent transport; the

role of large scale and small scale ExB flow and grad B drift in creating poloidal assymetry in the parallel flow [29], the impact of a diverted configuration with respect to a limited configuration on the isothermal turbulence and transport [31] and the properties of energy turbulent structures and heat transport [4]. The TOKAM3X code has also been coupled to the Monte Carlo neutral particle solver EIRENE [24] to study the effect of turbulent fluctuations on the transport of neutral particles [23].

BOUT++ is a modular code that can simulate in principle any set of fluid equations in curvilinear coordinates [18]. The STORM module is a two fluid plasma model used for the study of blobs [21], [20], [96], which has recently been extended to include neutrals [86]. Like TOKAM3X, flux aligned coordinates are used [85].

The GRILLIX code [91] uses coordinates independent of the magnetic flux, with a cylindrical or cartesian grid and standard finite difference methods for the perpendicular operators. The parallel operators are handled using a field-line following and interpolation procedure [41]. The code has been used to compare the characteristics of the turbulence [90] and Reynolds stress [52] between diverted and limit geometries, and the effect of the Boussinesq approximation has been studied in slab, limited and diverted geometries [82], [90], [81], [99]. Finally the code has been adapted and used to study advanced divertor configurations [6].

However, as yet, no attempt has been made to bring together these insights, as well as other work on blob transport [62] [83] [22], [97] [25], to develop a predictive model of the transport and SOL width in diverted configurations.

1.5 Outline of current work

Among the attempts to develop numerical tools to simulate the plasma turbulence in diverted configurations, the GBS code was recently upgraded to allow the simulation of the diverted SOL, using a geometric coordinate system entirely independent from the magnetic field (Fig. 1.3), placing minimal constraints on its form, which is specified via the flux function. In this thesis, we leverage the extensive numerical work detailed in Ref. [69] to provide physics insight into the diverted SOL, making significant progress towards providing predictive capability of the heat load to the divertor plates. We focus in particular on Double Null (DN) magnetic configurations. DN configurations are of interest because the four strike points provide greater opportunity to spread the heat load to the wall, the two X points may allow greater radiative heat losses and the quiescent High Field Side (HFS) allows heating antennas to be placed there safe from heat damage, hence the DN configuration is being considered for DEMO [73], [47]. It also provides an ideal setting for advancing the first numerical investigation of the plasma dynamics in diverted configurations because of the topological seperation between the HFS and Low Field Side (LFS).

In Chapter 2, the version of the GBS code used in this thesis is described. We outline the derivation of the DRBE from the kinetic equation, and their drift-reduction to obtain the form
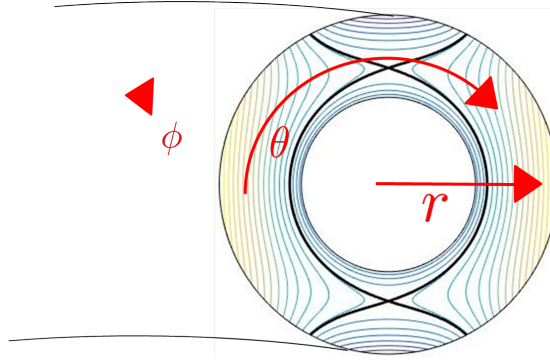
Figure 1.3 – Circular geometric coordinate system used in GBS. The coordinate directions are shown in red: r is the radial coordinate, θ the poloidal coordinate and ϕ the toroidal coordinate. The flux surfaces are shown in colour and the LCFS in black.

implemented in the code. The implementation of the magnetic field via the geometric operators in the geometric coordinate system, as well as the boundary conditions and numerical approach, are explained.

In Chapter 3 we study the turbulence and transport in balanced Double Null magnetic configurations. First, the geometric operator expressions in a circular-toroidal coordinate system are derived, then we present the main results of the first GBS simulations in a double null configuration. The striking HFS-LFS asymmetry of interest for the placement of heating antennas is discussed in terms of the ballooning instability driving the turbulence. The up-down asymmetry is investigated by the time averaging of Ohm's law and the parallel resistivity is found to have a significant effect, in contrast to earlier work [50] where it was neglected.

We then focus on the density decay on the LFS of the tokamak. This is a key element in the prediction of the heat load to the divertor plates, one of the most critical issues for the operation of ITER and design of DEMO [48], [93], [103]. It is also important in determining the wall recycling, wall erosion and impurity influx. We find a double decay length, as observed in experiments [47], [78], [45], [12], [42]. The decay length of the near SOL is well described by transport driven by a non-linearly saturated ballooning instability, whilst the far SOL density decay length is described using a model of intermittent transport mediated by blobs.

In Chapter 4, we look at the effect of magnetic inbalance on the plasma transport. We first describe the modifications to GBS to make the domain more elongated, allowing the study of more realistic magnetic equilibria. In particular, a new elliptic-toroidal coordinate system, the derivation of the geometric operators in this system and the numerical verification of their implementation in the GBS code are described. We present the results of three simulations with different magnetic configurations: an unbalanced double null in which the LCFS forms an upper single null, a balanced double null and an unbalanced double null in which the LCFS forms a lower single null. The heat distribution between the four strike points is compared between the three configurations and interpreted in terms of the equilibrium fluxes.

Finally, the work of the present thesis is summarised and conclusions presented in Chapter 5.

2 | Drift Reduced Braginskii Equations and the GBS Code

2.1 Introduction

In this Chapter the physical model and the simulation tool used in this thesis - that is the Drift Reduced Braginskii Equations (DRBE) and their implementation in the GBS code - are described. The derivation of the Braginskii fluid equations from the Boltzmann kinetic equation is outlined. We then consider the limit of low frequency (with respect to the ion cyclotron frequency) and large scale (with respect to the ion cyclotron radius) fluctuations, i.e. the drift ordering, obtaining the set of DRBE. This set of equations is implemented in the GBS code, which has been developed in the last decade at the Swiss Plasma Center. GBS is the ideal tool to carry out the simulations of the double-null configurations described in the rest of the thesis.

In Section 2.2 the derivation of the physical model is outlined and the physical hypotheses behind it are described. In Section 2.3 details of the numerical implementation are given, comprising the geometry, numerics and boundary conditions.

2.2 The drift-reduced Braginskii equations

The most complete description of a plasma is given by the distribution function, $f(t, \mathbf{x}, \mathbf{v})$, of each particle species making up the plasma, which evolve according to the Boltzmann equation:

$$\frac{\partial f}{\partial t} + \nabla \cdot (\mathbf{v} f) + \nabla \cdot \left(\frac{\mathbf{F}}{m} f \right) = C \tag{2.1}$$

where $\mathbf{F} = q(\mathbf{E} + \frac{1}{c}\mathbf{v} \times \mathbf{B})$ is the Lorentz force, q is the particle charge, m is the particle mass and C is the collision operator. Collisions force the velocity distribution towards a Maxwellian, so for a sufficiently collisional plasma, such as in the case of the tokamak boundary, the velocity

dependence of f does not merit evolving the full six dimensional distribution function. It is more practical to consider the evolution of the first three moments of the distribution functions: the density,

$$n(\mathbf{x}, t) = \int f(\mathbf{x}, \mathbf{v}, t) d\mathbf{v}, \tag{2.2}$$

momentum,

$$n(\mathbf{x}, t)\mathbf{V}(\mathbf{x}, t) = \int \mathbf{v} f(\mathbf{x}, \mathbf{v}, t) d\mathbf{v}, \tag{2.3}$$

and temperature,

$$T(\mathbf{x}, t) = \frac{1}{n} \int \frac{m}{3} (\mathbf{v} - \mathbf{V})^2 f(\mathbf{x}, \mathbf{v}, t) d\mathbf{v} \tag{2.4}$$

of each species. The density evolution equation is found by taking the first moment of Eq. (2.1),

$$\frac{\partial n}{\partial t} + \nabla \cdot (n\mathbf{V}) = 0, \tag{2.5}$$

and analogous equations are derived for the evolution of $\mathbf{V}$ and T by taking the second and third moments of Eq. (2.1). In Eq. (2.5), the evolution of the first moment, n, is linked to the scond moment, $n\mathbf{V}$. This is a general issue known as the closure problem: the equation for the evolution of the nth moment contains the $(n+1)^{\text{th}}$ moment, so to obtain a closed system the $(n+1)^{\text{th}}$ moment must be expressed in terms of the moments of order n and lower. The Braginskii closure is based on the assumption that the velocity distibutions of the particle species are close to Maxwellian, since the collisionality is high, and that since the deviations from a Maxwellian distribution are due to the presence of spatial and temporal gradients, the higher moments can be expressed as proportional to n, $\mathbf{V}$, T and their gradients. The full derivation of the Braginskii equations is found in Ref. [9]. GBS uses the strong magnetic field case of Braginskii's equations.

The Braginskii equations encapsulate the plasma dynamics on timescales from the cyclotron frequencies to the confinement time and from the Larmor radii to the machine size. Since they are computationally too demanding, Zeiler et. al. [98], [87] proposed to use the drift ordering

for the length and timescales of typical SOL phenomena:

$$\frac{\partial}{\partial t} \sim \mathbf{v}_{E \times B} \cdot \nabla \sim \frac{\rho_s^2}{L_\perp^2} \omega_i \ll \omega_i \qquad (2.6)$$

where $\rho_s = c_s / \omega_i$ is the ion sound speed Larmor radius, that is, the ratio between the sound speed and ion cyclotron frequency, and

$$\mathbf{v}_E = (-\nabla \phi \times \mathbf{b}) \frac{c}{B} \qquad (2.7)$$

is the $E \times B$ drift velocity. This ordering allows us to decompose the ion and electron velocities

$$\mathbf{V}_e = \mathbf{v}_E + \mathbf{v}_{*e} + v_{\|e} \mathbf{b} \qquad (2.8)$$
$$\mathbf{V}_i = \mathbf{v}_E + \mathbf{v}_{*i} + \mathbf{v}_{pol} + v_{\|i} \mathbf{b} \qquad (2.9)$$

where

$$\mathbf{v}_{*s} = (-\mathbf{b} \times \nabla p_s) \frac{c}{enB} \qquad (2.10)$$

is the diamagnetic drift velocity for species s and

$$v_{\|s} = \mathbf{b} \cdot \mathbf{V}_s \qquad (2.11)$$

is the velocity in the magnetic field direction. The $E \times B$ and diamagnetic drift velocities constitute the approximation to the perpendicular drift velocity in the limit of vanishing Larmor radius. For the electrons, this approximation is sufficient, but ions have a larger

Larmor radius so the first order correction to their drift velocity,

$$
\begin{aligned}
\mathbf{v}_{pol} = & \frac{\mathbf{b}}{\omega_i} \times \frac{d\mathbf{V}_{\perp i0}}{dt} + \frac{1}{nm_i\omega_i}\Big\{ \mathbf{b} \times \Big[p_i \Big(\nabla \times \frac{\mathbf{b}}{\omega_i} \Big) \cdot \nabla \mathbf{V}_{\perp \mathbf{i0}} \Big] \\
& + \mathbf{b} \times \nabla_\perp \Big[\frac{2p_i}{\omega_i} \nabla \cdot \mathbf{b} \times \mathbf{V}_{\perp i0} \Big] - \nabla_\perp \Big[\frac{p_i}{2\omega_i} \nabla_\perp \cdot \mathbf{V}_{\perp i0} \Big] \Big\} \\
& + \frac{1}{nm_i\omega_i}\mathbf{b} \times \Big[G_i\kappa - \frac{\nabla G_i}{3} \Big],
\end{aligned}
\tag{2.12}
$$

must be included, where

$$
\kappa = \mathbf{b}\cdot\nabla\mathbf{b}
\tag{2.13}
$$

is the magnetic field curvature and the gyroviscous terms, $G_{i,e}$ are

$$
G_e = -\eta_{0,e}\left(2\nabla_\parallel v_{\parallel,e} - \frac{C(p_e)}{Bn} + \frac{C(\phi)}{B} \right)
\tag{2.14}
$$

$$
G_i = -\eta_{0,i}\left(2\nabla_\parallel v_{\parallel,e} + \tau\frac{C(p_i)}{Bn} + \frac{C(\phi)}{B} \right),
\tag{2.15}
$$

with $\eta_{0,e,i}$ constant coefficients. These terms are neglected in this thesis, since it can be shown that $\nabla\cdot(n\mathbf{v}_{pol}) \ll \nabla\cdot(n\mathbf{v}_{E\times B})$ [55].

The detailed derivation of the the set of equations we consider for the present study is given in Ref. [55]. Here, we briefly summarize this derivation.

The plasma is assumed to be quasineutral, $n_i = n_e \equiv n$, thus we consider the electron continuity equation:

$$
\frac{\partial n}{\partial t} + \nabla\cdot[n(\mathbf{v}_E + \mathbf{v}_{*e} + \mathbf{v}_{\parallel e})] = 0.
\tag{2.16}
$$

The electrical potential, ϕ is evolved via the vorticity $\omega = \nabla_\perp^2\phi$, which is determined by subtracting the electron and ion continuity equations:

$$
-\frac{nc}{B\omega_i}\left(\frac{\partial\omega}{\partial t} + \mathbf{v}_{\parallel i}\cdot\nabla\omega \right) + \frac{1}{3m_i\omega_i}\mathbf{b} \times \kappa\cdot\nabla G_i + \nabla_\parallel\frac{j_\parallel}{e} + \nabla\cdot n(\mathbf{v}_{*i} - \mathbf{v}_{*e}) = 0
\tag{2.17}
$$

where $j_\parallel = n(v_{\parallel i} - v_{\parallel e})$.

The electron and ion momentum equations are projected along the **b** direction to derive the equations for the parallel velocities

$$m_e \frac{d^e v_{\parallel e}}{dt} = -\frac{1}{n}\nabla_\parallel p_e - \frac{2}{3}\nabla_\parallel G_e + e\nabla_\parallel \phi + e\frac{j_\parallel}{\sigma_\parallel} - 0.71\nabla_\parallel T_e \tag{2.18}$$

$$m_i \frac{d v_{\parallel i}}{dt} = -\frac{1}{n}\nabla(p_i + p_e) - p_i \nabla \times \frac{\mathbf{b}}{\omega_i}\cdot\nabla V_{\parallel i} - \frac{2}{3}\nabla_\parallel G_i \tag{2.19}$$

where $d_t = \partial_t + (\mathbf{v}_E + v_{\parallel i}\mathbf{b})\cdot\nabla$ and $d_t^e = \partial_t + (\mathbf{v}_E + v_{\parallel e}\mathbf{b})\cdot\nabla$ and the electromagnetic fluctuations are neglected since the plasma β is small in the SOL. Finally the electron and ion temperature equations come from considering the drift ordering of Braginskii's temperature equation:

$$\frac{3}{2}n\frac{d^e T_e}{dt} = -\frac{3}{2}n\mathbf{v}_{*e}\cdot\nabla T_e - p_e\nabla\cdot(\mathbf{v}_{\perp e} + \mathbf{v}_{\parallel e})$$
$$+ \frac{5}{2}\frac{c}{e}\nabla\cdot p_e\left(\frac{\mathbf{b}}{B}\times\nabla T_e\right) + 0.71 T_e\nabla_\parallel j_\parallel + \nabla\cdot(\chi_{\parallel e}\nabla_\parallel T_e) \tag{2.20}$$

$$\frac{3}{2}n\frac{d T_i}{dt} = -T_i[n\cdot\nabla(\mathbf{v}_E + \mathbf{v}_{\parallel e}) + \nabla\cdot(n\mathbf{v}_{*e}) - \frac{5}{2}\frac{c}{e}p_i\left(\nabla\times\frac{\mathbf{b}}{B}\right)\cdot\nabla T_i \tag{2.21}$$

We now rewrite the the divergences of the $E\times B$, diamagnetic and parallel fluxes in a form suitable for numerical implementation.

The $\nabla\cdot(n\mathbf{v}_E)$ terms are evolved as

$$\nabla\cdot(n\mathbf{v}_E) = c\nabla n\cdot\left(-\nabla\phi\times\frac{\mathbf{b}}{B}\right) + cn\nabla\cdot\left(\nabla\phi\times\frac{\mathbf{b}}{B}\right) = \frac{c}{B}[\phi, n] + \frac{2cn}{B}C(\phi) \tag{2.22}$$

where

$$[\phi, n] = \mathbf{b}\cdot(\nabla\phi\times\nabla f) \tag{2.23}$$

is the Poisson bracket operator and

$$C(f) = \frac{B}{2}\left(\nabla\times\frac{\mathbf{b}}{B}\right)\cdot\nabla f \tag{2.24}$$

is the curvature operator.

The $\nabla \cdot (n\mathbf{v}_{*e})$ terms are evolved as

$$\nabla \cdot (n\mathbf{v}_{*e}) = -\frac{c}{e}(\nabla \times \frac{\mathbf{b}}{B}) \cdot \nabla p_e = -\frac{2c}{eB}C(p_e). \tag{2.25}$$

The $\nabla \cdot (n\mathbf{v}_{\parallel e})$ terms are evolved as

$$\nabla \cdot (n\mathbf{v}_{\parallel e}) = \nabla n \cdot \mathbf{v}_{\parallel e} + n\nabla \cdot \mathbf{v}_{\parallel e} = n\nabla_{\parallel} v_{\parallel e} + v_{\parallel e}\nabla_{\parallel} n. \tag{2.26}$$

where

$$\nabla_{\parallel} f = \mathbf{b} \cdot \nabla f \tag{2.27}$$

is the parallel gradient operator and $\nabla \cdot \mathbf{b}$ is neglected. This constitutes a neglect of finite aspect ratio effects.

In this thesis we consider the cold ion limit, $\tau = T_i/T_e = 0$. This assumption can have an effect on the stability of linear SOL modes [57], on the electrical potential structure near the LCFS [101] and on up-down asymmetry [102]. We neglect fluctuations in the magnetic field (electrostatic limit) and employ the Boussinesq approximation.

To summarise, the model equations in the dimensionless form we consider in the present thesis are

$$\frac{dn}{dt} = \frac{2}{B}[C(p_e) - nC(\phi)] - \nabla_{\parallel}(nv_{\parallel e}) + S_n + D_n\nabla_{\perp}^2 n \tag{2.28}$$

$$\frac{d\omega}{dt} = \frac{2B}{n}C(p_e) - v_{\parallel i}\nabla_{\parallel}\omega + \frac{B^2}{n}\nabla_{\parallel} j_{\parallel} + D_{\omega}\nabla_{\perp}^2 \omega \tag{2.29}$$

$$\begin{aligned}\frac{dT_e}{dt} = &\frac{4}{3B}\Big[\frac{7}{2}T_eC(T_e) + \frac{T_e^2}{n}C(n) - T_eC(\phi)\Big] \\ &+ \frac{2}{3}\frac{T_e}{n}0.71\nabla_{\parallel} j_{\parallel} - \frac{2}{3}T_e\nabla_{\parallel} v_{\parallel e} - v_{\parallel e}\nabla_{\parallel} T_e + S_{T_e} + D_{T_e}\nabla_{\perp}^2 T_e\end{aligned} \tag{2.30}$$

$$\frac{dv_{\parallel e}}{dt} = -v_{\parallel e}\nabla_{\parallel} v_{\parallel e} + \mu(\nabla_{\parallel}\phi - \frac{T_e}{n}\nabla_{\parallel} n - 1.71\nabla_{\parallel} T_e + \nu j_{\parallel}) + D_{v_{\parallel e}}\nabla_{\perp}^2 v_{\parallel e} \tag{2.31}$$

$$\frac{dv_{\parallel i}}{dt} = -v_{\parallel i}\nabla_{\parallel} v_{\parallel i} - \frac{1}{n}\nabla_{\parallel} p_e + D_{v_{\parallel i}}\nabla_{\perp}^2 v_{\parallel i} \tag{2.32}$$

where n, T_e, ϕ and $v_{\parallel e,i}$, B and t are normalized to n_0, T_{e0}, T_{e0}/e, c_{s0}, B_0 and R_0/c_{s0}, respectively, where n_0, T_{e0} and $c_{s0} = \sqrt{T_{e0}/m_i}$ are the reference density, electron temperature and

sound speed, B_0 and R_0 are the magnetic field strength and major radius at the magnetic axis. Perpendicular lengths are normalised to the ion sound Larmor radius $\rho_{s0} = c_{s0}/\omega_i$, with $\omega_i = eB_0/(cm_i)$, and parallel lengths normalised to R_0. The normalised resistivity is defined based on the Spitzer resistivity as $\nu = m_e R_0/(1.96 m_i c_{s0} \tau_e)$ where τ_e is the electron collision time. We use a constant resistivity across the domain, with no temperature dependence. We define $\mu = m_i/m_e$ and $\rho_* = \rho_{s0}/R_0$. The electron pressure is denoted $p_e = nT_e$ and dimensionless current $j_\parallel = n(v_{\parallel i} - v_{\parallel e})$. Using the Poisson bracket operator defined in Eq. (2.23), the convective derivative becomes $d_t f = \partial_t f + \rho_*^{-1}[\phi, f]$. Small diffusion operators are added for numerical stability.

To summarise, Eqs. 2.28- 2.32 employ the following assumptions:

- The parallel resistivity, ν is constant.

- $T_i = 0$.

- Equations are in the electrostatic limit, $\partial_t \psi = 0$.

- The Boussinesq approximation - $\frac{d}{dt}\nabla_\perp^2(n\phi) = n\frac{d}{dt}\nabla_\perp^2\phi$ - is used.

- Gyroviscous terms are neglected

The conversion between the normalised units n_0 and T_{e0} and physical units of density and temperature is most correctly derived from the source terms. That is, given the divergence of particle flux from experiments in units of $m^{-3}s^{-1}$ this must be matched to the simulation $S_n = \tilde{S}_n/(n_0/t_0) = \tilde{S}_n R_0/(n_0 c_{s0})$ where $\tilde{S}_n$ is the particle source in physical units and S_n is the particle source in GBS units. The same consideration applies for the heat flux, from which we find T_{e0} and hence c_{s0}. However, in practice, temperature data is much more readily available from experiments than heat or particle flux divergence, so we estimate ρ_{s0} by taking T_{e0} as the experimentally measured temperature at the LCFS.

The ion sound velocity is given by:

$$c_{s0} = 9.79 \cdot 10^5 \sqrt{\gamma T_e/\mu} \ \texttt{cm/sec} \tag{2.33}$$

Where γ is the adiabatic index, T_e is the electron temperature in [eV] and $\mu = m_i/m_p$ is the mass ratio between an ion and a proton. The ion gyrofrequency is given by:

$$\omega_i = 9.58 \cdot 10^3 ZB/\mu \ \texttt{rad/sec} \tag{2.34}$$

Where Z is the ion charge state and B is the magnetic field in Gaussian cgs units. Substituting in TCV-like parameters for a hydrogen plamsa - $T_{e0} = 45$eV, $B = 1.43$T and $\gamma = Z = \mu = 1$ - gives an approximation of $\rho_{s0} = 0.0479$ cm.

2.3   The GBS Code

For a given set of model equations, there exist a range of possibilities for their implementation. When fluctuations are small, it is common to evolve only the deviations from a pre-determined equilibrium. In a medium that is uniform over a certain length scale, it is common to simulate only a small sample of the area, with suitable boundary conditions such that the small area is representative of the whole. While these approximations are valid and often used in the study of plasma turbulence in the tokamak core, such simplifications are impossible in the SOL due to the fluctuations being of order unity and the existance of non-local phenomena such as propagating blobs.

The problem of solving these equations in the SOL has been approached using a number of codes, which differ in the approximations made to the DRBE, the boundary conditions and numerical schemes. These include BOUT++ [78], [19], TOKAM3X [92], GRILLIX [91], GBD[100] and GEMR [35].

The GBS code was developed to solve the set of equations in three dimensions treating the equilibrium profiles and plasma turbulence self consistently. It initially used a second order finite differences scheme and was used to study linear devices, such as LAPD, then Simple Magnetic Torus configurations, such as in TORPEX. The coordinate system was flux aligned, with coordinate directions x perpendicular to the flux surfaces, z the periodic toroidal coordinate and y the binormal coordinate such that the system was orthogonal [74].

Magnetic presheath boundary conditions were derived and implemented to correctly treat the boundary at the limiter [51]. The physical model was extended to include neutral atom physics, finite ion temperature, the addition of a closed field line region, and a non-Boussinesq treatment of the polarization drift [36]. Recently, the code was upgraded to implement a geometric coordinate system, independent from the magnetic field, that allows the study of diverted magnetic configurations [69], and a further upgrade allows the simulation of advanced divertor configurations [34].

The approach of GBS is that starting from an arbitrary initial state, constrained only to be consistent with the boundary conditions, the five fields n, T_e, ω, ϕ, $v_{\parallel e}$ and $v_{\parallel i}$ are evolved self-consistently according to Eqs. (2.28 - 2.32) with no seperation between equilibrium and fluctuations. The 3D simulation domain covers the full toroidal and poloidal angle and extends radially from a certain distance inside the LCFS, typically of the order $20\rho_{s0}$, up to the wall. The source terms are non-zero only within the LCFS and mimic plasma outflow from the core. Plasma losses to the wall are encapsulated by boundary conditions. Hence, starting from a uniform initial state, the fields evolve until a dynamic equilibrium state is reached in which the source input is balanced by the wall losses. We perform the physical analysis in this dynamic equilibrium state.

2.3.1   Geometry

The plasma fields are defined on a coordinate grid that is purely geometrical, independent from the magnetic field. We define our coordinate $[x, y, z]$ with x being the radial coordinate, y the poloidal coordinate and z the toroidal coordinate. More precisely, two different poloidal coordinate systems are used in this thesis. The first is the circular coordinate system, in which x is a linear rescaling of the minor radius r, and y a linear rescaling of the geometrical poloidal angle θ. This coordinate system is right handed and orthogonal. This coordinate system is used in Chapter 3 to perform balanced DN simulations. The second system is the elliptic system, which is non-orthogonal. In this system the x coordinate refers to an elliptic surface and y is a poloidal angle, defined in Chapter 4. The elliptic system is used to carry out simulations of unbalanced DN configurations.

The operators described in Eqs. (2.23-2.27) include a number of coefficients that depend on both the definition of the coordinate system and the magnetic field. We consider magnetic fields that are toroidally uniform and are specified by a flux function, $\psi(x, y)$, which is related to the magnetic field as

$$\mathbf{B} = F(\psi)\nabla z + \nabla z \times \nabla \psi(x, y) \tag{2.35}$$

from which we find the $\mathbf{b}(x, y)$ vector and $B(x, y)$ scalar in Eqs. (2.23-2.27). We simplify the operators by taking only the first order terms in a/R_0, $l_\perp/R_0$ and ρ_{s0}/R_0, where a is the tokamak minor radius and $l_\perp$ is the length scale of field gradients in the poloidal plane. This simplification is described fully in Ref. [67] and corresponds to taking the infinite aspect ratio limit. Removing this approximation was found to have a stabilising effet on ballooning modes in a limited configuration [44]. The magnetic field is defined such that the poloidal magnetic field component is a factor a/R_0 smaller than the toroidal field component, allowing further simplification using this ordering parameter [69].

2.3.2   Numerics

The spatial derivatives are evaluated using a fourth order finite differences method. For numerical stability, $v_{\parallel e}$ and $v_{\parallel i}$ are evolved on a grid displaced by $\Delta y/2$ and $\Delta z/2$ relative to the n, ϕ, ω, T_e grid, where Δx and Δy are the grid spacing in the poloidal and toroidal directions. The Poisson bracket is evolved according to an Arakawa scheme. To evaluate ϕ from ω, Poisson's equation is inverted using a direct solver method based on the MUMPS library [1], [2]. The timestepping is performed using a fourth order Runge-Kutta scheme.

The correct numerical implementation of Eqs. (2.28 - 2.32) is verified using the method of manufactured solutions, first adapted to plasma fluid codes in Ref. [79] and described for the version of GBS used in this thesis in Ref. [69].

The use of geometric coordinates requires a greater resolution in the toroidal direction than the one necessary in codes based on flux-aligned coordinates. Indeed, it must be checked for each magnetic configuration used that the local pitch angle nowhere exceeds more than two perpendicular grid spacings per toroidal grid spacing. If this requirement is not met, the parallel gradient operator is not correctly evaluated and the simulation will crash.

Other approaches exist for handling magnetic X points. TOKAM3X [92] and BOUT++ [78] retain the use of flux-aligned coordinates by decomposing the domain into a number of sub-domains and thus avoiding the coordinate singularity. Ghost cells are used to exchange information between the sub-domains. This method is less computationally expensive because less poloidal planes are required in each simulation, however, the coordinate grid suffers a loss of resolution where there is greater flux expansion at the X point. The GRILLIX [91] code, like GBS, uses a geometric grid, however the parallel gradient operator is treated using a field line following and interpolation method, which can be difficult to handle at the domain boundaries.

2.3.3   Boundary conditions

The simulations are periodic in the y direction but boundary conditions must be applied in the radial direction. At r_{max}, boundary conditions are applied at the magnetic pre-sheath, where the ion drift approximation breaks down and gradients in the direction perpendicular to the wall become large. These boundary conditions are derived and compared to kinetic simulations in Ref. [51] and have been properly adapted to be applied to to the diverted geometry in Ref. [69],

$$v_{\|i} = \pm\sqrt{T_e} \tag{2.36}$$

$$v_{\|e} = \pm\sqrt{T_e}\exp\left(\lambda - \phi/T_e\right) \tag{2.37}$$

$$\partial_x\phi = \mp\sqrt{T_e}\partial_x v_{\|i} \tag{2.38}$$

$$\partial_x n = \mp n/\sqrt{T_e}\partial_x v_{\|i} \tag{2.39}$$

$$\omega = -(\partial_x v_{\|i})^2 \mp \sqrt{T_e}\partial_{xx}^2 v_{\|i} \tag{2.40}$$

$$\partial_x T_e = 0 \tag{2.41}$$

The plus and minus signs refer to field lines entering and leaving the wall and $\lambda \approx 3$. Where the sign changes, a smoothing function is applied to avoid discontinuity [69].

At the inner radial boundary, we use an ad-hoc set of boundary conditions: $\partial_x f = 0$ for all fields f, except for ω and ϕ, for which we impose $\omega = 0$ and $\phi = \lambda T_e$. The ad-hoc inner boundary conditions have minimal effect in the region outside the source where our analysis is performed.

3 Density decay in the SOL of balanced double-null configurations

3.1 Introduction

Managing the heat load to the divertor is among the most critical issues for the operation of ITER and design of DEMO [48], [103] and identified by the European roadmap for the realisation of fusion energy as a possible showstopper for the entire program [93]. A first step towards a theoretical model of the heat flux is a prediction of the density decay in the SOL region, this is the subject of this chapter. Besides the heat flux, the density decay length also determines the wall recycling, impurity influx and wall erosion.

This Chapter is concerned with the density decay length in DN configurations and the results presented are the first study of density decay length carried out with GBS in diverted geometry. Looking at diverted rather than limited configurations is crucial because diverted configurations are used in the majority of present day experiments and will be used in ITER and DEMO. Certain aspects of the density decay such as the properties of the linear modes and blob propagation are significantly modified when going from limited to diverted configurations - for example due to the region of high flux expansion, topological separation of good and bad curvature regions, higher magnetic shear - making it necessary to study diverted configurations carefully and not simply extrapolate the results from limited configurations.

The density decay of the SOL cannot always be fitted by a single exponential decrease, in fact a double decay length is commonly observed in double null (DN) configurations, for example on C-Mod [47] and MAST [78] with a shorter decay length in the near SOL and a longer one in the far SOL. This is similar to observations in other magnetic configurations, such as the single null (SN) [45] [12] and limited configurations [42]. The different decay in the near and far SOL is the result of differences in the near and far SOL turbulence. Differences have been observed experimentally [37]. In the near SOL, turbulence is not intermittent, while in the far SOL intermittent events known as blobs have been detected and tracked [63], [68]. Our work represents a step forward building upon earlier single blob studies [61] and multiblob models [83], [22], [97].

We disentangle the different turbulent mechanisms at play in the SOL, in particular the nature of the fluctuations in the near and far SOL, the properties of blobs including their typical size, velocity and generation rate, and the parallel transport. Ultimately, our work allows the development of a predictive model for the density decay in DN configurations. The focus of the present chapter is on balanced DN configurations, meaning the two X points are on the same magnetic flux surface constituting the single separatrix. Configurations in which one X point is closer to the magnetic axis than the other and there are therefore two separatrices are referred to as unbalanced, these are considered in the next chapter.

This Chapter is an expanded version of Ref. [5]. First we describe the coordinate system and geometric operators used for the simulation of the balanced DN configuration in Section 3.2. In Section 3.3 we describe a set of simulations in which the resistivity and safety factor - the most important controls on the plasma dynamics - are varied. We highlight the main features of the results and discuss the asymmetry in the turbulence between the high field side (HFS) and low field side (LFS) and in the structure of the time and toroidally averaged fields around the upper and lower X points. In Section 3.4 we focus on the density decay at the outer midplane. In the near SOL, the turbulent radial flux is not intermittent, so we estimate the flux based on the development and saturation of a linear instability driven by the background radial gradient in density and temperature. We match the predicted flux, Γ, to the turbulent flux across the LCFS, Γ_{LCFS}, to find the near SOL density decay length. In the far SOL the fluctuation distribution is heavy-tailed, indicating intermittent turbulence and indeed observation of the simulation results reveals the presence of coherent structures of high plasma density (blobs) that propagate outwards due to their self-generated $\mathbf{E} \times \mathbf{B}$ velocity. We predict the blob-mediated flux using only the near SOL properties, from which we can derive the far SOL density decay length.

3.2   Coordinate system and geometric operators for the balanced DN configuration

For the simulations of the balanced DN configuration, we use a circular toroidal coordinate system (r, θ, ϕ), defined as,

$$
\begin{aligned}
r &= \sqrt{R_1^2 + Z^2} \\
\theta &= \arctan Z / R_1 \\
\phi &= \arctan Y / X
\end{aligned}
\tag{3.1}
$$

where (X, Y, Z) is a Cartesian system centred at the midplane of the major axis of the tokamak, R_0 is the major radius at the magnetic axis, $R = R_0 - r \cos\theta$ is the major radius, $R_1 = R_0 - R = r \cos\theta$ is the distance from the magnetic axis in the ∇R direction and a is the minor radius at the wall (see Fig. 3.1).
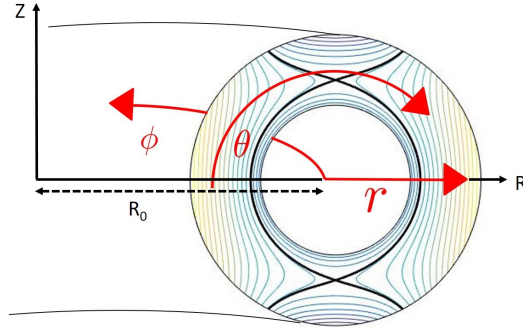
Figure 3.1 – Flux surfaces (colours) and coordinate directions (red) for the balanced double null configuration. The LCFS is shown by the thick black line. The hole around the magnetic axis is not physical, rather the Braginskii model is not valid in the core so we do not simulate that region.

The inverse transformation is

$$X = R\cos\phi$$
$$Y = R\sin\phi \tag{3.2}$$
$$Z = r\sin\theta.$$

The covariant basis vectors associated with the coordinates (r,θ,ϕ) are

$$e_r = \begin{pmatrix} -\cos\theta\cos\phi \\ -\cos\theta\sin\phi \\ \sin\theta \end{pmatrix} \quad e_\theta = r\begin{pmatrix} \sin\theta\cos\phi \\ \sin\theta\sin\phi \\ \cos\theta \end{pmatrix} \quad e_\phi = R\begin{pmatrix} -\sin\phi \\ \cos\phi \\ 0 \end{pmatrix} \tag{3.3}$$

The basis in Eq. (3.3) is orthogonal, so the covariant and contravariant basis vectors are parallel. The covariant and contravariant sets of basis vectors are related by

$$\nabla r = \mathbf{e}_r \quad \nabla\theta = \frac{\mathbf{e}_\theta}{r^2} \quad \nabla\phi = \frac{\mathbf{e}_\phi}{R^2}. \tag{3.4}$$

In order to evaluate the geometric coefficients appearing in Eqs. (2.23-2.27), the magnetic field is specified via its flux function $\tilde\psi(r,\theta)$, which should be a solution of the Grad-Shafranov equation but here we assume it can be any 2D function. From the flux function, we derive the magnetic field in covariant and contravariant components,

21

$$\mathbf{B} = F(\tilde{\psi})\nabla\phi + \nabla\phi \times \nabla\tilde{\psi}(r,\theta) \tag{3.5}$$

$$= \frac{F(\tilde{\psi})}{R^2}\mathbf{e}_\phi - \frac{1}{rR}\frac{\partial\tilde{\psi}}{\partial\theta}\mathbf{e}_r + \frac{1}{rR}\frac{\partial\tilde{\psi}}{\partial r}\mathbf{e}_\theta \tag{3.6}$$

$$= F(\tilde{\psi})\nabla\phi - \frac{1}{rR}\frac{\partial\tilde{\psi}}{\partial\theta}\nabla r + \frac{r}{R}\frac{\partial\tilde{\psi}}{\partial r}\nabla\theta \tag{3.7}$$

where we assume that $F(\tilde{\psi})$ is a constant, $F(\tilde{\psi}) = B_0 R_0$. From these expressions, we can calculate the norm $B = |\mathbf{B}|$ and unit vector $\mathbf{b} = \frac{\mathbf{B}}{B}$.

These expression are substituted into Eqs. (2.23 - 2.27) to obtain the operator coefficients needed to carry out GBS simulations.

In the GBS implementation, we define $\tilde{\psi}$ in terms of a normalised radial coordinate $\bar{r} = r/a$ where a is the radius at the wall. The coordinates θ and ϕ are already dimensionless.

The turbulent quantities evolved by GBS vary on spatial scales of order ρ_{s0} in the perpendicular direction. Therefore we use a coordinate system normalised to ρ_{s0} so that the gradients of the turbulent quantities are $O(1)$. This system, (x, y, z), is related to the (r, θ, ϕ) system by

$$x = \frac{(r-a)}{\rho_{s0}} \quad y = \frac{a\theta}{\rho_{s0}} \quad z = \phi. \tag{3.8}$$

The expressions of the parametric operators appearing in Eqs. (2.28 - 2.32) are expressed in the (x, y, z) coordinates. We present the example of the derivation of the parallel gradient operator, the derivation of the other four operators is found in Ref. [67] with only the final expression given below.

The definition of the parallel gradient operator is given by Eq. (2.27), which we can write in the circular coordinate system and dimensionless units as

$$\mathbf{b}\cdot\nabla f = \frac{1}{B}(B^r\partial_r + B^\theta\partial_\theta + B^\phi\partial_\phi)f. \tag{3.9}$$

Using Eq. 3.6 and 3.7 we find that

$$B^2 = B_0^2 R_0^2 + \frac{a^2 B_0^2}{R_0^2 \bar{R}^2}\left[\frac{1}{\bar{r}^2}\left(\frac{\partial\psi}{\partial\theta}\right)^2 + \left(\frac{\partial\psi}{\partial\bar{r}}\right)^2\right] \tag{3.10}$$

where the normalised quantities $\bar{R} = R/R_0$ and $\psi = \tilde{\psi}/(a^2|B_0|)$ are both $O(1)$. We substitute the expression for the **B** components in Eq. 3.6 into Eq. 3.9 and express the perpendicular derivatives in terms of the x and y coordinates so that they are also $O(1)$:

$$\mathbf{b} \cdot \nabla f = \frac{1}{B} \left[\frac{B_0 R_0}{\bar{R}^2 R_0^2} \partial_\phi - \frac{|B_0|}{\bar{r} R_0 \bar{R}} \frac{\partial \psi}{\partial \theta} \frac{a}{\rho_{s0}} \partial_x + \frac{|B_0|}{\bar{r} R_0 \bar{R}} \frac{\partial \psi}{\partial \bar{r}} \frac{a}{\rho_{s0}} \partial_y \right] f. \tag{3.11}$$

We simplify the expression in Eq. (3.11) using the ordering parameters a/R_0, $l_\perp/R_0$ and ρ_{s0}/R_0, where $l_\perp$ is the length scale of field gradients in the poloidal plane. We keep only the first order terms in these parameters, as described fully in Ref. [67]. The parallel gradient operator we consider for our simulations is then

$$R_0 \nabla_\parallel f = \frac{B_0}{|B_0|} \frac{\partial f}{\partial \phi} + \frac{a}{\rho_{s0}} \frac{1}{\bar{r}} \left(\frac{\partial \psi}{\partial \bar{r}} \frac{\partial f}{\partial y} - \frac{\partial \psi}{\partial \theta} \frac{\partial f}{\partial x} \right). \tag{3.12}$$

We note that for the parallel gradient operator, none of the terms can be dropped using the above ordering. Following similar steps, we obtain the other geometric operators:

$$
\begin{aligned}
\nabla_\parallel^2 f = \quad & \frac{\delta^{-2}}{\bar{r}^2} \left((\frac{\partial \psi}{\partial \theta})^2 \frac{\partial^2 f}{\partial x^2} + (\frac{\partial \psi}{\partial \bar{r}})^2 \frac{\partial^2 f}{\partial y^2} - 2 \frac{\partial \psi}{\partial \bar{r}} \frac{\partial \psi}{\partial \theta} \frac{\partial^2 f}{\partial x \partial y} \right) \\
& + \delta^{-1} \left(\frac{1}{\bar{r}^2} (\frac{\partial \psi}{\partial \theta} \frac{\partial^2 \psi}{\partial \bar{r} \partial \theta} - \frac{\partial \psi}{\partial \bar{r}} \frac{\partial^2 \psi}{\partial \theta^2}) - \frac{1}{\bar{r}^3} (\frac{\partial \psi}{\partial \theta})^2 \right) \frac{\partial f}{\partial x} \\
& + \delta^{-1} \left(\frac{1}{\bar{r}^2} (\frac{\partial \psi}{\partial \bar{r}} \frac{\partial^2 \psi}{\partial \bar{r} \partial \theta} - \frac{\partial \psi}{\partial \theta} \frac{\partial^2 \psi}{\partial \bar{r}^2}) + \frac{1}{\bar{r}^3} \frac{\partial \psi}{\partial \bar{r}} \frac{\partial \psi}{\partial \theta} \right) \frac{\partial f}{\partial y} \\
& + \delta^{-1} \frac{B_0}{|B_0|} \frac{2}{\bar{r}} (\frac{\partial \psi}{\partial \bar{r}} \frac{\partial^2 f}{\partial y \partial \phi} - \frac{\partial \psi}{\partial \theta} \frac{\partial^2 f}{\partial x \partial \phi}) + \frac{\partial^2 f}{\partial \phi^2}
\end{aligned}
\tag{3.13}
$$

$$C(f) = \frac{B_0}{|B_0|} \left(\sin\theta \frac{\partial f}{\partial x} + \frac{\cos\theta}{\bar{r}} \frac{\partial f}{\partial y} \right) \tag{3.14}$$

$$\nabla_\perp^2 f = \frac{1}{\bar{r}^2} \frac{\partial^2 f}{\partial y^2} + \frac{\partial^2 f}{\partial x^2} \tag{3.15}$$

$$[\Phi, f] = \frac{1}{\bar{r}} [\Phi, f]_{\bar{r}, \theta} \tag{3.16}$$

where we defined $[\Phi, f]_{x,y} = \partial_x \Phi \partial_y f - \partial_y \Phi \partial_x f$.

3.3   Overview of simulation results

3.3.1   Magnetic field and simulation parameters

The magnetic field configuration we consider for our simulations is based on that of three infinite wires, one located on the magnetic axis, one at a distance $2a$ above the magnetic axis and one $2a$ below the magnetic axis. The wire located on the magnetic axis mimics the plasma current in the core. We take the flux function,

$$\psi(s,\theta) = S(\log(s) + \frac{1}{2}I_n(\log(s^2 + a^2 - 2as\sin\theta) + \log(s^2 + a^2 + 2as\sin\theta)), \tag{3.17}$$

where I_n is the ratio of current strength in each of the outer wires with respect to inner wire, and perform a radial transform $s = r - r_0$, with r_0 an ad-hoc parameter to obtain a configuration sufficiently circular to fit in the simulation domain. The parameter S is used to tune the poloidal field strength. In our simulations, the upper and lower wires carry a current ten times stronger than the central wire ($I_n = 10$). By setting $r_0 = 0.9a$ we obtain a configuration sufficiently circular to fit in the domain. The flux surfaces are shown in Fig. 3.1.
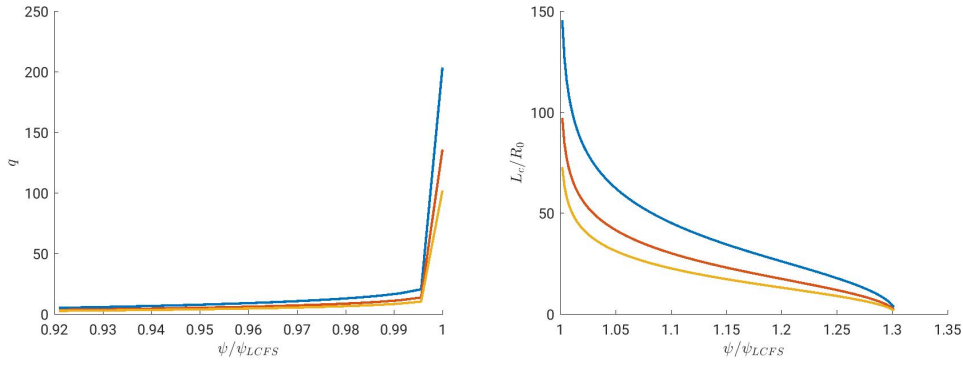

Figure 3.2 – Profiles of the safety factor, $q(\psi)$ in the closed flux regions and the connection length $L_c(\psi)$ on the LFS (right). Profiles for $q = 4.3, 6.5, 8.6$ are shown in yellow, orange and blue respectively. Both q and L_c tend to infinity at the LCFS.

Based on the magnetic field specified in Eq. (3.17) we carried out a set of simulations where we varied the safety factor and resistivity - here we present some of the main features of the simulation results.

3.3.2 Parameter scan in ν and q

Simulations consider a fixed plasma size, $\rho_*^{-1} = R_0/\rho_{s0} = 500$, $L_x = x_{\text{wall}} - x_{\text{inner boundary}} = 120\rho_{s0}$ and $L_y = 2\pi a = 800\rho_{s0}$. The grid resolution is $\Delta x = 0.769\rho_{s0}$ and $\Delta y = 1.78\rho_{s0}$ for the simulations with $\nu = 1$ and $\Delta x = 0.513\rho_{s0}$ and $\Delta y = 1.18\rho_{s0}$ for the simulations with $\nu = 0.1$ and 0.01. We use 80 planes in the z direction for the simulations with $\nu = 1$ and 120 planes for the simulations with $\nu = 0.1$ and 0.01. Previous convergence tests [69] show that this numerical convergence is reached with grid of this resolution.

The source terms, S_n and S_{T_e}, are Gaussian centred at a distance $11\rho_{s0}$ inside the LCFS with half width half maximum (HWHM) $1.5\rho_{s0}$ and amplitude $1.35n_0$. By tuning the poloidal field strength via the parameters S in Eq. (3.17), simulations are run with local safety factor $q = (a/\rho_*)\mathbf{B}\cdot\nabla z/\mathbf{B}\cdot\nabla y = 4.3, 6.5, 8.6$ at the LCFS outer midplane. The resulting profiles of q inside the LCFS and the connection length in the SOL are shown in Fig. 3.2. We also scan the parallel resistivity, $\nu = 1, 0.1$ and 0.01, typical experimental values for the normalised resistivity. Scans over these parameters are chosen since they are the most important controls on the plasma dynamics. We fix $\mu = m_i/m_e = 200$. Typical snapshots and time and z averaged fields are shown for all six fields for the highest and lowest resistivity with $q = 6.5$ in Figs. 3.3, 3.4 and 3.5. The effect of changing q is found to be much smaller than the effect of changing ν in these simulations.

These snapshots show the presence of fluctuations, particularly on the LFS. To quantify the fluctuation level, the standard deviation of n and ϕ is shown in Fig. 3.6. The fluctuation level is highest on the LFS near the midplane, as expected for interchange turbulence. For n, the highest fluctuation level is at the LCFS, for ϕ larger fluctuations are present further into the LFS. For the $\nu = 1$ simulations there are significant fluctuations in the private flux regions, for the $\nu = 0.01$ simulation less so.

In all the simulations, we observe asymmetries between the HFS and LFS, and upper and lower X points, even though the magnetic field is up-down symmetric. The asymmetries are visible in both the turbulent snapshots and time-averaged quantities. We now examine these asymmetries in more detail.

3.3.3 HFS-LFS asymmetry

In our simulations, we observe a turbulent LFS and quiescent HFS. Similar observations have been made in DN experiments [47]. This points out a different nature of turbulence in the HFS and LFS.

The different nature of turbulence on the HFS and LFS has been tested by considering two additional simulations. Removing the interchange instability drive [the curvature term in Eq. (2.29)] drastically reduces turbulence on the LFS (see Fig. 3.7), indicating ballooning instabilities are the primary driver of turbulence in this region. On the other hand, removing the Kelvin-Helmholtz drive [the $[\phi, \omega]$ term in the convective derivative in Eq. (2.29)] suppresses
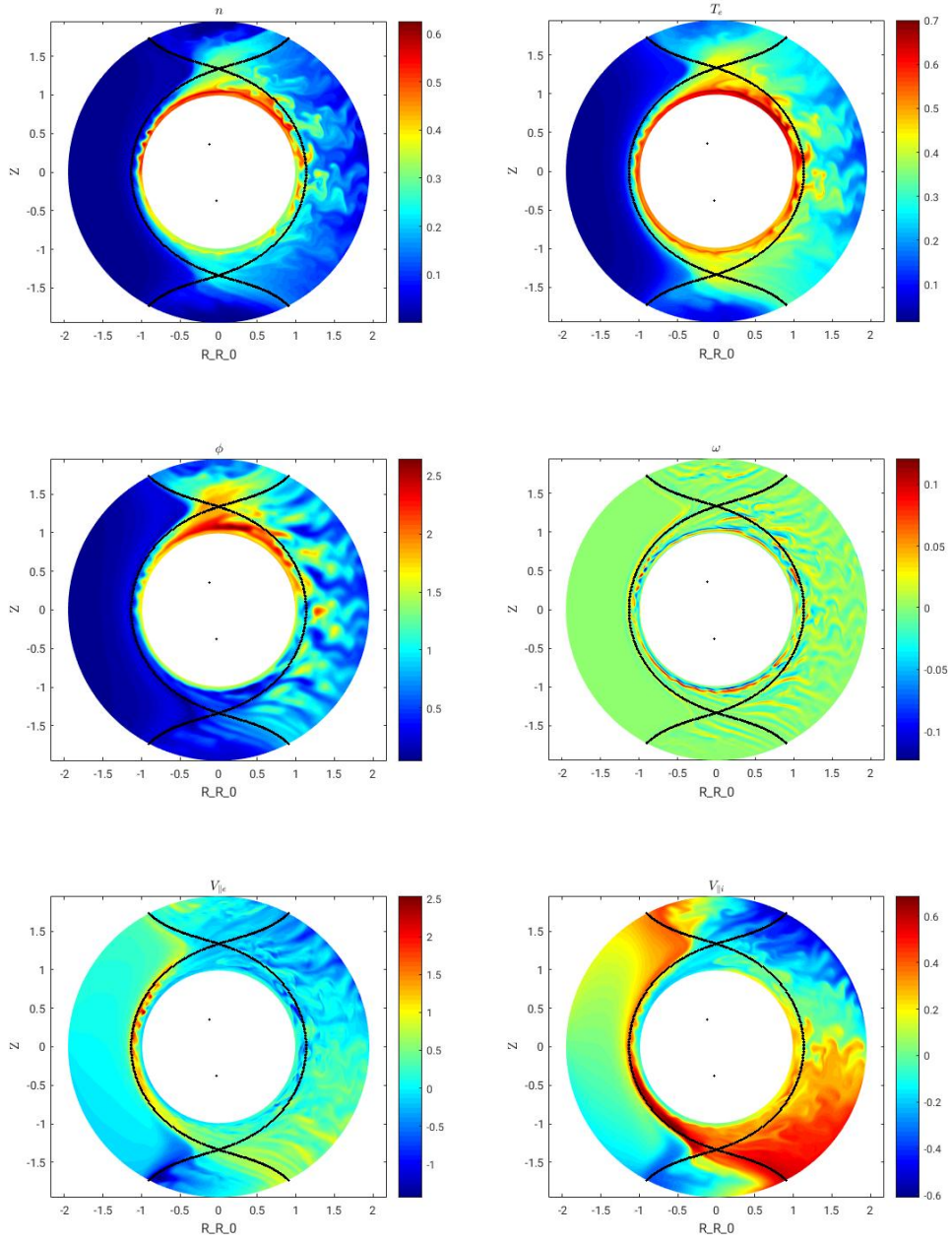
Figure 3.3 – Typical snapshots of the six fields for the $q = 6.5, \nu = 1$. The axis lengths are normalised to a.
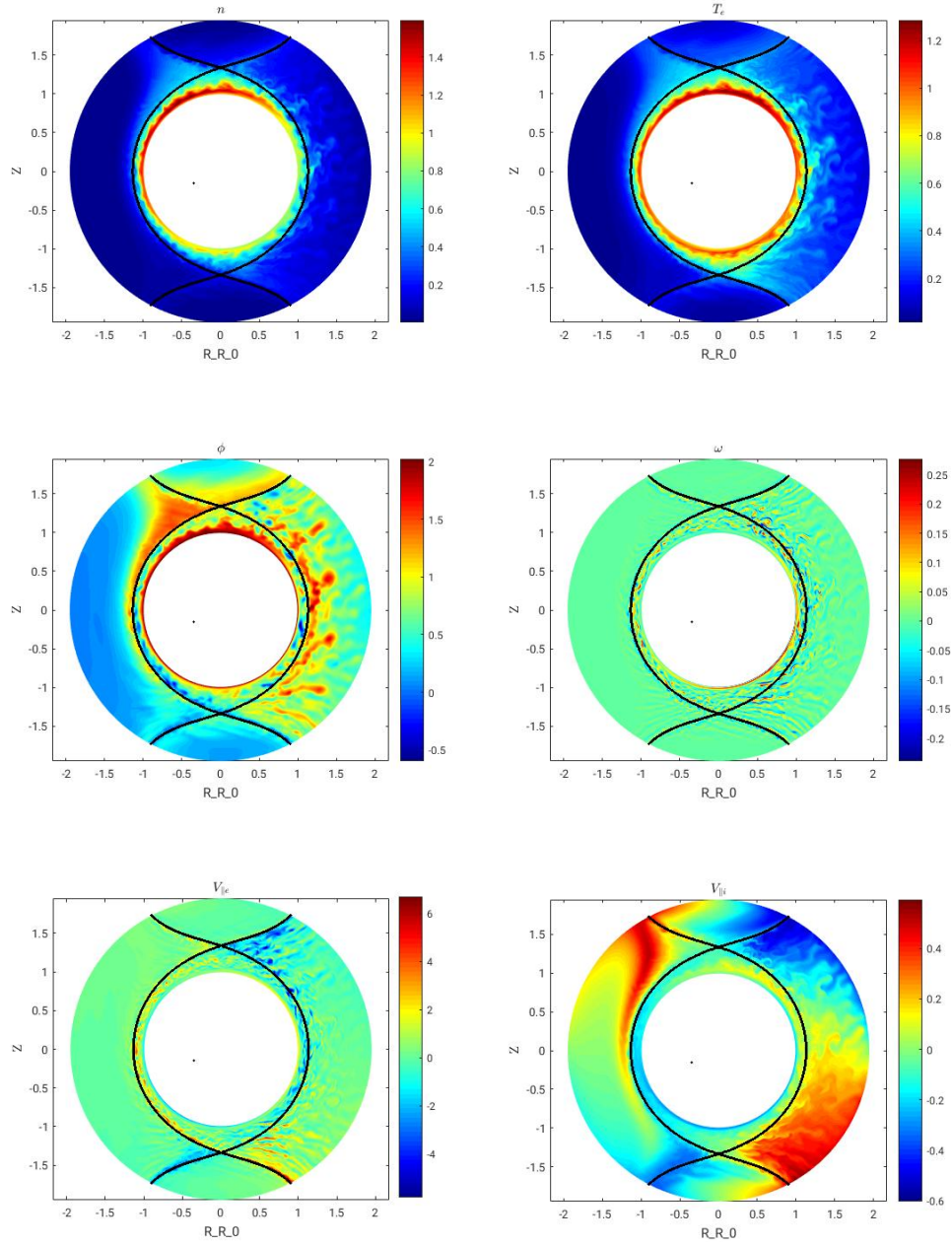
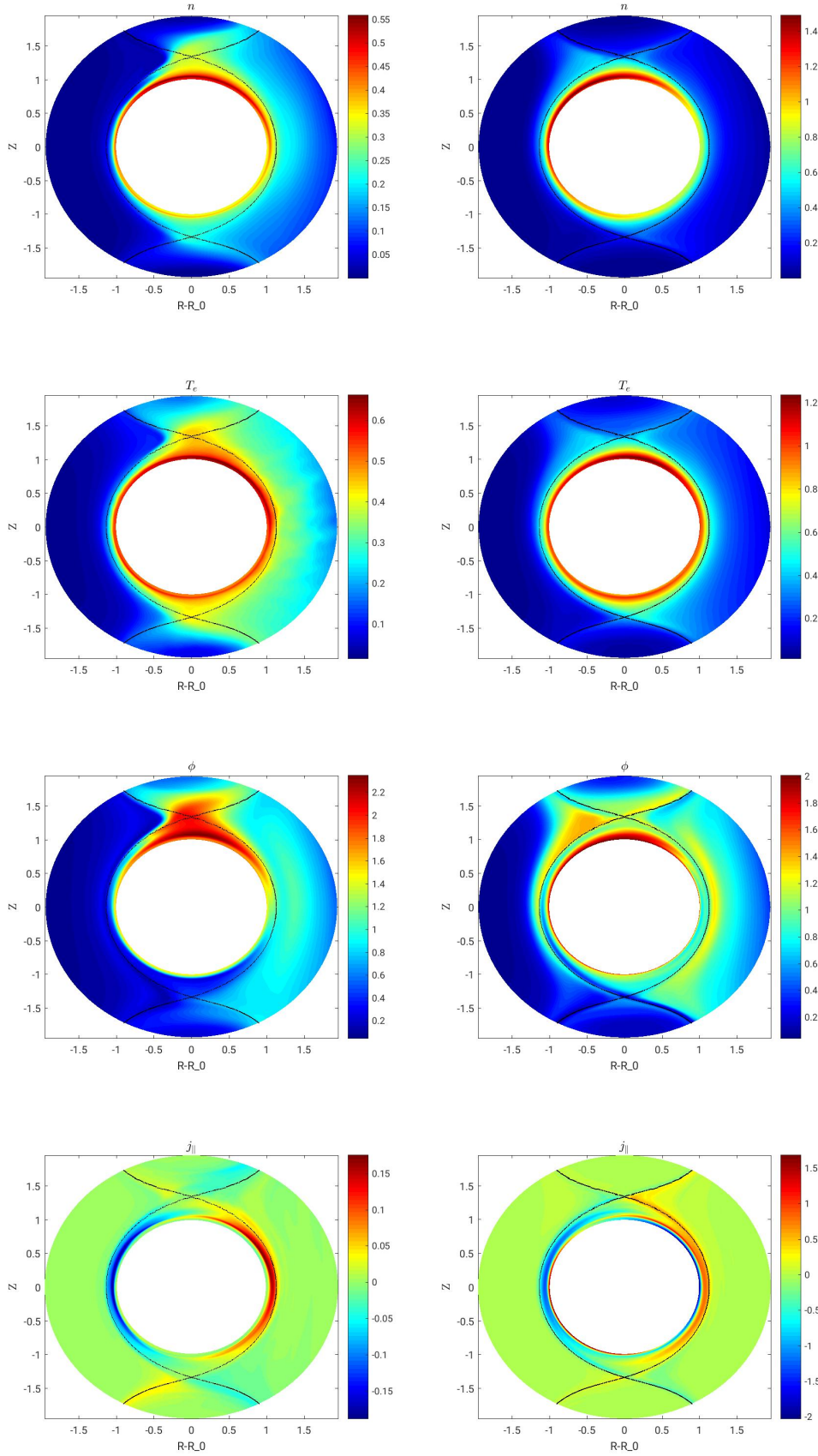Figure 3.4 – Typical snapshots of the six fields for the $q = 6.5, \nu = 0.01$.

Figure 3.5 – Comparison of time and toroidally averaged fields between the $q = 6.5$, $\nu = 1$ (left) and $\nu = 0.01$ (right) simuations. We observe a better confinement and less asymmetry in the lower resistivity simulation.
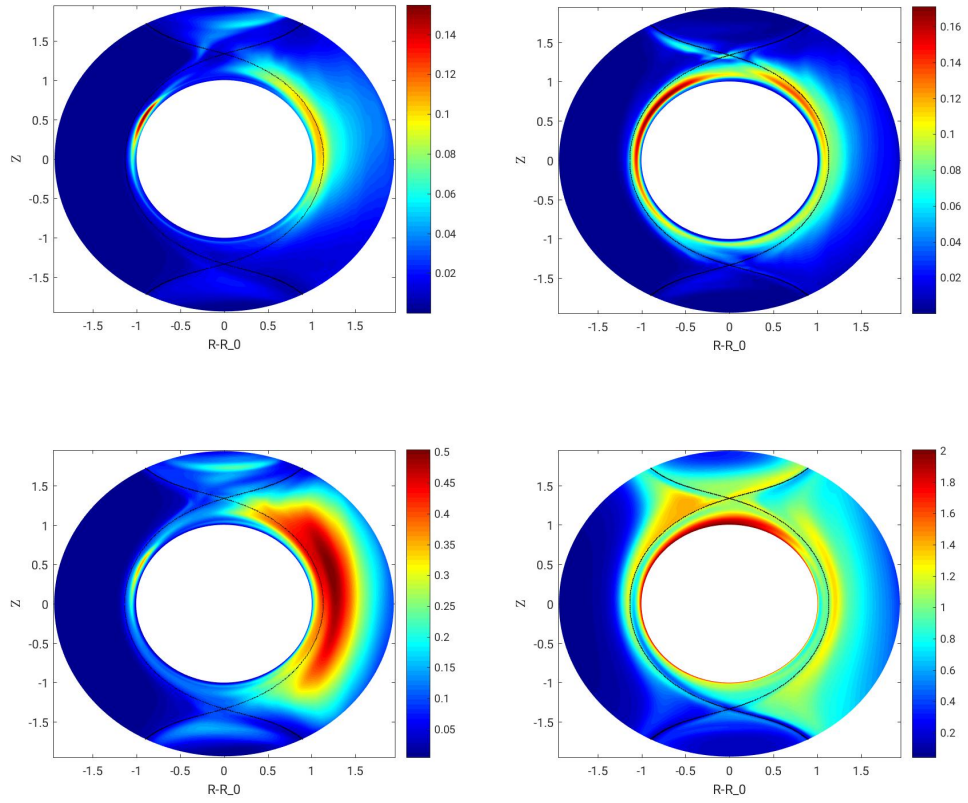
Figure 3.6 – Standard deviation of n and ϕ, a proxy for the fluctuation level.

the turbulence on the HFS but has a small impact on the LFS (Fig. 3.7), indicating velocity shear and the Kelvin-Helmholtz instability play a dominant role only on the HFS.

The analysis of LFS and HFS turbulence should therefore be carried out separately. In the following we will focus on the LFS, where most of the heat flux is exhausted.
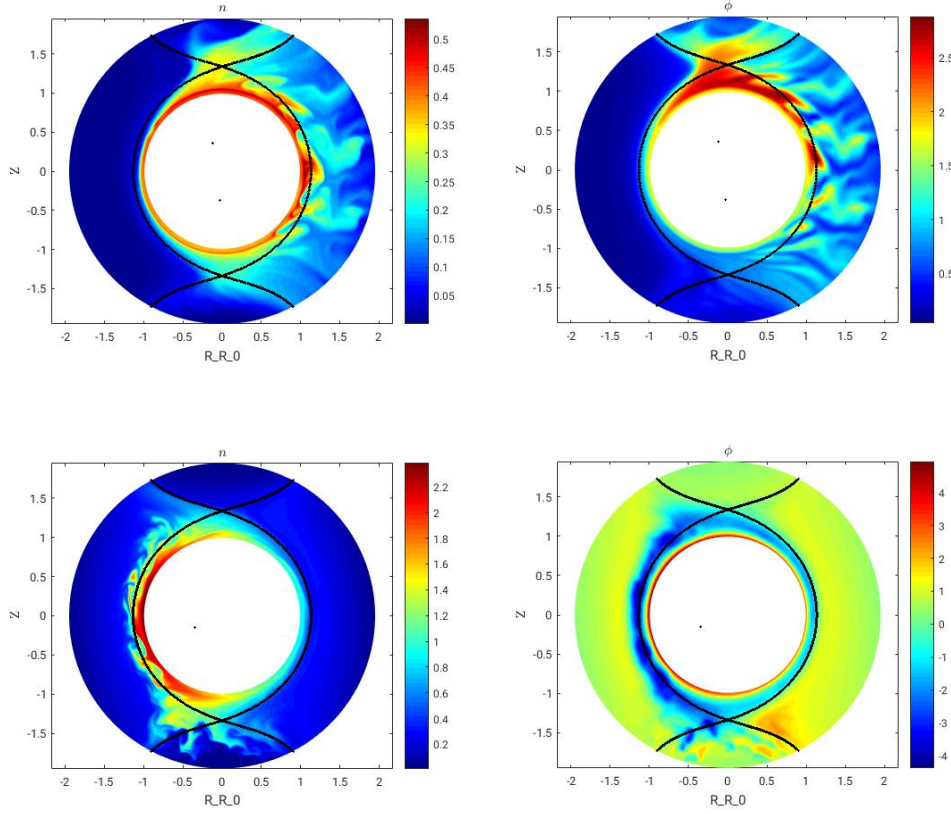

Figure 3.7 – Snapshots of n and ϕ for the simulations with no KH instability drive (top) and no interchange instability drive (bottom). Removing the KH drive has minimal effect on the turbulence, whist removing the interchange drive changes it completely.

3.3.4   Up-down asymmetry

We observe an up-down asymmetry, despite the fact that the magnetic configuration is perfectly balanced. In n and T_e this is caused by the time-averaged, anti-clockwise $\mathbf{E} \times \mathbf{B}$ advection of plasma from the midplane towards the upper X point on the LFS. On the HFS, turbulent outflow is negligible, hence plasma advection to the lower X point outside the LCFS is low, resulting in a less important asymmetry.

The asymmetry is even more pronounced in the electrical potential, particularly in the higher resistivity simulation (see Fig. 3.5). To understand the mechanism behind this asymmetry,

we followed the method described in Ref. [50], considering the dominant terms of the time averaged Eq. (2.31):

$$\nabla_\parallel \bar{\phi} = 1.71 \nabla_\parallel \bar{T}_e - (\bar{T}_e / \bar{n}) \nabla_\parallel n - \nu \bar{j}_\parallel \tag{3.18}$$

(we indicate the time and toroidal average with an overbar and the fluctuation with a tilde, e.g. $n = \bar{n} + \tilde{n}$). In addition to $\nabla_\parallel T_e$ and $\nabla_\parallel n$ contributions which result from the $E \times B$ convection, we observe an important contribution to $\nabla_\parallel \phi$ from the $j_\parallel$ term. This can be estimated by studying the main terms of the time averaged Eq. (2.29): $\nabla_\parallel j_\parallel \sim -(2/B)C(p_e)$ which is a balance between the diamagnetic and parallel currents. At the upper divertor, the parallel currents are directed from the X point towards the wall, whilst in the lower divertor region they flow from the wall towards the X point. This means that the contribution to ϕ from $\int_z (-\nu j_\parallel dz$ is positive for the upper X point and negative for the lower X point, since the poloidal component of **b** goes anticlockwise in both cases.

Up-down asymmetry in balanced DN configurations is widely observed in the heat flux to the outer legs [10], [16], [70] and can be enhanced or reduced in unbalanced configurations. The analysis of the up-down asymmetries in balanced and unbalanced configurations is the subject of Chapter 4.

3.4   LFS density decay

The density decay in our simulations cannot be properly described by a single exponential decrease, rather it can be fitted with two exponentials characterised by a shorter decay length L_n near the LCFS and longer decay length L'_n in the far SOL (see Fig. 3.8). Such a double decay length is a typical observation in a DN configuration, e.g. on C-Mod [47] and MAST [78], as well as in SN configurations [45] [12] and limited configurations [42]. It has also been observed in turbulent two-fluid simulations [26] [40].

The difference in the scale length is reflected by different turbulent properties in near and far SOL. As observed experimentally [8], [45], [14], the fluctuation distribution is close to Gaussian in the near SOL with increasing skewness and kurtosis, indicative of intermittency, in the far SOL (Fig. 3.8). In the following, we identify the two different mechanisms setting L_n and L'_n. We call the width of the inner SOL Δ, this is the distance over which the density decays steeply. We refer to the density, temperature and radial turbulent particle flux at the separatrix by $\bar{n}$, $\bar{T}_e$ and Γ, and at the entrance of the far SOL, i.e. a distance Δ from the separatrix, by $\bar{n}'$, $\bar{T}_e{}'$ and Γ', both at the outer midplane.

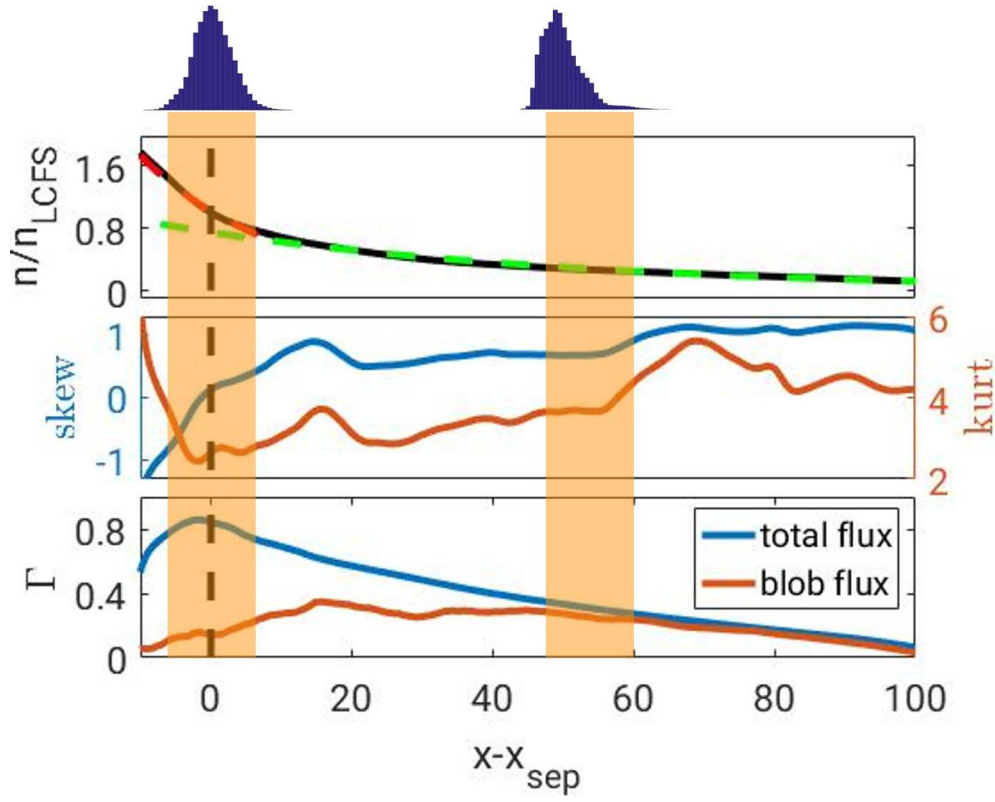Figure 3.8 – Radial profile of $\bar{n}$ at the outer midplane with the fitted exponentials (top), profiles of the skewness and kurtosis (middle) and total turbulent transport and transport due to blobs (bottom). Above are two PDFs of the normalised density fluctuation, $\tilde{n}/\sigma_n$, evaluated in the corresponding radius range, where σ_n is the standard deviation evaluated locally.

3.4.1   Turbulence in the near SOL

We start by looking at the near SOL. Since the turbulent radial flux in the near SOL is not due to large intermittent events, but can be rather associated to Gaussian-distributed fluctuations, we estimate the flux based on the development and saturation of a linear instability driven by the background radial gradient in density and temperature. We then match the predicted turbulent flux, Γ, to the turbulent flux across the LCFS, Γ_{LCFS}, to find L_n. It should be noted that although $\tilde{n}(k_y)$ has a broad spectrum, $\Gamma(k_y)$ has a clear peak [71], as shown in Fig. 3.9, which supports our approach based on considering one single mode as responsible for the turbulent transport.
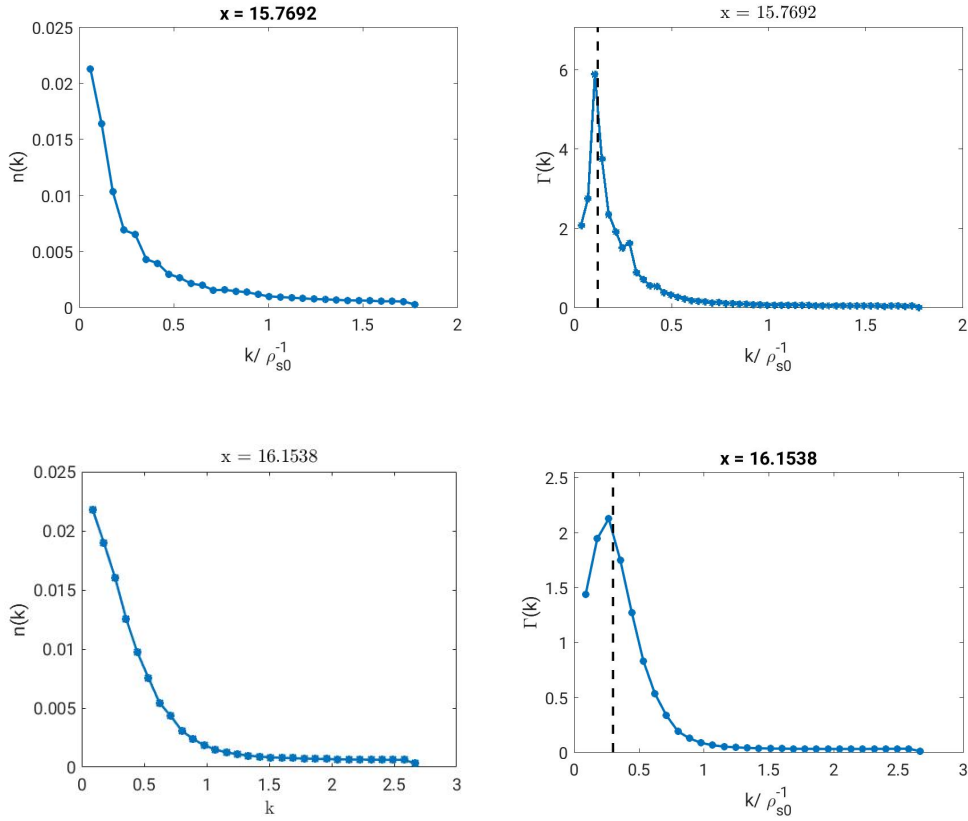

Figure 3.9 – Poloidal spectra of the density and $E \times B$ flux at fixed radius for the simulations with $\nu = 1$, $q = 6.5$ (top) and $\nu = 0.01$, $q = 6.5$. The flux spectrum has a clear peak even through the density fluctuation spectrum does not and the wavenumber of the peak matches well the linear analysis prediction shown by the dashed line.

The turbulent flux can be written

$$\Gamma = \left\langle \overline{\frac{\tilde{n}\partial_y\tilde{\phi}}{B}} \right\rangle_y \tag{3.19}$$

where the poloidal, y, average is evaluated over 45 degrees centered around the outer midplane. The density fluctuation can be estimated by noticing that linear instabilities saturate when the gradient of the fluctuations becomes comparable to the background density gradient, hence locally removing the turbulence drive [75][76], that is $\partial_x\tilde{n} \sim \partial_x\bar{n}$ or equivalently $k_x\tilde{n} \sim \bar{n}/L_n$, with k_x the typical radial wavenumber of the perturbation, in agreement with $\tilde{n}/\bar{n}$ in the simulations. We relate $\partial_y\tilde{\phi}$ to $\tilde{n}$ by balancing the leading order terms in the continuity equation, Eq. (2.28):

$$\gamma\tilde{n} = \rho_*^{-1}\frac{\partial\tilde{\phi}}{\partial y}\frac{\partial\bar{n}}{\partial x}\frac{1}{B} \tag{3.20}$$

where γ is the linear growth rate of the instability driving the transport. The simulation test mentioned above (Fig. 3.7) shows that ballooning modes drive turbulence on the LFS. For these modes, as well as for drift waves [80], non-local linear theory shows that $k_x = \sqrt{k_y/L_n}$ [75]. By considering the linear instability that maximises the transport, the turbulent flux

$$\bar{\Gamma} = \rho_*\bar{n}\left(\frac{\gamma}{k_y}\right)_{\max} \tag{3.21}$$

follows.

In order to evaluate the $(\gamma/k_y)_{\max}$, we linearise Eqs. (2.28) - (2.32) assuming $C(f) \sim \partial_y$, since the flux surfaces are approximately vertical in most of the region we are considering, and neglecting radial variation of the perturbation and poloidal variation of the equilibrium. We take $k_\parallel = 2/q$ where 2 approximately is the minimum parallel mode number allowed by our configuration. This is expected from ballooning stability and observed in the simulations. The linearised system

$$\begin{pmatrix} \gamma & (ik_yR_0T_{e0})/L_n & 0 & 0 \\ 2ik_yT_{e0} & k_y^2T_{e0}\gamma & -ik_\parallel\sqrt{T_{e0}} & 2ik_yT_{e0} \\ 0 & -ik_\parallel\sqrt{T_{e0}} & \nu & 0 \\ 0 & (ik_yR_0T_{e0}\eta)/L_n & 0 & \gamma \end{pmatrix}\begin{pmatrix} n \\ \phi \\ j_\parallel \\ T_e \end{pmatrix} = 0 \tag{3.22}$$

that we obtain corresponds to that of the simple magnetic torus geometry [72]. We take $\eta = L_n/L_{Te} = 0.77$, the theoretically expected value [76], which is within 20% of the simulations. Using $\Gamma = \Gamma_{LCFS}$ and solving the dispersion relation associated with the system 3.22 we find numerically the k_y and L_n shown in Fig. 3.10 for three values of Γ_{LCFS}. The estimates of L_n correspond well to the simulations, as shown in Fig. 3.16.

To understand the decrease in k_y and increase in L_n with increasing ν and q (which has been observed experimentally [64]), we consider the limit (valid for typical parameters) in which the resistive ballooning mode is dominant: $R/L_n \gg 1$, $\mu\gamma \ll \nu$ and, to avoid coupling with sound waves and drift waves, $k_\parallel \ll \gamma$ and $\omega_* \ll \gamma$ where $\omega_* = k_y R/L_n$. The dispersion relation from Eq. (3.22) reduces to $\gamma^2 - \gamma_i^2 + \gamma k_\parallel^2/(\nu k_y^2) = 0$, where $\gamma_i = \sqrt{2R(1+\eta)/L_n}$ is the ideal ballooning growth rate, capturing well the strong transport limit [38]. Expressed in physical units to make explicit the dependence on physical parameters, the density scale length we obtain can be written as

$$L_n = \frac{2}{3}(1+\eta)\bar{c}_s^2\left(\frac{q\bar{n}}{2\Gamma_{LCFS}}\right)^{4/3}\left(\frac{m_e}{m_i 1.96\tau_e}\right)^{2/3}\omega_i^{-4/3}R_0^{1/3}, \qquad (3.23)$$

which of the order 1mm for typical experimental parameters in TCV and C-Mod tokamak [47], [95]. We can use this equation to estimate k_y by noticing that the peak γ/k_y occurs approximately where the damping term and ballooning drive are equal. Using $\gamma \sim \gamma_i$, we find

$$k_y = \frac{2^{2/3}}{3^{1/4}}\left[\frac{1.96\bar{n}\omega_i^2 m_i \tau_e}{q^2\Gamma_{LCFS}R_0^2 m_e}\right]^{1/3} \qquad (3.24)$$

in physical units. The full numerical result, shown in Fig. 3.10, agrees well with this estimate, as well as the simulation flux spectra as shown in Fig. 3.9.

3.4.2   Turbulence in the far SOL

We now turn to the far SOL, where the fluctuation distribution is heavy-tailed (Fig. 3.8), indicating intermittent turbulence. Indeed observation of the simulation results reveals the presence of coherent structures of high plasma density - blobs - that propagate outwards due to their self-generated $E \times B$ velocity. Considerable effort has been made to understand the dynamics of blobs, as described in the review paper Ref. [14], motivated by their significant contribution to the total radial transport in the SOL (shown for example in Ref. [62]). In particular, the relationship between the blob size and velocity has been the subject of extensive work, culminating in the two-region model [61], [83] which has been validated against both experimental measurements (see e.g. Ref. [94]) and simulations (see e.g. Ref. [68]). The
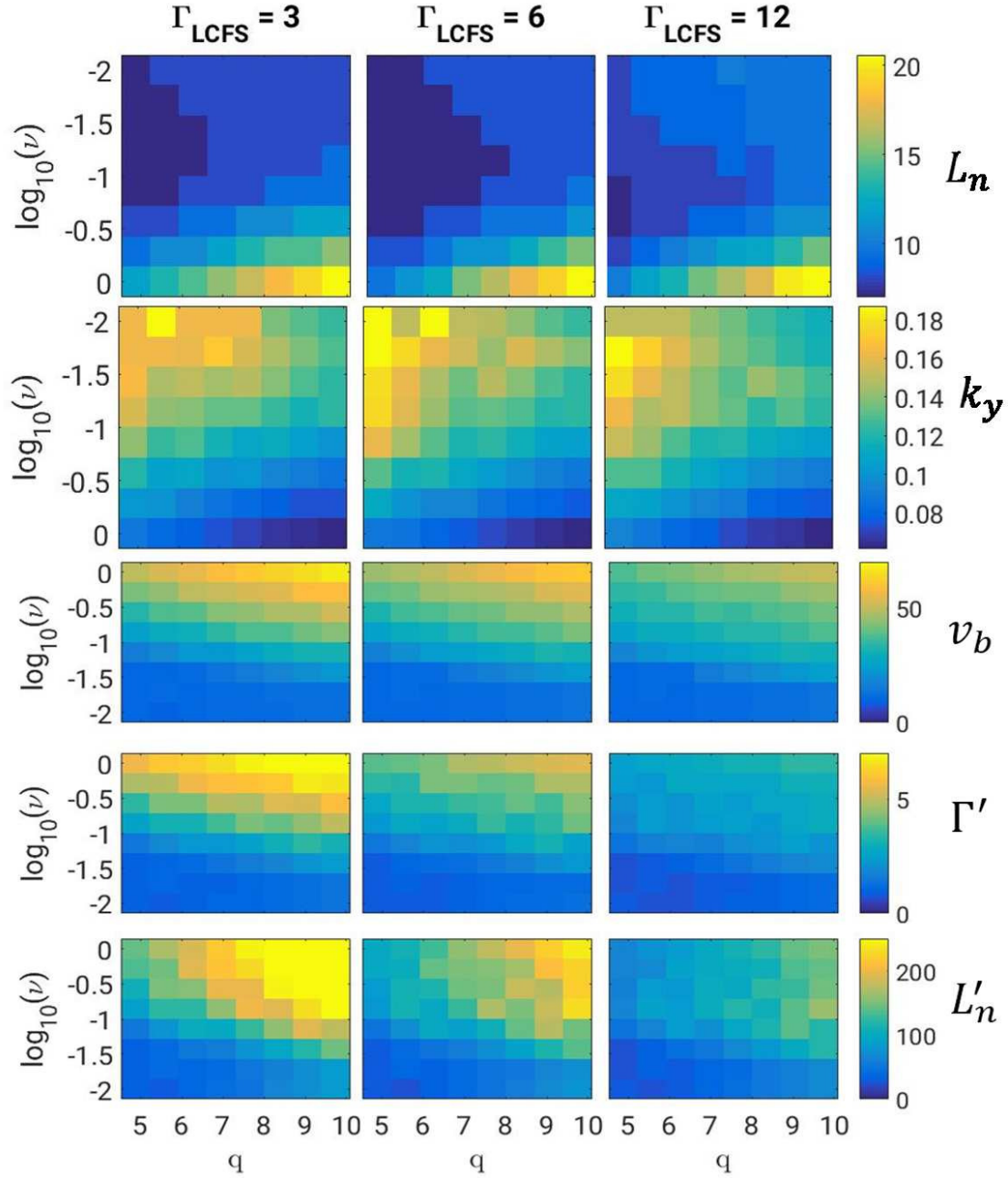
Figure 3.10 – Predicted L_n, k_y, v_b, Γ' and L'_n as a function of v, q and Γ_{LCFS}. All reference quantities are taken at the LCFS.

two-region model describes the radial motion of blobs (defined as regions of plasma density over a certain threshold based on the standard deviation of the density fluctuation) in diverted configurations. The two regions refers to the region around the midplane (region 1), where ballooning instability drive is significant and the region near the divertor (region 2) where the ballooning instability drive is negligible (see Fig. 3.11). The two regions are separated by an area of high flux expansion, which has the effect of making the blobs more elongated in the poloidal plane. We give a brief overview of the derivation of the two-region model size-velocity relation. A more detailed derivation can be found in Ref. [68].
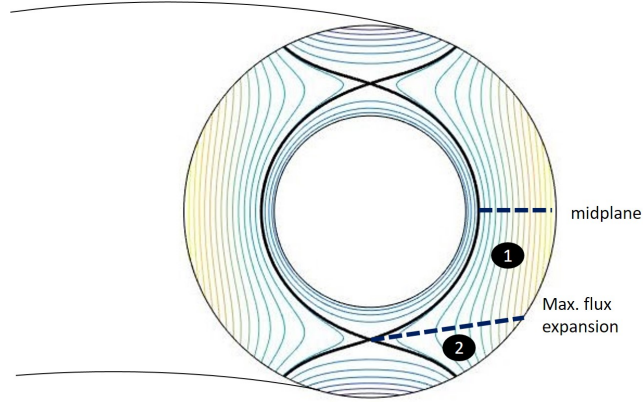

Figure 3.11 – The two regions referred to in the two region model. Region 1 lies between the midplane and the region of maximum flux expansion, region 2 lies between the region of maximum flux expansion and the wall.

We first consider the linear system governing the blob instability, starting from the simplified vorticity equations (simplified Eq. (2.29)) in the two regions:

$$\partial_t \omega_1 + \rho_*^{-1}[\phi_1, \omega_1] = \frac{1}{n_1}\nabla_\parallel J_{\parallel,1} + \frac{2T_e}{n_1}C(n_1)$$
$$\partial_t \omega_2 + \rho_*^{-1}[\phi_2, \omega_2] = \frac{1}{n_2}\nabla_\parallel J_{\parallel,2}$$

and the density equation in region 1

$$\partial_t n_1 + \rho_*^{-1}[\phi_1, n_1] = 0. \tag{3.25}$$

Note that we include the ballooning instability drive only in region 1. The subscripts refer quantities in region 1 and 2, and the model is isothermal. At the outer midplane, the curvature term is given by $C(n_1) = -\frac{1}{r}\frac{\partial n_1}{\partial \theta}$. We linearise these equations about a background density that depends only on x and a constant background potential. Therefore

$$n_i = n_{0,i}(x) + \delta n_i e^{-i\omega t + i k_i y}$$
$$\phi_i = \delta \phi_i e^{-i\omega t + i k_i y}.$$

We substitute these expressions into Eq. 3.25 to relate the density and potential perturbations in region 1:

$$\omega \delta n_1 = -\rho_*^{-1} k_1 \delta \phi_1 \frac{\partial n_1}{\partial x}. \tag{3.26}$$

For the parallel current gradients, we use the two point approximation [61]. This can be written in region 1 as

$$\nabla_\parallel J_\parallel \sim \frac{\phi_1 - \phi_2}{\nu L_{\parallel 1}^2}. \tag{3.27}$$

where $L_{\parallel 1}$ is the field line length from the midplane to the region of maximum flux fanning. Assuming no current at the midplane, $J_\parallel$ at the boundary between the two regions is approximately $(\phi_1 - \phi_2)/(\nu L_{\parallel 1})$. Hence for region 2, we have

$$\nabla_\parallel J_\parallel \sim \frac{1}{L_{\parallel 2}} \frac{\phi_1 - \phi_2}{\nu L_{\parallel 1}} - \frac{n_2 c_s}{T_e}(\phi_2 - \phi_f) \tag{3.28}$$

where $L_{\parallel 2}$ is the field line length from the region of maximum flux fanning to the wall and the sheath current $J_\parallel = n c_s (1 - \exp(\lambda - \phi/T_e))$ has been linearised around $\phi \approx \phi_f = \lambda T_e / e$.

Linearising these equations we have the system

$$\omega^2 \delta \phi_1 = -i\omega_{\sigma,1} \omega (\delta \phi_1 - \delta \phi_2) - \gamma_{mhd}^2 \delta \phi_1$$
$$\omega \delta \phi_2 = i\omega_{\sigma,2} \frac{k_1^2}{k_2^2} (\delta \phi_1 - \delta \phi_2) - i\omega_{\alpha,2} \delta \phi_2 \tag{3.29}$$

where we have introduced the frequencies $\omega_{\sigma,j} = (\nu L_1 L_j n_{0,j} k_1^2)^{-1}$ associated with the parallel resistivity, $\omega_{\alpha,j} = (\rho_s L_2 k_j^2)^{-1}$ associated with the sheath resistivity and $\gamma_{mhd} = (-2\rho_s^2 \rho_*^{-1} \frac{\partial_x n_1}{n_{0,1}})^{1/2}$

the ballooning instability growth rate. The relative sizes of these timescales define the blob regime parameters

$$\Lambda = \omega_{\alpha,1}/\omega_{\sigma,1} = \nu\bar{n}'L_{\parallel 1}^2/[L_{\parallel 2}\rho_s]$$

$$\Omega = \omega_{\alpha,1}/\gamma_{mhd} = \frac{k_1^{-4}n_{0,1}}{2\rho_{s1}^2\rho_{s2}^2L_{\parallel 2}^2\frac{\partial_x n_1}{n_{0,1}}\rho_*^{-1}}$$

These parameters quantify the importance of sheath resistivity with respect to plasma resistivity and sheath resistivity with respect to ballooning drive, respectively. We consider a high and low resistivity limit. For $\Lambda \gg 1$, the first term on the RHS in the second of equations 3.29 vanishes, requiring $\delta\phi_2 = 0$, meaning the perturbation does not extend into the divertor region. The first equation then gives

$$1 + \hat{\omega}^2 + i\hat{\omega}\frac{\Theta}{\Lambda} = 0 \tag{3.30}$$

where the normalised frequency $\hat{\omega} = \omega/\gamma_{mhd}$. We see that the curvature drive (first term) is balanced by either the region one inertia (second term) or region one plasma resistivity (third term). For $\Lambda \ll 1$, the ω_σ terms (parallel current between the two regions) cancel to first order and solving the second order system gives

$$1 + (1 + f^2)\hat{\omega}^2 + i\Theta\hat{\omega} = 0. \tag{3.31}$$

where f is the flux tube fanning [61]. Therefore, the curvature drive can be balanced either with fanning enhanced inertia in region two or with the sheath resistivity.

To relate these results to the blob behaviour, we invoke the blob correspondence principle [61], [14]: that a single blob moves according to the linear dispersion relation. From the linearised continuity equation, we have therefore that blob velocity

$$v_x = v_E = \Im(\omega)\rho_*\frac{\delta n_1}{\partial_x n_1} \tag{3.32}$$

where the $E \times B$ velocity $v_E = -ik_1\delta\phi_1$. Using the normalised size and velocity $\hat{a} = a_b/a_*$,

$\hat{v} = v / v_*$ where

$$
\begin{aligned}
a_b &= (2a_y/\pi)^{4/5} a_x^{1/5} \\
a_* &= [2\rho_s^4 L_{\|2}^2 n_b/(a_x \bar{n}' \rho_*)]^{1/5} \\
v_* &= \rho_s [2\pi^2 a_x^2 \rho_s^2 \rho_*^2 L_{\|2} n_b/(\bar{n}' a_y^2)]^{1/5}
\end{aligned}
\tag{3.33}
$$

this becomes $\hat{v} = Im(\hat{\omega})\hat{a}^{1/2}$ and the above relations correspond to the $a - v$ scalings shown in figure 3.12. A complete characterization of the blobs in these simulations is given in Ref. [68].

We use a pattern recognition algorithm described in [68] to track the blobs (defined here as coherently propagating structures of amplitude greater than 2.5 times the standard deviation of n) and measure their size, amplitude and velocity. Following Ref. [63] we calculate the fraction of the cross field transport due to blobs by assuming a 2D Gaussian density distribution of each blob in the poloidal plane with a peak density fluctuation $n_{b,i}$ and radial and poloidal HWHM $a_{x,i}$ and $a_{y,i}$ where i is the blob index. The blob flux is calculated

$$
\Gamma_b(x, y) = \sum_i n_{b,i} v_{b,i} \exp\left[\frac{(x - x_{b,i})^2}{2a_{x,i}^2} + \frac{(y - y_{b,i})^2}{2a_{y,i}^2} \right],
\tag{3.34}
$$

where the sum is carried out over all blobs and $(x_{b,i}, y_{b,i})$ are the blobs' centre of mass. We find that blob transport dominates in the far SOL (Fig. 3.8), consistent with the result of Ref. [63] and previous experimental works that found blobs to contribute an order unity fraction of the particle flux [8], [14], [7].

To estimate the far SOL decay length, we balance the divergences of the blob flux and parallel flux: $\nabla_\perp \Gamma' = \nabla_\| \Gamma_\|$. Since the parallel flow near the divertor is not intermittent (see Fig. 3.14) we can estimate the divergence of the parallel flux from the Bohm boundary conditions, $\nabla_\| \Gamma_\| \sim \bar{n}' c_s'/L_\|$ with $L_\| = L_{\|1} + L_{\|2}$, $\bar{n}' = \bar{n} \exp(-\Delta/L_n)$ and $\bar{c}_s' = \bar{c}_s \exp(-\Delta\eta/[2L_n])$. We remark that L_n' depends only weakly on Δ since Γ' also scales approximately with $\bar{n}' \bar{c}_s'$. We assume that the blob flux can be written in the form $\Gamma' = C\bar{n}'^\alpha$ where C is a product of parameters with no radial dependence in the simple model (v, R_0, q etc) and α is a power of order unity. The exponential decay of $\bar{n}$ with radius then gives that $\nabla_\perp \Gamma' = C\alpha\Gamma'/L_n' \sim \Gamma'/L_n$. We now relate the blob flux to the time and toroidal average density $\bar{n}'$ and near SOL properties.

First, we express the blob flux averaged in the poloidal plane [83]

$$
\Gamma' = \langle \Gamma_b \rangle_{x,y} = \sigma_b f_b v_b
\tag{3.35}
$$

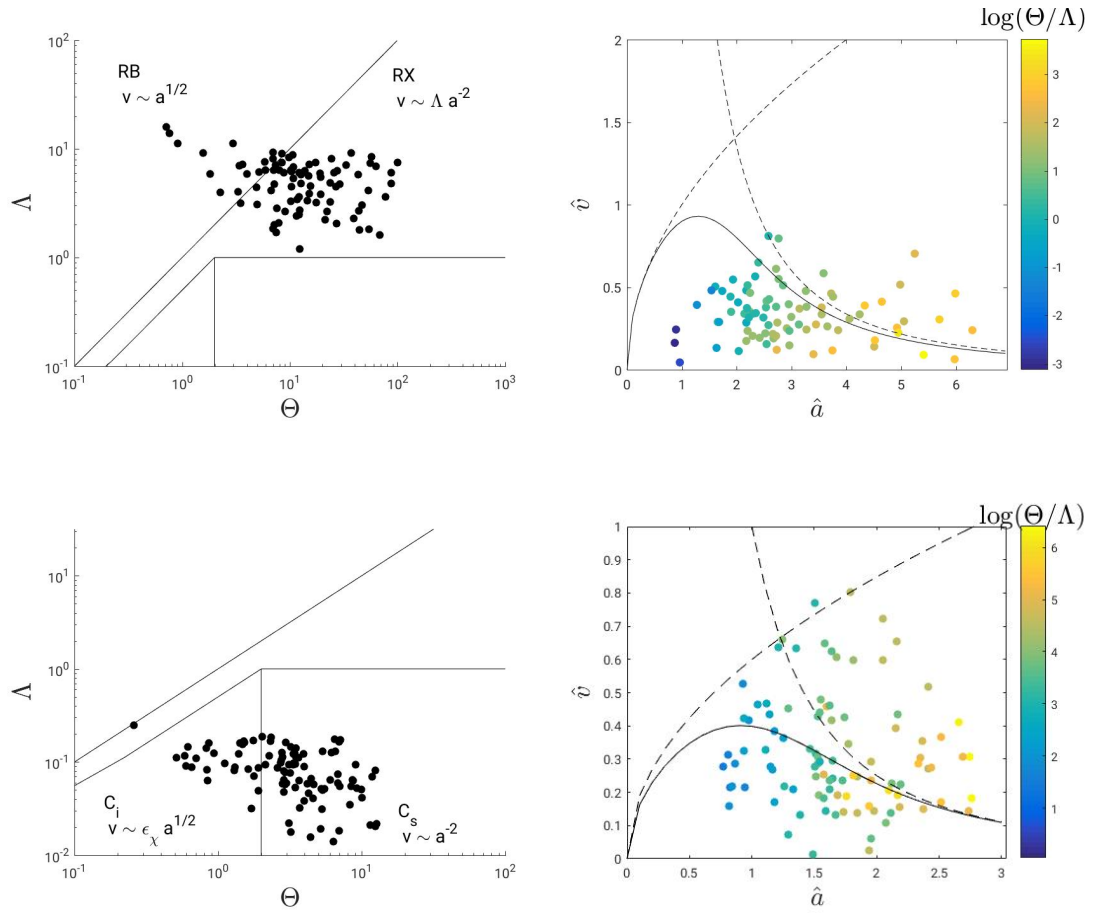in terms of σ_b the average density inside a blob, f_b the blob packing fraction (ratio of area

Figure 3.12 – Comparison of the detected blobs to the two region model predictions for the $v = 1$ simulations (top) and $v = 0.01$ simulation (bottom). In the $\Lambda - \Theta$ plots (left)we see that blobs in the $v = 1$ simulation are in the RB and RX regimes, meaning they don't extend to the wall in the parallel direction, whilst in the $v = 0.01$ simulation the blobs are in the C_i and C_s regions, meaning they extend into divertor region and in some cases to the wall. In the $a - v$ scaling plots (right) we see a good agreement with the two region model scaling relations. The solid black line is the scaling relation Eq. (3.30) in the upper plot, and Eq. (3.31) in the lower plot. The dashed lines are the RB and RX asymptotes in the upper plot and C_i and C_s asymptotes in the lower plot.
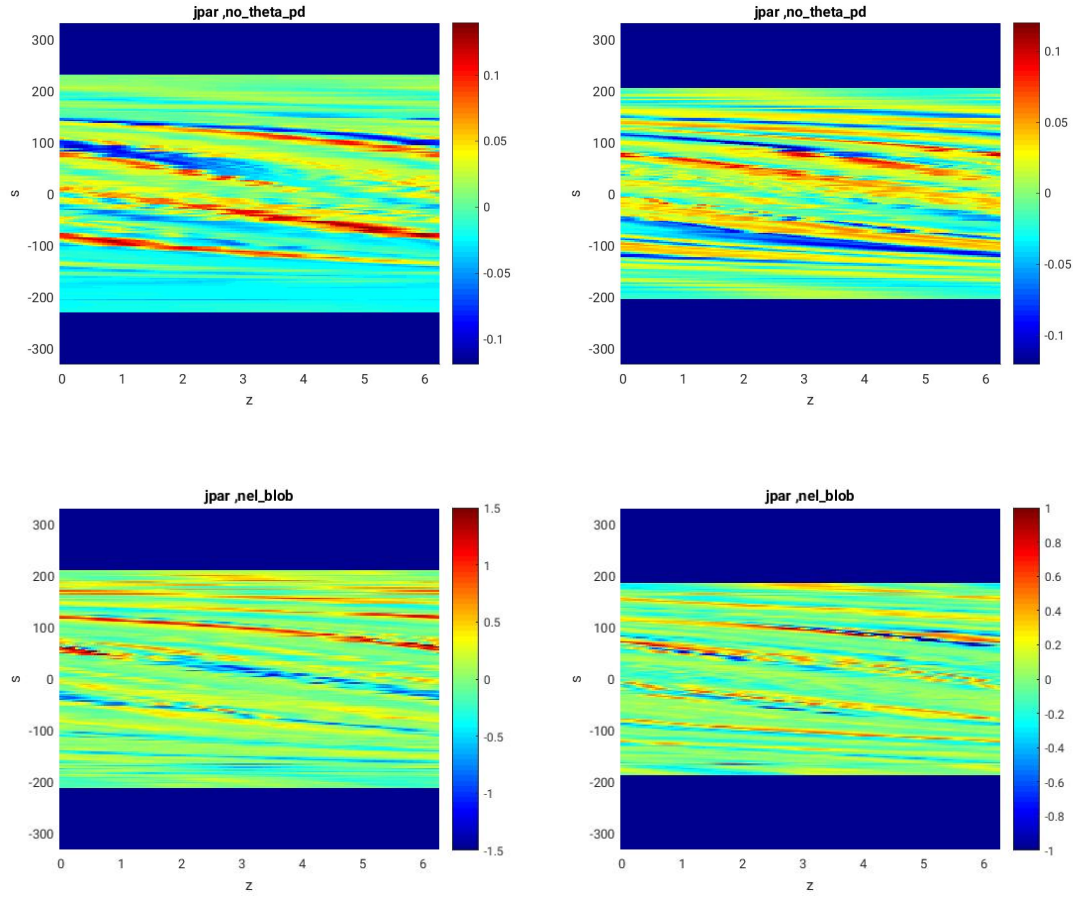
Figure 3.13 – Parallel current structure of blobs in different blob regimes. Top left is an RB blob, in which the current loop closes within the main part of the SOL, not too far from the midplane. For the RX (top right) and C_i blobs (bottom left) the current loop closes around the X point region and for the C_s blob the parallel current perturbation reaches right to the wall.
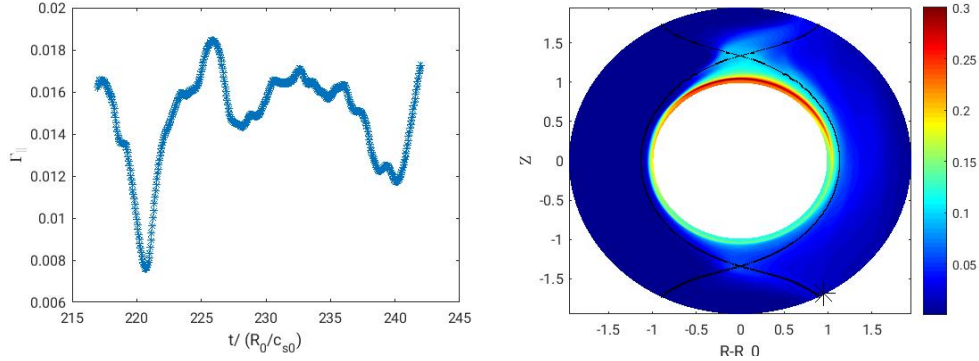
Figure 3.14 – Parallel flux of electron density as a function of time (left), near the lower LFS divertor leg (black marker on the right figure), which does not show an intermittent character.

covered by blobs to total SOL area) and v_b the average blob velocity. The x average is taken from the LCFS to the wall. We address each of these quantities in turn.

We estimate $\sigma_b = 2n_b/\ln(2)$, i.e. as the ratio of the average number of particles in a blob, $2\pi n_b a_x a_y/\ln(2)$, where we assume blobs have on average a Gaussian shape with HWHM a_x and a_y and peak density $\bar{n}' + n_b$, and the average blob area, $A_b = \pi a_x a_y$. Since $\bar{n}'$ decreases radially, $n_b/\bar{n}'$ remains approximately constant over the blob lifetime despite parallel draining, so we combine the definition of a blob and the estimate of the $\tilde{n}/\bar{n}$ in the near SOL to estimate $n_b \sim 3\tilde{n} \sim 3\bar{n}/(L_n k_x)$.

The packing fraction $f_b = N_b A_b/(A_{SOL})$ where N_b is the number of blobs, requires an estimate of the blob size. We observe that the blob size remains approximately constant as the blobs propagate (as observed experimentally in AUG [11]) and that blobs tend to be circular, maximising their Kelvin-Helmholtz stability [75], so we estimate their size as the geometric mean of the near SOL eddy dimensions $a_x \sim a_y \sim \pi/(2\sqrt{k_x k_y})$. We infer therefore from the results for the near SOL analysis that blob size increases with resistivity, a trend observed both in our simulations (Fig. 3.15) and experimentally [95].

We now turn to the estimation of N_b. In steady state, the blob generation and loss rates are equal. Since blobs are generated from instabilities of wavelength $2\pi/k_y$ we expect the generation rate to be proportional to $L_y k_y/(2\pi)$. The generation timescale has previously been proposed as determined by poloidal flow shear [28] or a combination of flow shear and mode phase velocity [27], [14]. In the presence of hot ions, strong $E \times B$ flow shear may be present [101], [69]. However, in our simulations we find the flow shear timescale, $\partial_x v_{E \times B}$, almost an order of magnitude less than the observed generation timescale and not to scale with v and q as observed. We reason that blobs are created because the linear instability saturates as the local density gradient is removed and the resulting density perturbation moves outwards without the streamer being *refilled* from the core, a case which was studied in a
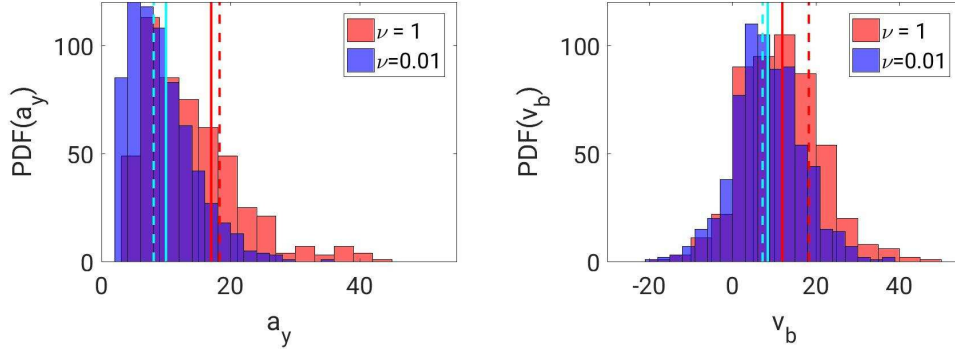
Figure 3.15 – Distribution of the vertical size (left) and radial velocity (right) of the blobs at $\nu = 1$ and $\nu = 0.01$ with $q = 6.5$. The mean sizes and velocities are shown with a solid line and the predictions with a dashed line.

basic plasma physics device in [60]. Hence, the generation rate is limited by the time taken for the blob to travel one radial wavelength of the driving instability, $4a_x/v_b$, and allow the density gradient to be re-established, which is consistent with the simulations. Taking the blob lifetime as the time taken to cross the domain, the loss rate is $N_b v_b/L_x$ where L_x is the distance between the LCFS and the wall. Hence $N_b = 4\pi^2 L_x L_y/(k_x k_y)$. Using the above relations, we find $f_b \approx \pi/16$, independent of SOL parameters. While the universality of f_b is well supported by the simulation data, the predicted value is an overestimate (likely because we assume all blobs cross the entire radial domain) and a better estimate is $f_b = 0.1$.

The average blob velocity, v_b, is deduced from the average blob size, a_x and a_y, according to the two region model scaling relations derived above. We saw that the normalised velocity is related to the normalised size by $\hat{v} = \Im(\hat{\omega})\hat{a}^{1/2}$ and $\hat{\omega}$ is given by the relevant dispersion relation, either Eq. (3.30) or Eq. (3.31). The average blob velocity is estimated by $v_b = 0.5\hat{v}v_*$, where the factor 0.5 is obtained by comparing the scaling with the simulation results and accounts for the fact that our estimate is an upper limit that neglects various mechanisms slowing the blobs [94]. A comparison between the two-region model $a - \nu$ scalings and the detected blobs is shown in Fig. 3.12. Whilst there is considerable scatter around the theoretical scalings (for the reasons described in Ref. [94]), the parallel current structure of the blobs is consistent with the current closure mechanism proposed for its $\Lambda - \Theta$ regime, as shown in Fig. 3.13.

Using the balance of flux divergences, as described above, we find L'_n, for which the full numerical result is shown in Fig. 3.10. For typical experimental parameters, most blobs are in

the $\Lambda > \Theta$ regime, for which

$$L'_n = \frac{7.3 f_b L_\parallel \omega_i^{0.0167} (R_0 m_i \tau_e)^{0.00833} \Gamma_{LCFS}^{1.04}}{m_e^{0.00833} \bar{c}_s^{1.05} \bar{n}^{1.04} (1+\eta) q^{0.0167} \rho_s'^{0.1}} \tag{3.36}$$

is of the order several mm for typical experimental parameters. We note that since $\Lambda \propto R_0$ and $\Theta \propto R_0^{1.46}$, larger device will likely have blobs in the $\Theta > \Lambda$, $\Lambda > 1$ regime, for which

$$L'_n = \frac{94.8 f_b L_{\parallel 1}^2 L_\parallel \Gamma_{LCFS}^{5/3} m_i^{17/15} \tau_e^{2/15} \rho_s'^{7/5} \omega_i^{19/15}}{R_0^{28/15} \bar{n}^{5/3} m_e^{17/15} c_s^{14/5} \rho_s^{2/5} (1+\eta)^{7/5} q^{34/15}} \tag{3.37}$$

In Fig. 3.10 we show ν_b, Γ' and L'_n as a function of ν, q and Γ_{LCFS}. We observe that Γ' increases with ν and with q, primarily due to variation in ν_b and to a lesser extent σ_b, as suggested in [83]. The increase in ν_b follows from the $\hat{a} - \hat{\nu}$ scaling. Such an increase has also been observed in gyrofluid simulations [35]. The increase in L'_n with resistivity is well documented experimentally [14]. The predicted L'_n is compared to the simulation result in Fig. 3.16. As for the near SOL, we find good agreement between theory and simulation.
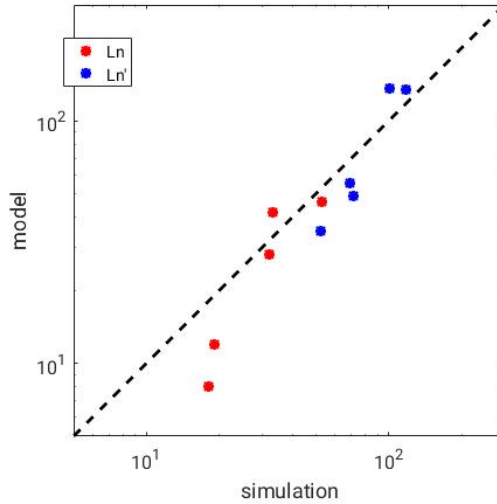

Figure 3.16 – Comparison of the model and simulation L_n and L'_n.

4 Turbulence and flows in unbalanced double-null configurations

4.1 Introduction

One of the possible main advantages of the double-null (DN) configuration is the ability to spread the heat load over the the four divertor legs and in particular over the two LFS strike points. One might expect a more equal spreading between the two LFS strike points than between the inner and outer strike points of a single null (SN) configuration [10] [16]. Since both these strike points are at greater major radius than the SN inner strike point, the heat load is also spread over a larger area for a given heat flux decay length [73], [10].

However, a perfect DN configuration is impossible to control, rather in practice the magnetic configuration cycles between lower single null (LSN), balanced DN and upper single null (USN) geometries [73]. In the LSN, the lower X point lies closer to the magnetic axis, hence the separatrix associated with the lower X point forms the LCFS and represents the primary separatrix. The separatrix associated with the upper X point lies entirely outside the LCFS and is therefore a secondary separatrix. We refer to the region between the two separatrices as the interseparatrix region (ISR). For the USN, it is the upper X point that is closer to the core and its associated separatrix forms the LCFS, whilst for the balanced case they are equidistant from the core so there is only one separatrix that is also the LCFS. The variation in magnetic topology can be quantified by the distance between the separatrices associated with the upper and lower X points at the midplane, among other methods.

The dependence of the heat flux sharing on the degree of magnetic balance has been studied experimentally on MAST [16], DIII-D [70] and C-Mod [10] tokamaks. In Ref. [16] the power deposition was compared for lower single null (LSN) and balanced DN discharges, in L and H mode. In the LSN configuration, the heat loads at the inner and outer strike points were measured, and more power was deposited at the outboard side in both L and H mode. In the balanced configuration, more power went to the lower LFS than the upper LFS leg in L-mode and inter-ELM H mode periods.

In Ref. [70] the heat flux sharing between the upper and lower divertors was found to be less

sensitive to the magnetic balance than the in/out power sharing. A higher heat flux was found at the lower divertor compared to the upper divertor, whilst a higher particle flux was found at the upper divertor. The heat and particle fluxes were interpreted in terms of the $E \times B$ flow across the private flux regions.

In Ref. [10], it was found equal power sharing between the upper and lower outer legs occurs close to a balanced double null that in L mode. Non-zero power to the inner divertor legs was measured. The results could be explained in terms of heat flux mapping along the magnetic field lines.

In this Chapter we approach the study of the heat flux distribution among the four divertor legs in balanced and unbalanced DN configurations using simulations run with a new version of GBS upgraded to employ an elliptic rather than circular toroidal coordinate system. This is a necessary step because the details of the magnetic field shape around the X point may have a significant effect on the fluxes in this region, hence a realistic X point shape is required. The use of an elliptic domain means magnetic fields with more realistic elongation can be simulated, so the radial rescaling of the flux function described in Section 3.2 is no longer required.

In Section 4.2, we describe the choice of a new coordinate system. The numerical verification of its implementation in GBS is described in Section 4.3. We then explain the system of magnetic flux coordinates we use in the analysis in Section 4.4. Section 4.5 describes the three simulations that we consider for the present study, that is a LSN, a balanced DN and a USN configuration. Finally in Section 4.7, we present the simulation results and, for the three magnetic fields, compare the heat loads to the four divertor legs, which are interpreted in terms of the $E \times B$, parallel and diamagnetic fluxes.

4.2 An elliptical coordinate system for the simulation of double null configurations

We describe the coordinate system introduced to properly describe turbulence in DN configurations. Since tokamak plasmas tend to be vertically elongated, an elliptic domain in the poloidal plane has been chosen, elongated in the vertical direction.

4.2.1 Definition of the elliptic coordinates

When defining the elliptical coordinates, we target simplicity of coordinate definition, regular grid spacing and absence of coordinate singularities. For these reasons, a non-orthogonal coordinate system was chosen. Like the circular-toroidal system described in Chapter 3, the elliptic coordinate system has two coordinate directions in the poloidal plane (a and v), and

one coordinate, ϕ is the toroidal angle. We define the elliptical coordinate basis (a, v, ϕ) as

$$
\begin{cases}
a = \sqrt{R_1^2 + \frac{Z^2}{k^2}} \\
\tan v = \frac{Z}{kR_1} \\
\tan \phi = \frac{Y}{X}
\end{cases}
\tag{4.1}
$$

where (X, Y, Z) are Cartesian coordinates centred at the tokamak axis of symmetry on the midplane, with Z the vertical direction and X and Y the orthogonal coordinates on the equatorial midplane. We also define the major radius $R = \sqrt{X^2 + Y^2}$ and the distance from the magnetic axis projected to the midplane $R_1 = R_0 - R = a \cos v$, where R_0 is the major radius of the magnetic axis. The parameter $k > 1$ is the ratio of the major and minor axes of the ellipse defined by $a = $ const and the coordinate a is the ellipse minor radius. The coordinate v is chosen to be different to θ in order to improve the resolution at the extremity of the ellipse. An added advantage of this choice is that the Jacobian does not depend on the coordinate v and this simplifies the computation of the operators.

We also introduce the inverse coordinate transformation

$$
\begin{cases}
X = (R_0 - a \cos v) \cos \phi \\
Y = (R_0 - a \cos v) \sin \phi \\
Z = ka \sin v
\end{cases}
\tag{4.2}
$$

The coordinate system is shown diagrammatically in Fig. 4.1.

4.2.2   Derivation of the GBS operators in elliptic coordinates

We now derive the GBS operator in this newly introduced coordinate system. We start by evaluating the covariant basis vectors:

$$
e_a = \begin{pmatrix} -\cos v \cos \phi \\ -\cos v \sin \phi \\ k \sin v \end{pmatrix} \quad
e_v = \begin{pmatrix} a \sin v \cos \phi \\ a \sin v \sin \phi \\ ak \cos v \end{pmatrix} \quad
e_\phi = \begin{pmatrix} -R \sin \phi \\ R \cos \phi \\ 0 \end{pmatrix}
\tag{4.3}
$$

and the contravariant basis vectors

$$
e^a = \begin{pmatrix} -\cos v \cos \phi \\ -\cos v \sin \phi \\ \frac{1}{k} \sin v \end{pmatrix} \quad
e^v = \begin{pmatrix} \frac{1}{a} \sin v \cos \phi \\ \frac{1}{a} \sin v \sin \phi \\ \frac{1}{ak} \cos v \end{pmatrix} \quad
e^\phi = \begin{pmatrix} -\frac{1}{R} \sin \phi \\ \frac{1}{R} \cos \phi \\ 0 \end{pmatrix}
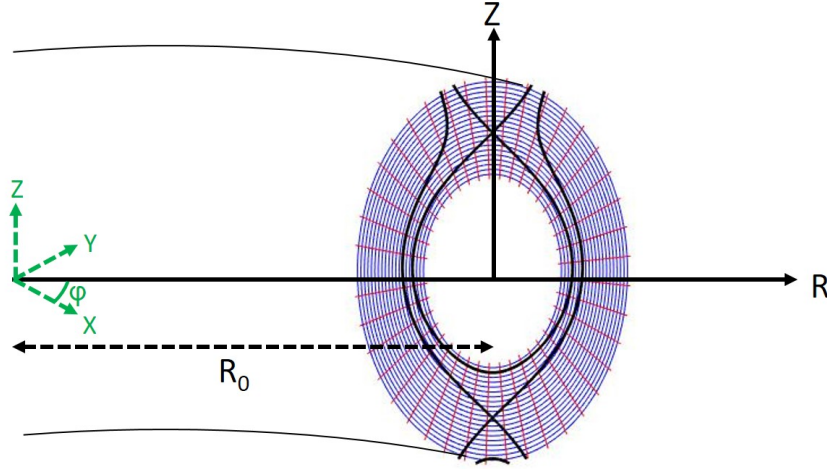\tag{4.4}
$$

49

Figure 4.1 – Coordinate surfaces for the elliptic coordinate system. The torus major axis is R_0. Surfaces of constant a are shown in blue and constant v in red.

The metric tensor and the inverse metric tensor are then given by:

$$G = \begin{pmatrix} g_{aa} & g_{av} & 0 \\ g_{av} & g_{vv} & 0 \\ 0 & 0 & g_{\phi\phi} \end{pmatrix} \quad G^{-1} = \begin{pmatrix} g^{aa} & g^{av} & 0 \\ g^{av} & g^{vv} & 0 \\ 0 & 0 & g^{\phi\phi} \end{pmatrix} \tag{4.5}$$

with the components

$$\begin{aligned}
g_{aa} &= \cos^2 v + k^2 \sin^2 v & g^{aa} &= \cos^2 v + \tfrac{1}{k^2} \sin^2 v \\
g_{av} &= a(k^2 - 1) \cos v \sin v & g^{av} &= \tfrac{k^2-1}{ak^2} \cos v \sin v \\
g_{vv} &= a^2(\sin^2 v + k^2 \cos^2 v) & g^{vv} &= \tfrac{1}{a^2}(\sin^2 v + \tfrac{1}{k^2} \cos^2 v) \\
g_{\phi\phi} &= R^2 & g^{\phi\phi} &= \tfrac{1}{R^2}
\end{aligned} \tag{4.6}$$

where we note the presence of off-diagonal terms due to the non-orthogonality of the coordinate basis. Using $J = \sqrt{\det G}$, the Jacobian is given by:

$$J = aRk \tag{4.7}$$

We now need to evaluate the components of the operators given in Eqs. (2.23-2.27) in the

elliptical coordinates. First, we express the magnetic field, in physical units as

$$\mathbf{B} = F(\tilde{\psi}(a,v))\tilde{\nabla}\phi + \tilde{\nabla}\phi \times \left(\frac{\partial\tilde{\psi}}{\partial a}\tilde{\nabla}a + \frac{\partial\tilde{\psi}}{\partial v}\tilde{\nabla}v\right) \tag{4.8}$$

where $\tilde{\psi}$ is the flux function in physical units. We will consider $F(\tilde{\psi}) = R_0 B_0$ in the following. The magnetic field can be expressed in either covariant or contravariant components:

$$\mathbf{B} = B_a e^a + B_v e^v + B_\phi e^\phi = B^a e_a + B^v e_v + B^\phi e_\phi \tag{4.9}$$

where the components are given by

$$
\begin{aligned}
B_a &= \tfrac{1}{J}(g_{av}\tfrac{\partial\tilde{\psi}}{\partial a} - g_{aa}\tfrac{\partial\tilde{\psi}}{\partial v}) & B^a &= -\tfrac{1}{J}\tfrac{\partial\tilde{\psi}}{\partial v} \\
B_v &= \tfrac{1}{J}(g_{vv}\tfrac{\partial\tilde{\psi}}{\partial a} - g_{av}\tfrac{\partial\tilde{\psi}}{\partial v}) & B^v &= \tfrac{1}{J}\tfrac{\partial\tilde{\psi}}{\partial a} \\
B_\phi &= B_0 R_0 & B^\phi &= \tfrac{B_0 R_0}{R^2}.
\end{aligned}
\tag{4.10}
$$

We also evaluate the norm of the magnetic field:

$$B^2 = \frac{B_0^2 R_0^2}{R^2} + \frac{1}{k^2 a^2 R^2}\left[g_{vv}\left(\frac{\partial\tilde{\psi}}{\partial a}\right)^2 + g_{aa}\left(\frac{\partial\tilde{\psi}}{\partial v}\right)^2 - 2g_{av}\frac{\partial\tilde{\psi}}{\partial a}\frac{\partial\tilde{\psi}}{\partial v}\right]. \tag{4.11}$$

These expressions are substituted into Eqs. (2.23-2.27) and simplified in an analogous manner to that described in Ref. [69]. More precisely, to perform the simplification, we define the normalised coordinate $\bar{a} = a/a_*$ where a_* is radial coordinate of the domain inner boundary at the midplane. We then have the following ordering for the equilibrium quantities:

$$\frac{\partial\psi}{\partial a} \sim \frac{1}{a_*} \to \frac{\partial\psi}{\partial\bar{a}} \sim 1, \quad \frac{1}{a}\frac{\partial\psi}{\partial v} \sim \frac{1}{a_*} \to \frac{1}{\bar{a}}\frac{\partial\psi}{\partial v} \sim 1, \quad \frac{\partial\psi}{\partial\phi} = 0 \tag{4.12}$$

where $\psi = \tilde{\psi}/(a^2|B_0|)$ is the normalised flux function. For the fluctuating quantities, we normalise the poloidal coordinates to ρ_{s0} (the scale length of the fluctuations), we then define the dimensionless coordinate $x = (a - a_*)/\rho_{s0}$ and $y = a_* v/\rho_{s0}$, which have the ordering

$$\frac{\partial f}{\partial a} \sim \frac{1}{\rho_s} \to \frac{\partial f}{\partial x} \sim 1, \quad \frac{1}{a}\frac{\partial f}{\partial v} \sim \frac{1}{\rho_s} \to \frac{1}{\bar{a}}\frac{\partial f}{\partial y} \sim 1, \quad \frac{R_0}{R}\frac{\partial f}{\partial\phi} \sim 1. \tag{4.13}$$

We then retain only the terms $O(1)$ or above in the parameters $\delta = \rho_{s0}/a_*$ and $\epsilon = a_*/R_0$. The

geometric operators in Eqs. (2.23-2.27) then become

$$\nabla_\parallel f = \frac{B_0}{|B_0|}\frac{\partial f}{\partial \phi} + \delta^{-1}\frac{1}{k\overline{a}}\left(\frac{\partial \psi}{\partial \overline{a}}\frac{\partial f}{\partial y} - \frac{\partial \psi}{\partial v}\frac{\partial f}{\partial x}\right) \tag{4.14}$$

$$
\begin{aligned}
\nabla_\parallel^2 f = \quad & \frac{\delta^{-2}}{k^2\overline{a}^2}\left((\frac{\partial \psi}{\partial v})^2\frac{\partial^2 f}{\partial x^2} + (\frac{\partial \psi}{\partial \overline{a}})^2\frac{\partial^2 f}{\partial y^2} - 2\frac{\partial \psi}{\partial \overline{a}}\frac{\partial \psi}{\partial v}\frac{\partial^2 f}{\partial x\partial y}\right) \\
& + \delta^{-1}\left(\frac{1}{k^2\overline{a}^2}(\frac{\partial \psi}{\partial v}\frac{\partial^2 \psi}{\partial \overline{a}\partial v} - \frac{\partial \psi}{\partial \overline{a}}\frac{\partial^2 \psi}{\partial v^2}) - \frac{1}{k^2\overline{a}^3}(\frac{\partial \psi}{\partial v})^2\right)\frac{\partial f}{\partial x} \\
& + \delta^{-1}\left(\frac{1}{k^2\overline{a}^2}(\frac{\partial \psi}{\partial \overline{a}}\frac{\partial^2 \psi}{\partial \overline{a}\partial v} - \frac{\partial \psi}{\partial v}\frac{\partial^2 \psi}{\partial \overline{a}^2}) + \frac{1}{k^2\overline{a}^3}\frac{\partial \psi}{\partial \overline{a}}\frac{\partial \psi}{\partial v}\right)\frac{\partial f}{\partial y} \\
& + \delta^{-1}\frac{B_0}{|B_0|}\frac{2}{k\overline{a}}(\frac{\partial \psi}{\partial \overline{a}}\frac{\partial^2 f}{\partial y\partial \phi} - \frac{\partial \psi}{\partial v}\frac{\partial^2 f}{\partial x\partial \phi}) + \frac{\partial^2 f}{\partial \phi^2} + O(\epsilon)
\end{aligned}
\tag{4.15}
$$

$$C(f) = \frac{B_0}{|B_0|}\frac{1}{k}\left(\sin v \frac{\partial f}{\partial x} + \frac{\cos v}{\overline{a}}\frac{\partial f}{\partial y}\right) + O(\epsilon) \tag{4.16}$$

$$[\Phi, f] = \frac{1}{k\overline{a}}[\Phi, f]_{a,v} + O(\epsilon) \tag{4.17}$$

Where we defined $[\Phi, f]_{x,y} = \partial_x\Phi\partial_y f - \partial_y\Phi\partial_x f$.

$$
\begin{aligned}
\nabla_\perp^2 f = \quad & \frac{1}{\overline{a}}(\sin^2 v + \frac{1}{k^2}\cos^2 v)\frac{\partial^2 f}{\partial y^2} + (\cos^2 v + \frac{1}{k^2}\sin^2 v)\frac{\partial^2 f}{\partial x^2} \\
& + 2\frac{(k^2-1)\sin v\cos v}{\overline{a}k^2}\frac{\partial^2 f}{\partial x\partial y} + O(\epsilon)
\end{aligned}
\tag{4.18}
$$

We note that these operators reduce the toroidal expressions given in Ref. [69] when $k = 1$.

4.3 Numerical verification of the GBS implementation

We ensure the correct implementation of the elliptical coordinates in GBS by testing each operator individually. This is done by evolving GBS by one timestep with all but one field frozen. An analytical expression for this field is chosen so that the application of the operator gives a known result. Performing this procedure with a series of different sized grids allows us to confirm that the numerical error converges at the expected rate, which is the order of the numerical scheme [79].

Operator	Test Function	Expected Result
$\nabla_\parallel f$	ψ	0
$\nabla_\parallel^2 f$	ψ	0
$C(f)$	$ka\sin(v)$	$C(f) = \left(\frac{B_0}{\|B_0\|}\right)\frac{\rho_{s0}}{a_*}$
$[f_1, f_2]$	$[\frac{\partial \psi}{\partial x}, x] + [\frac{\partial \psi}{\partial y}, y]$	0

Table 4.1 – Test functions for the GBS operators in elliptic coordinates.

The grid sizes used are given by:

$$N_x = N_{x0}2^{n_g}$$
$$N_y = N_{y0}2^{n_g}$$
$$N_z = N_{z0}2^{n_g}$$

(4.19)

where $N_{x0} = 20$, $N_{y0} = 30$ and $N_{z0} = 4$, and n_g varies between 0 to 4. We study the convergence rate using the L_2 and L_∞ norms, given by:

$$L_2 = \sqrt{\frac{\sum\limits_{i,j,k} \Delta_{ijk}}{N_x N_y N_z}}$$
$$L_\infty = \max_{i,j,k}(|\Delta_{ijk}|)$$

(4.20)

where Δ_{ijk} is the difference between the numerical and analytical value of the operator applied to the test function at the ijk grid point, where i, j and k reference the x, y and z grid directions. The L_2 norm is a measure of the average error over whole grid and the L_∞ norm is a measure of the maximum error. Table 4.1 shows the test functions and expected results for the parallel gradient, parallel diffusion, curvature and Poisson bracket operators, all of which converged at the expected fourth order rate, with similar results to that shown for the parallel gradient in Fig. 4.2.

The verification of the Laplacian operator is performed in a different way. The Laplacian operator appears in Poisson's equation: $\nabla_\perp^2 \Phi = \omega$ and is discretized using a fourth order finite difference scheme.

To verify that this operation is correctly implemented, we use the method of manufactured solutions [79]. Precisely, we choose a test function f and we apply the Laplacian operator analytically on the test function using Mathematica. In the GBS code, the value of ω is set to correspond to this result: $\omega = \nabla_\perp^2 f$. By running only one step in the GBS code, we get the value of Φ. If the boundary conditions are set correctly, Φ must be equal to f.

We choose the test function $f = \sin(ax)\sin(by)$, with $a = \frac{2\pi}{L_x}$ and $b = \frac{2\pi}{L_y}$ and periodic boundary conditions for y and Dirichlet boundary condition for x imposing $\Phi(x = 0) = 0$ and $\Phi(x = $
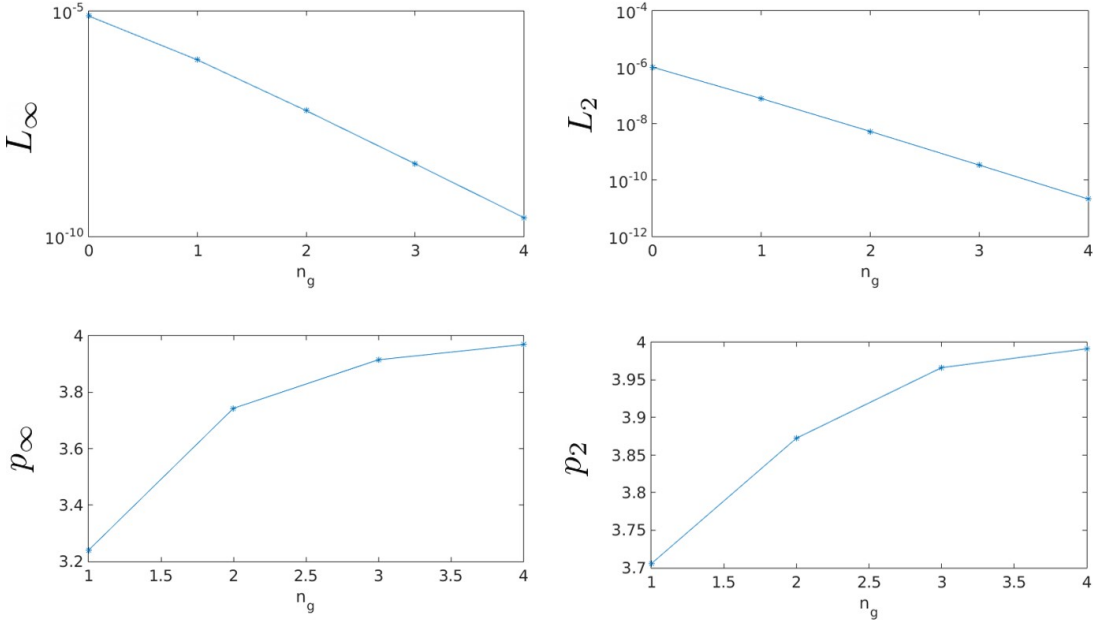
Figure 4.2 – Convergence of the parallel gradient operator. The upper plots show the L_∞ (left) and L_2 (right) norms as a function of grid size. The lower plots show the convergence rates $p_\infty = \ln[L_\infty(n_g)/L_\infty(N_g+1)]/\ln(2)$ (left) and $p_2 = \ln[L_2(n_g)/L_2(N_g+1)]/\ln(2)$ (right), which we expect to approach the order of the numerical scheme as the grid size tends to infinity, in this case four.

$L_x) = 0$. This choice of function $f = \sin(ax)\sin(by)$ implies:

$$\omega = \sin(by)\left[\frac{2ab(k^2-1)\cos(ax)\cos^2(by)}{k^2(1+bx)} - \frac{b^2\sin(ax)(\frac{\cos^2(by)}{k^2}+\sin^2(by))}{(1+bx)^2} \right.$$
$$\left. -a^2\sin(ax)(\cos^2(by) + \frac{\sin^2(by)}{k^2}) \right] \tag{4.21}$$

The results of the convergences of $\nabla_\perp^2 \Phi - \nabla_\perp^2 f$ are shown on Fig.4.3. The norm L_∞ seems to converge at order four but the norm L_2 only reaches order three, probably because the boundary conditions are implemented only to second order.

4.4   Magnetic Coordinates

In the balanced DN configuration, there are five topologically separated regions: the closed flux (CF), low field side (LFS), high field side (HFS), upper private plasma (UPP) and lower private plasma (LPP) regions. When the double null is unbalanced, there is a sixth region that we refer to as the inter-separatrix region (ISR). These are shown in Fig. 4.4.
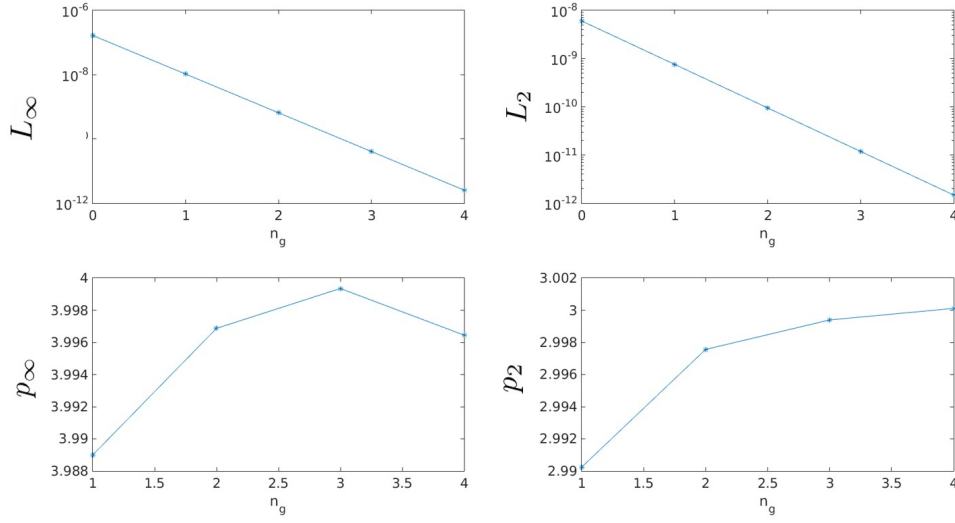
Figure 4.3 – Convergence analysis for the Laplacian operator $\nabla_\perp^2 \Phi - \nabla_\perp^2 f$. The upper plots show the L_∞ (left) and L_2 (right) norms as a function of grid size. The lower plots show the convergence rates $p_\infty = \ln[L_\infty(n_g)/L_\infty(N_g+1)]/\ln(2)$ (left) and $p_2 = \ln[L_2(n_g)/L_2(N_g+1)]/\ln(2)$ (right), which we expect to approach the order of the numerical scheme as the grid size tends to infinity, in this case four. This is the case for p_∞ but not for p_2, we attribute this to the boundary conditions, which are not implemented at fourth order.

To better understand the mechanism behind the distribution of the heat flux in such a complex topology, it is useful to project the vector components of the heat fluxes, such as the $E \times B$ flux, onto a magnetic coordinate basis. The system we use consists of the toroidal coordinate ϕ, a flux coordinate,

$$\rho = (\psi - \psi_{LCFS})\frac{x_{max} - x_{LCFS}}{\psi_{max} - \psi_{LCFS}}, \tag{4.22}$$

in practice a rescaling of the flux function, and a binormal coordinate χ that is orthogonal to both ρ and χ. The value of χ is found by integrating the arc length along the outer separatrix in units of ρ_{s0}, starting in the high field side at midplane and going in the direction of increasing v. The arc length is given by:

$$dS = \sqrt{g_{ij}du^i du^j} = \sqrt{g_{xx}dx^2 + g_{yy}dy^2 + 2g_{xy}dxdy}. \tag{4.23}$$

These definitions are such that ρ and χ have the same order of magnitude as x and y.

In order that χ is continuous and single-valued within a given topological region (as shown in Fig. 4.5), we integrate dS along the divertor legs as follows: when passing from the extremity
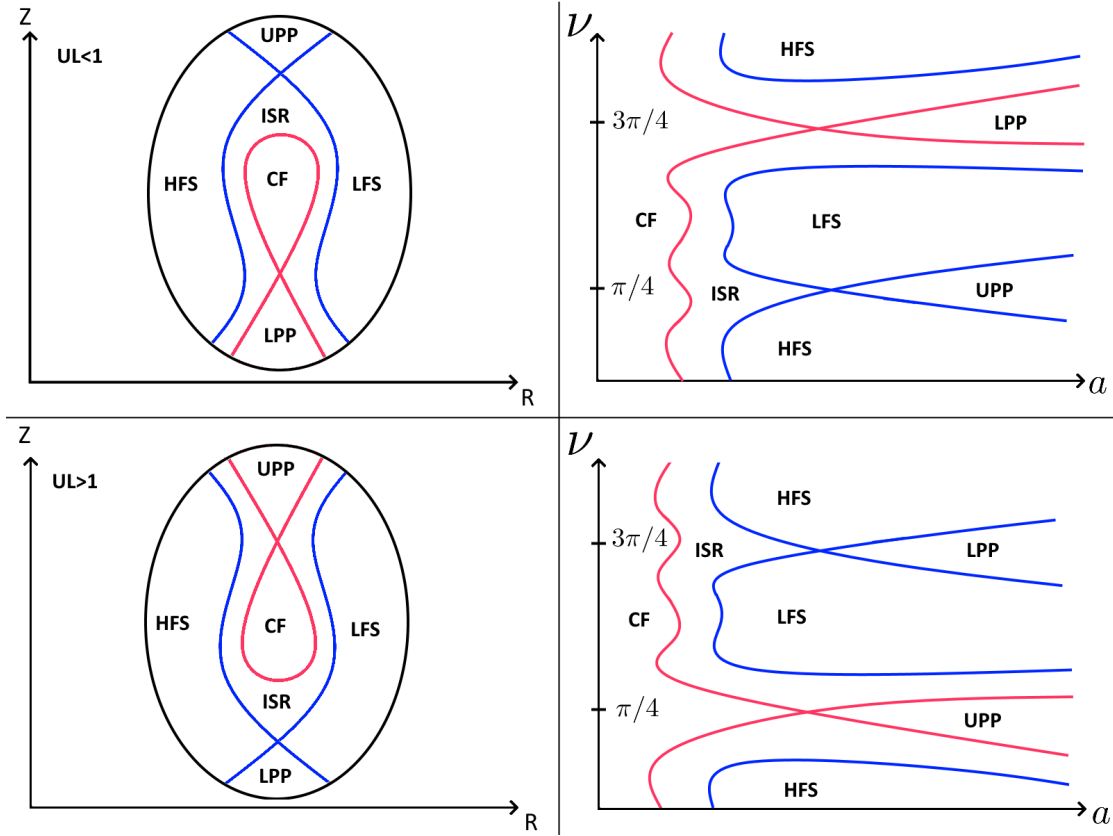
Figure 4.4 – Topological regions in double null configurations.

of one leg to the other one, for example on Fig. 4.6 from point **B** to point **C**, χ is decreased of $\Delta_X \chi$ in order to keep the continuity of χ at the X-point, where $\Delta_X \chi$ is the sum of the arc lengths between the point **A** to the point **B** and between the point **C** to the point **D**. In this way the value of χ at the point **A** is equal to χ at the point **D**. The same method is applied when passing from point **F** to point **G** in order for χ to have only one value at the X point, (point **E**).

Using the fact that the coordinate χ is defined to be perpendicular to the coordinate ρ in the $R - Z$ plane, we can compute the contours of $\chi = $ cnst in the $x - y$ grid. Knowing the value of χ along the outer separatrix, we use the contours of χ constant to find the value of χ in every region. The intersections of the χ contour and the ρ contour form the grid points of the magnetic coordinate grid. The grid is defined such that $\Delta\chi$ and $\Delta\rho$ are uniform.

The values of x, y, R_1 and Z in the $\rho - \chi$ grid are computed by interpolating their value at every intersection of the contours of χ constant and the contours of ρ constant. The arrays $x(\rho, \chi)$ and $y(\rho, \chi)$ are then used to interpolate the simulation quantities onto the ρ, χ grid.
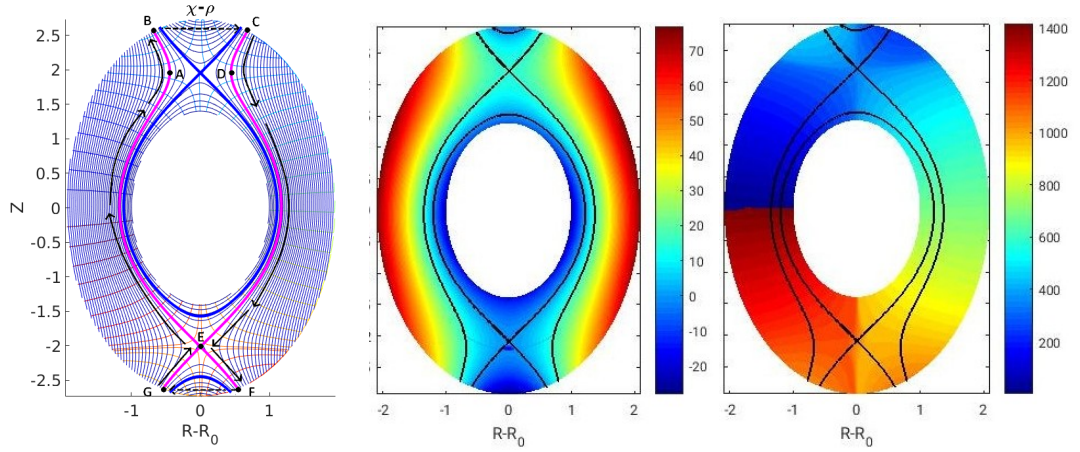
Figure 4.5 – χ-ρ coordinates in an unbalanced double null configuration. Coordinate surfaces (left), colour plot of ρ (centre) and colour plot of χ (right) showing the continuity of the coordinates and single-valuedness within a single topological region.

4.4.1   Analytical computation of χ derivatives

In the following analysis, we project the $E \times B$ flux, $\Gamma_E = n\mathbf{v}_E$, and the diamagnetic flux, $\Gamma_* = n\mathbf{v}_*$, (where $\mathbf{v}_E$ and $\mathbf{v}_*$ are defined in Eqs. (2.7) and (2.10)) in the χ and ρ directions, that is to say parallel and perpendicular to the flux surfaces. For each flux vector, we wish to evaluate

$$\Gamma^\chi = \Gamma \cdot \nabla \chi = \Gamma^x \frac{\partial \chi}{\partial x}\bigg|_y + \Gamma^y \frac{\partial \chi}{\partial y}\bigg|_x \tag{4.24}$$

and

$$\Gamma^\rho = \Gamma \cdot \nabla \rho = \Gamma^x \frac{\partial \rho}{\partial x}\bigg|_y + \Gamma^y \frac{\partial \rho}{\partial y}\bigg|_x. \tag{4.25}$$

Using Eq. (4.22), it can be seen that the ρ derivatives, $\frac{\partial \rho}{\partial x}\big|_y$ and $\frac{\partial \rho}{\partial y}\big|_x$ are simply a rescaling of the ψ derivatives already in hand. In this section we derive the expressions of $\partial \chi / \partial x)_y$ and $\partial \chi / \partial y)_x$ analytically, starting from the orthogonality condition in the $R - Z$ plane:

$$\nabla \chi \cdot \nabla \psi = 0. \tag{4.26}$$

57

In the $R - Z$ Cartesian basis, we write $\nabla \psi$:

$$\begin{pmatrix} \frac{\partial \chi}{\partial R} \\ \frac{\partial \chi}{\partial Z} \end{pmatrix} = \begin{pmatrix} \frac{\partial \chi}{\partial x}\frac{\partial x}{\partial R} + \frac{\partial \chi}{\partial y}\frac{\partial y}{\partial R} \\ \frac{\partial \chi}{\partial x}\frac{\partial x}{\partial Z} + \frac{\partial \chi}{\partial y}\frac{\partial y}{\partial Z} \end{pmatrix} \tag{4.27}$$

and $\nabla \chi$,

$$\begin{pmatrix} \frac{\partial \psi}{\partial R} \\ \frac{\partial \psi}{\partial Z} \end{pmatrix} = \begin{pmatrix} \frac{\partial \psi}{\partial x}\frac{\partial x}{\partial R} + \frac{\partial \psi}{\partial y}\frac{\partial y}{\partial R} \\ \frac{\partial \psi}{\partial x}\frac{\partial x}{\partial Z} + \frac{\partial \psi}{\partial y}\frac{\partial y}{\partial Z} \end{pmatrix} \tag{4.28}$$

from which we find that Eq. (4.26) is satisfied by

$$\begin{cases} \frac{\partial \chi}{\partial x}\frac{\partial x}{\partial R} + \frac{\partial \chi}{\partial y}\frac{\partial y}{\partial R} = -C(\frac{\partial \psi}{\partial x}\frac{\partial x}{\partial Z} + \frac{\partial \psi}{\partial y}\frac{\partial y}{\partial Z}) \\ \frac{\partial \chi}{\partial x}\frac{\partial x}{\partial Z} + \frac{\partial \chi}{\partial y}\frac{\partial y}{\partial Z} = C(\frac{\partial \psi}{\partial x}\frac{\partial x}{\partial R} + \frac{\partial \psi}{\partial y}\frac{\partial y}{\partial R}). \end{cases} \tag{4.29}$$

Solving the two equations in Eq. (4.29) for the two unknowns, $\frac{\partial \chi}{\partial x}$ and $\frac{\partial \chi}{\partial y}$, leads us to the required analytical expression,

$$\frac{\partial \chi}{\partial x}\bigg|_y = -\frac{C\rho_s}{ak}(\frac{\partial \psi}{\partial v}\cos^2 v - a\frac{\partial \psi}{\partial a}(k^2 - 1)\cos v \sin v + \frac{\partial \psi}{\partial v}k^2\sin^2 v) \tag{4.30}$$

$$\frac{\partial \chi}{\partial y}\bigg|_x = \frac{C\rho_s}{a_* k}(a\frac{\partial \psi}{\partial a}k^2\cos^2 v - \frac{\partial \psi}{\partial v}(k^2 - 1)\cos v \sin v + a\frac{\partial \psi}{\partial a}\sin^2 v) \tag{4.31}$$

from which we can compute Γ^χ using Eq. (4.24).

4.5   Magnetic field and simulation parameters

The magnetic field is developed in the same way to the circular simulations, that is based on straight, current carrying wires of infinite length in addition to the plasma current assumed. The wire pairs are introduced at different angles and radii to change the shape of the magnetic field for a total of $2n$ wires. To achieve unbalanced configurations, a new parameter, λ_n, is introduced to multiply the strength of the upper wire relative to the lower one.

The flux function in toroidal coordinate is therefore given by:

$$\psi(r,\theta) = S\log(r) + S\sum_{n=1}^{\text{nwires}}\frac{1}{2}I_n\left(\lambda_n\log(r^2 + a_n^2 - 2ra_n\sin(\theta + \theta_n)) + \log(r^2 + a_n^2 + 2ra_n\sin(\theta + \theta_n))\right)$$

$$(4.32)$$

where S is a constant that sets the strength of the poloidal magnetic field relative to B_0, I_n is the ratio of the current flowing through the nth wire pair with respect to the current flowing through the plasma, a_n is the distance from the magnetic axis to the nth wires and θ_n is the angle between the pair of wires and the z axis.

The derivatives of the flux function are given by:

$$\frac{\partial \psi}{\partial r} = \frac{S}{r} + \sum_{n=1}^{\text{nwires}} SI_n \left(\lambda_n \frac{r - a_n \sin(\theta + \theta_n)}{a_n^2 + r^2 - 2a_n r \sin(\theta + \theta_n)} + \frac{r + a_n \sin(\theta + \theta_n)}{a_n^2 + r^2 + 2a_n r \sin(\theta + \theta_n)} \right)$$
$$\frac{\partial \psi}{\partial \theta} = \sum_{n=1}^{\text{nwires}} SI_n r a_n \cos(\theta + \theta_n) \left(\lambda_n \frac{-1}{a_n^2 + r^2 - 2a_n r \sin(\theta + \theta_n)} + \frac{1}{a_n^2 + r^2 + 2a_n r \sin(\theta + \theta_n)} \right)$$

$$(4.33)$$

We consider three simulations with three different magnetic fields: LSN, balanced DN and USN. In each case, the magnetic field has two X points. We use 6 wire pairs to form the magnetic field. In the balanced case, these are at angles $\theta_n = 0, \pi/2, \pm\pi/4$ and $\pm\pi/32$ at distances $a_n = 4, 3.7, 3.7, 3.7, 3.7, 3.7$ with relative strengths $I_n = 1.25, 0.35, 0.27, 0.27, 0.14, 0.14$, $\lambda_n = 1$ for all n. The USN is the same except that $\lambda_1 = 1.1$ and I_1 is reduced to 1.1905 to keep the total current constant. For the LSN we use the same wire configuration as the USN except $\theta_1 = \pi$ so that the lower rather than the upper wires carries the stronger current. We consider $S = 0.25$ in all cases. The flux surfaces for the three configurations considered are shown in Fig. 4.7. The local q at the midplane in the interseparatrix region is approximately 5.

In the unbalanced configurations, the gap between the inner and outer separatrices is $23\rho_{s0}$, corresponding to approximately $1\,cm$ for typical tokamak parameters. This is somewhat less than the range of $\pm 4\,cm$ obtained experimentally [70], [16] but nevertheless allows sufficient effect on the division of heat flux between the divertor legs to be observed.

For all simulations, the elongation of the domain is $k = 1.4$, the grid size is $n_x = 156, n_y = 450$ and $n_z = 80$. $L_y = 800\rho_{s0}$, the same as the circular case, whilst $L_x = x_{\text{wall}} - x_{\text{inner boundary}} = 137.5\rho_{s0}$. The grid resolution is therefore $\Delta x = 0.881\rho_{s0}$ and $\Delta y = 1.78\rho_{s0}$. The resistivity is $\nu = 1$ for all three simulations and the rest of the parameters are the same as the circular case (see Section 3.3).

4.6 Overview of the simulation results

Equilibrium profiles of p_e, $v_{\parallel e}$ and ϕ are shown in Fig. 4.8. As for the circular simulations, we see little plasma on the HFS outside the LCFS. In contrast to the circular simulation with $\nu = 1.0$, in the balanced DN simulation there is more plasma at the bottom than the top of the closed flux region, and little in either the upper or lower private plasma. On the LFS, all three simulations have very similar $\bar{n}(r)$ profiles at the midplane. There is a single decay length across the separatrix or separatrices of approximately $90\rho_{s0}$, comparable to the outer decay
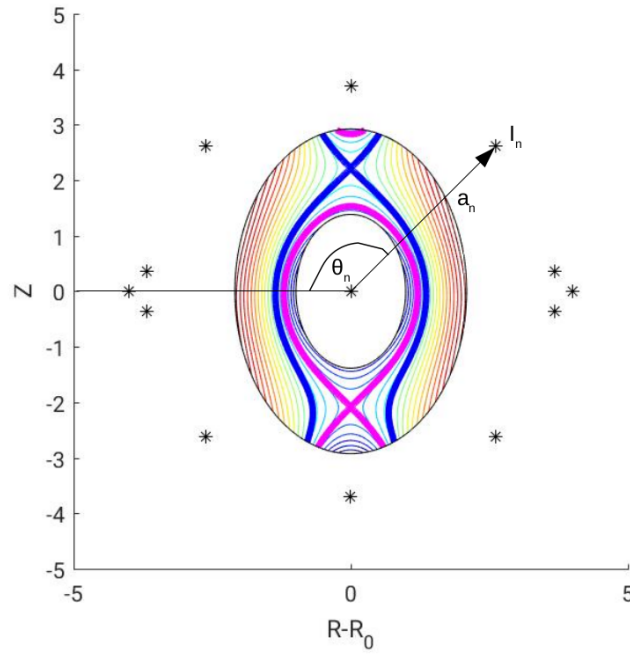
Figure 4.6 – ψ surfaces for the LSN magnetic field, with the definitions of the magnetic field parameters θ_n, a_n and I_n.
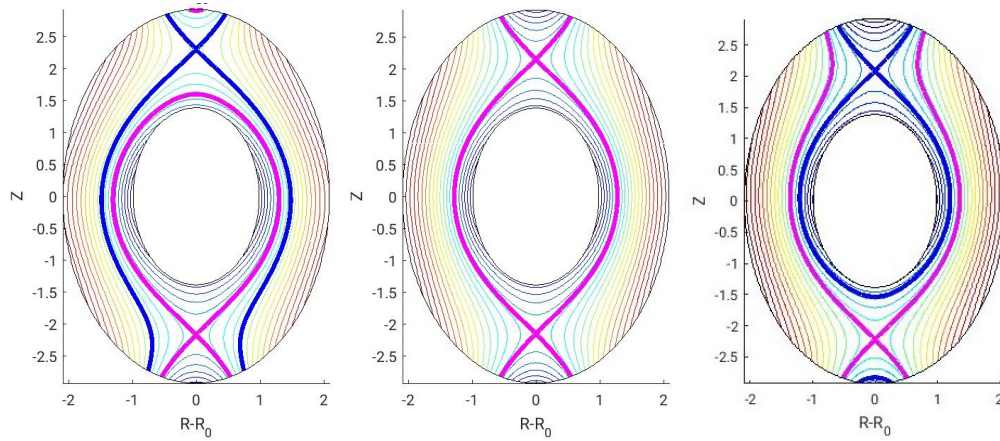

Figure 4.7 – LSN, balanced DN and USN magnetic fields.

length for the $\nu = 1$ simulation on the circular domain.

Whilst the electron pressure is considerably more up-down symmetric than the circular case with $\nu = 1$, up-down asymmetry in ϕ is clearly present, with a higher potential around the upper X point compared to the lower X point. This is the case for all three magnetic configurations. The electric potential is higher on the LFS than HFS, in particular around the midplane, due to the higher n and T_e there. In the LSN configuration, the electrical potential peaks on the outer separatrix, whilst in the USN configuration, the peak is just outside the secondary separatrix and there is also a high potential within the LCFS near the upper X point, leading to a more complex structure, (see Fig. 4.8). Inside the LCFS, ϕ decreases, a pattern also observed in GBS simulations with no inner boundary [33] and experimentally [84] [54]. This phenomenon has been theoretically explained when hot ions are present [101].

In Fig. 4.8 we see stronger parallel flow to the strike points associated with the primary X point in the USN configuration compared to the LSN configuration. This is likely due to the high plasma pressure in the ISR in the USN configuration, which arises because the $E \times B$ flow in the ISR is in the direction from the upper to the lower X point, so turbulent plasma outflow from the midplane is lost at the lower outer leg in the LSN configuration and distributed around the ISR in the USN configuration. Hence the ISR is hotter in the USN configuration, resulting in greater absolute $v_{\parallel e}$.

The fluctuation level in n and ϕ at each point in the poloidal plane is quantified by the standard deviation in the time and toroidal direction variation, shown in Fig. 4.9. The fluctuation pattern in n is very similar to the circular case, with the highest fluctuation level on and just inside the LCFS. In both elliptic and circular simulations, the relative size of the density fluctuations in upper and lower private flux regions is comparable to the relative fluctuation level at the midplane, with a higher fluctuation in both simulations in the upper compared to the lower private flux region. In both cases, the absolute fluctuation level in the private plasma remains much smaller than the absolute fluctuation level at the midplane because the density there is much lower.

The highest fluctuation level in ϕ in the elliptic simulation is on the separatrix, whilst in the circular domain simulation it is further into the open flux region. The absolute and relative fluctuation levels in this region are similar in both simulations. In the elliptic domain simulation, the fluctuation level is considerably lower in the private flux regions compared to the circular simulation.

4.7   Distribution of heat flux between divertor legs

As mentioned in Sec. 4.1, one of the main reasons that the Double Null configuration is interesting is its potential to spread the heat load between several strike points. Since a perfect double null is rarely achieved in practice [73], it is critical to understand how the heat flux sharing depends on the degree of magnetic inbalance, quantified by the distance between the
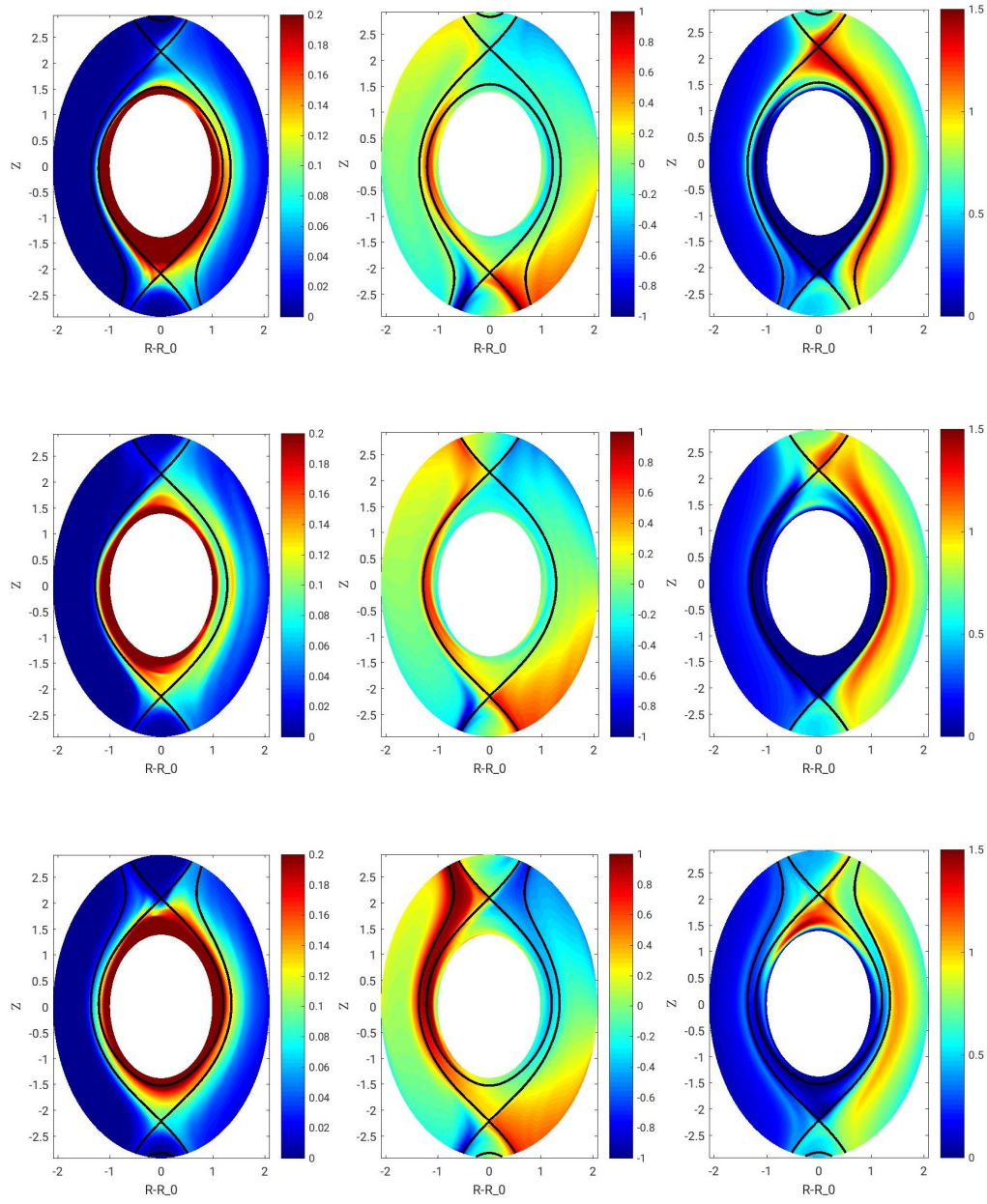
Figure 4.8 – Time and toroidally averaged p_e, $v_{\parallel e}$ and ϕ (left to right).
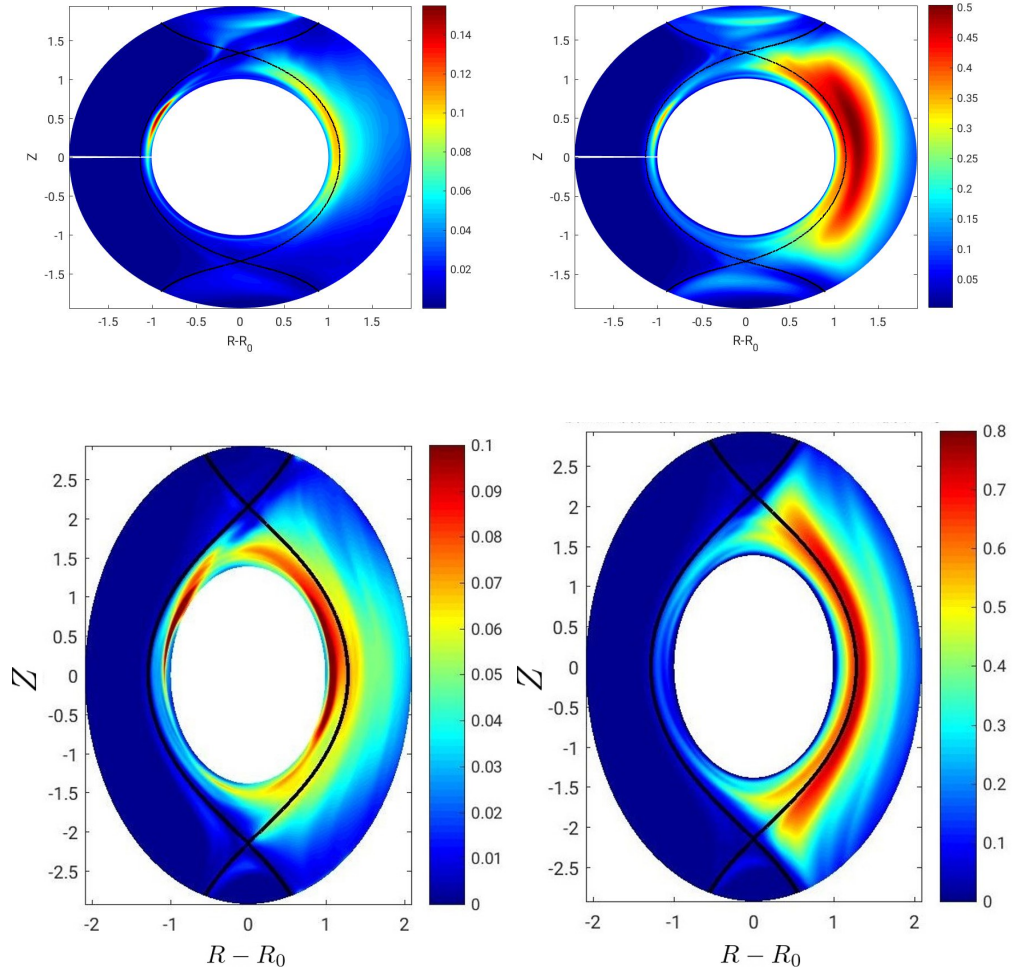
Figure 4.9 – Local standard deviation of n (left) and ϕ (right) in the circular domain and elliptic domain balanced double null simulations. The n fluctuation pattern is similar for the two simulations, with the highest standard deviation on around the LCFS just above the midplane, whilst in ϕ the highest fluctuation level in the circular simulation is outside the LCFS in contrast to the elliptic simulation where it lies right on the LCFS.

inner and outer separatrices. This problem is addressed in this section.

Figure 4.10 – Pie charts of the heat flux sharing.

To visualise the heat flux distribution, we divide the tokamak into four quadrants, bounded by the $y = 0, L_y/4, L_y/2$ and $3L_y/4$ surfaces. We integrate the parallel component of the heat flux $\Gamma_q = nT_e v_{\parallel e}$ over the section of the wall in each quadrant to identify where the heat is being exhausted. The results are shown in Fig. 4.10. We see that most of the heat is lost on the LFS with less than 10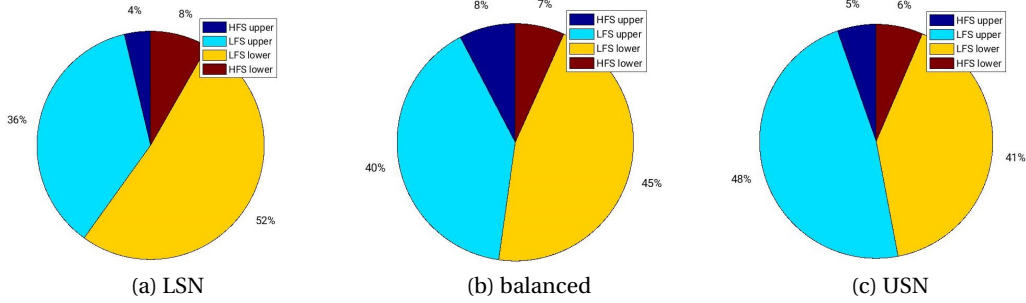% going to each of the HFS legs. The heat load on the LFS is split almost equally between the upper and lower legs, with a few percent more to the lower leg for the balanced and LSN cases and a few percent more to the upper leg for the USN.

In Ref. [10] a model is introduced to describe the division of the heat flux between the upper and lower LFS legs. The model assumes there is radial turbulent transport across the LCFS around the outer midplane and plasma is lost to the wall by parallel flow, resulting in a single heat flux decay length at the divertors. This divertor decay projects to a single pressure decay length at the midplane. The heat exhausted at the divertor leg associated with the primary X point is the radial integral of the heat flux from the inner separatrix (the LCFS) to the wall, whilst the heat exhausted at the divertor leg associated with the secondary X point is the radial integral of the heat flux from the secondary separatrix to the wall. If we assume that the only cross-field transport is at the midplane, the remaining heat transported over the LCFS should be exhausted at the HFS leg associated with the primary X point, however, Ref. [10] does not find the corresponding logistic function a good fit for the in-out power sharing and instead fits a Gaussian function. The 10% power measured at the in Ref. [10] is similar to what we observe in our simulations.

Following this model, the heat fluxes to the upper outer and lower outer divertor legs are expected to be equal in a balanced DN configuration and the fractional difference in the heating power is given by

$$\frac{P_{\text{LFS,l}} - P_{\text{LFS,u}}}{P_{\text{LFS,l}} + P_{\text{LFS,u}}} = \tanh\left(-\frac{\delta R_{sep}}{2L_{pe}}\right) \tag{4.34}$$
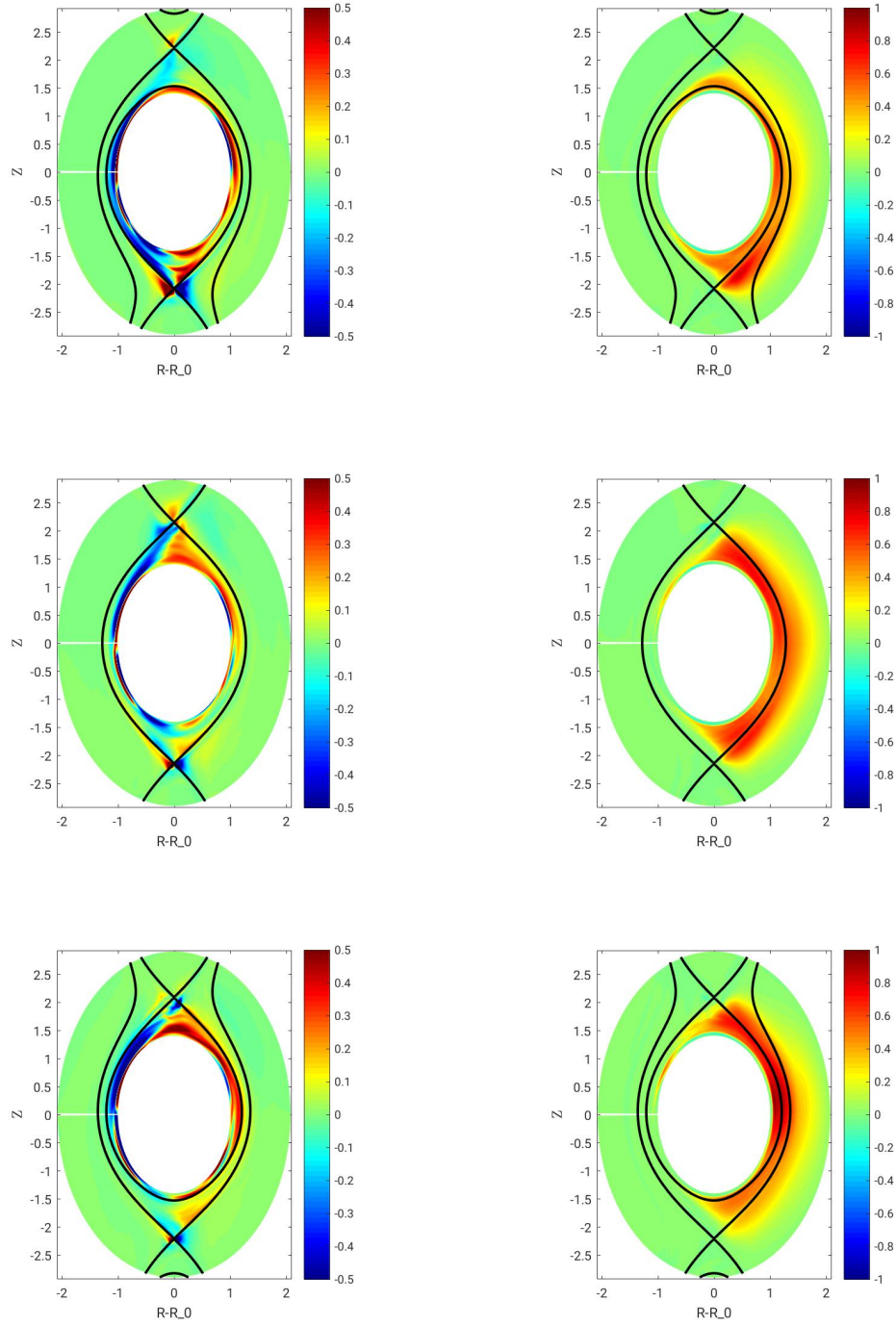
Figure 4.11 – Radial $E \times B$ flux components: $\bar{\Gamma}_E^\rho$ (left) and $\tilde{\Gamma}_E^\rho$ (right). The turbulent component of the flux is more important than the mean field contribution in all three simulations.
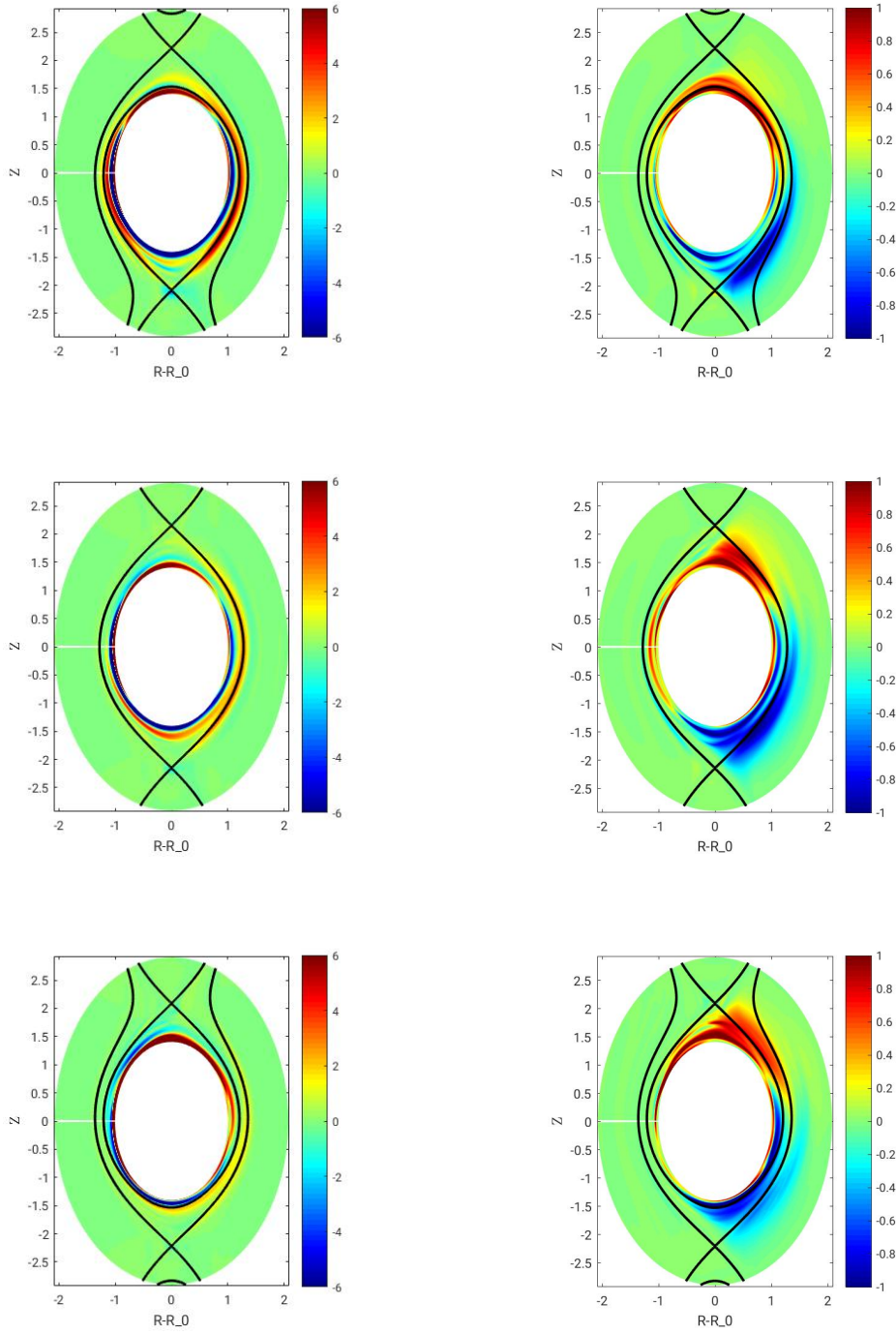
Figure 4.12 – Poloidal $E \times B$ flux components: $\bar{\Gamma}_E^\chi$ (left) and $\tilde{\Gamma}_E^\chi$ (right). The turbulent component of the flux is more important than the mean field contribution in the LFS common flux region, whilst in the interseparatrix region the turbulent and equilibrium fluxes are comparable.
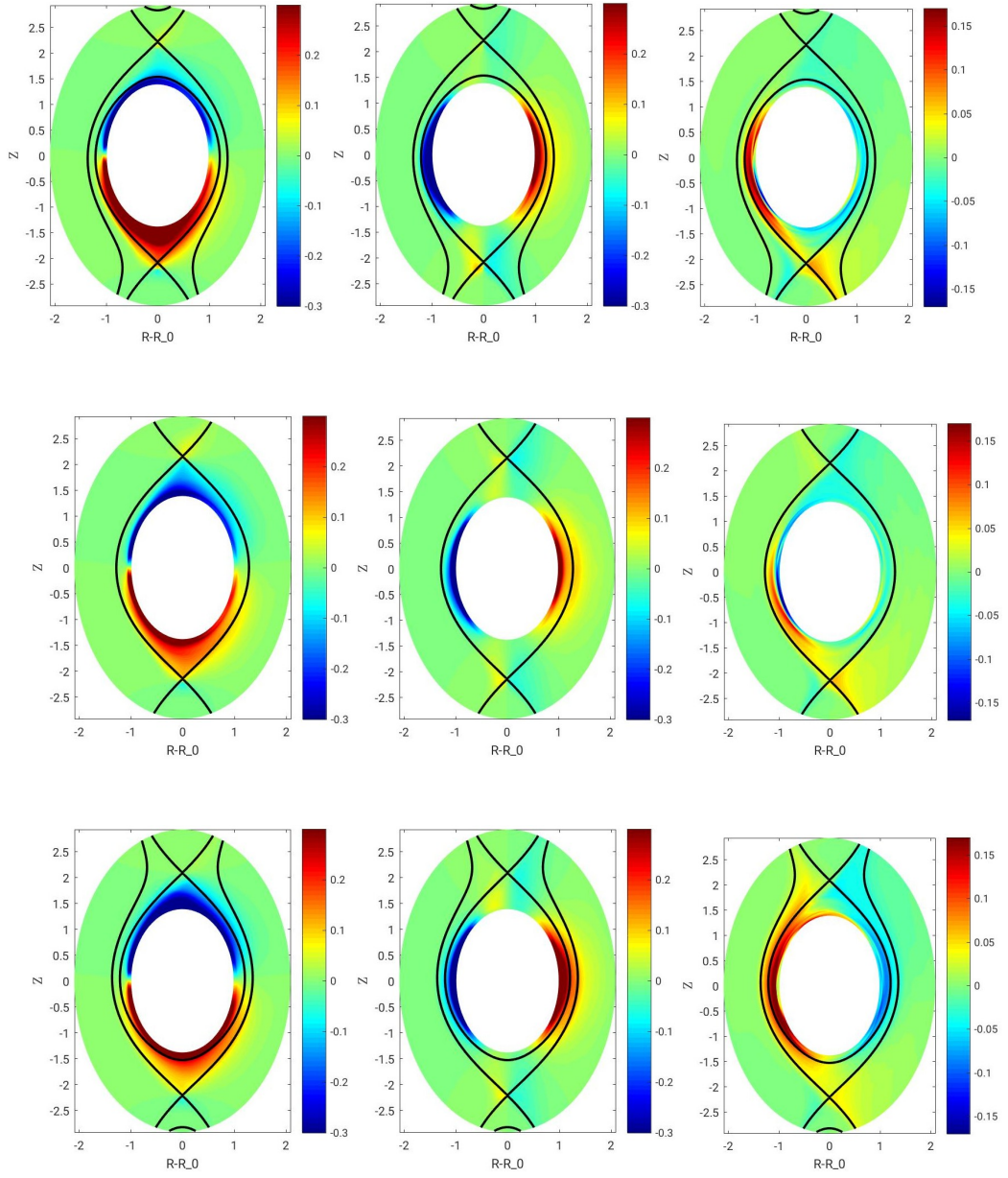
Figure 4.13 – Left to right $\bar{\Gamma}_*^\rho$, $\bar{\Gamma}_*^\chi$ and $\bar{\Gamma}_\parallel$. The turbulent components of the flux are much less important than the mean field contribution in both ρ and χ directions so are not shown. The radial component of the diamagnetic flux acts as a source of plasma to the ISR in the lower half and a sink in the upper half. The stagnation point of $\bar{\Gamma}_\parallel$ in the ISR is below the outer midplane in both the LSN and USN configurations.

where l and u refer to the lower and upper divertors, δR_{sep} is the distance between the two separatrices at the midplane and L_{pe} is the pressure decay length at the outer midplane [10]. In our simulations, $\delta R_{\text{sep}} = 23, 0, -23 \rho_{s0}$ for the USN, balanced DN and LSN configurations respectively. Following the model in Ref. [10], we fit a single density decay length at the midplane, which appears to be a good fit to the density decay in these simulations. The pressure decay length is related to the density decay length by $L_{pe} = L_n/(1 + \eta) = 51\rho_{s0}$ where $\eta = L_n/L_{T_e} \approx 0.77$ as described in Chapter 3. Substituting these numbers into Eq. 4.34 predicts the fractional differences in the heat load as $-0.22, 0, 0.22$ whilst in the simulations we find $-0.18, -0.05, 0.07$. Hence, the fractional difference in the heat flux in our simulations is less than expected from the model in Ref. [10]. In addition the heat flux to the upper and lower LFS legs is not equal in the balanced DN configuration.

To understand why this difference arises, we consider the time and toroidally averaged parallel, diamagnetic and $E \times B$ fluxes, which are plotted in the poloidal plane in the magnetic coordinate $(\rho - \chi)$ directions in Figs. 4.11, 4.12 and 4.13. We note that the diamagnetic and $E \times B$ fluxes are not considered in the model in Ref. [10].

For the balanced case, as expected, we find the main fluxes are the turbulent $E \times B$ flux across the LCFS and the parallel flow to the wall. The stagnation point of the parallel flow lies close to the outer midplane, and there is little $E \times B$ flow across the midplane, however the up-down symmetry is broken by the diamagnetic flux. Since $\Gamma_* = -\mathbf{b} \times \nabla p_e c/(eB)$ goes in the downwards direction for a pressure gradient mostly in the ∇R direction, as is the case on the LFS, the diamagnetic flux acts as a sink of plasma in the upper half of the LFS domain and a source in the lower half resulting in a greater heat flux to the lower leg, as shown in Fig. 4.10. The difference in heating power to the upper and lower outer legs is consistent with an order of magnitude estimate of the diamagnetic heat flux.

In the LSN and USN, the plasma dynamics are complicated by the existence of the interseparatrix region, in which two competing flow effects that are not accounted for in the model of Ref. [10] are at play. The first is that the stagnation point of $v_{\parallel e}$ is below the midplane in the ISR for both LSN and USN simulations, so the parallel flow at the midplane goes upwards in both cases. We observe the greatest divergence of the parallel heat flux in the part of the ISR just below the midplane, particularly in the LSN configuration. In the LSN configuration, the turbulent radial flow across the LCFS is also strongest here (see Fig. 4.11). In the USN, the upwards parallel flow is exhausted on the upper LFS, whilst in the LSN it goes towards the HFS lower leg. The second effect is the downwards equilibrium $E \times B$ flow in the ISR, resulting from the inwards electric field across the ISR (see Fig. 4.8). The inwards electric field results because $\phi \simeq \Lambda T_e$ [49] and T_e increases across the midplane from the wall towards the second separatrix, whilst in the closed flux region $\phi < 0$, implying a peak in ϕ near the second separatrix an inwards electric field across the ISR, as observed in Fig. 4.8.

In the LSN configuration, the downwards $E \times B$ flow across the $y = L_y/2$ surface is greater than the parallel flow across this surface in the opposite direction, resulting in a greater heat

flux to the lower leg. Conversely, in the USN configuration there remains a downwards $E \times B$ flow across the outer midplane, however it is less that the upwards parallel flow, resulting in a greater heat flux to the upper leg. The weaker $E \times B$ flow results from ϕ being less strongly peaked on the outer separatrix than in the LSN configuration.

We observe a more equal heat flux sharing in the balanced DN and USN configurations than in the LSN configuration, which is advantageous in terms of reducing the peak heat load to the divertor plates. It is also interesting that the additional flow effects not included in the model of Ref. [10] result in a more equal heat flux sharing in the unbalanced configurations, again a desirable result.

In Refs. [70] and [16], a greater heat flux was measured on the lower LFS divertor leg than the upper leg in a balanced configuration, as is also observed in our simulations. However, the direction of the toroidal magnetic field is reversed in these experiments compared to our simulations. In Ref. [70] the higher heat flux at the lower leg is interpreted in terms of the $E \times B$ flow. In their experiments, the $E \times B$ flow went from the lower outer to lower inner leg, and upper inner to upper outer leg, resulting in a higher particle flow at the upper outer compared to the lower outer leg. Coupled with the assumption of constant pressure along field lines, this leads to a higher temperature at the lower outer compared to the upper outer leg, leading to a higher heat flux at the lower outer leg. In contrast, in our simulations, the $E \times B$ drift across the private flux regions is weak compared to the stronger drifts around the midplane, which could explain the difference in our results.

5 Summary and conclusions

In this work we leverage the recent upgrade to GBS to use geometric coordinates to make significant progress towards first-principles predictions of plasma transport in SOL in DN magnetic configurations. In Chapter 2, the physical model, based on the drift-reduced Braginskii equations, is present and its implementation in the GBS code described.

In Chapter 3 we present the results of a set of simulations in a balanced double null configuration in which the resistivity and safety factor are varied. We explain the origins of the up-down and LFS-HFS asymmetries. We focus on the density decay at the outer mid-plane, which we find to have two decay lengths. We develop a model to predict the two density decay lengths observed in the simulations. In the near SOL, we use an approach based on the saturation of linear instabilities, whilst in the far SOL we consider blob transport. The final results reveal the dependencies of the two scale lengths on the resistivity, safety factor and major radius.

In Chapter 4, we turn our attention to unbalanced double null configurations, used a further code upgrade to use an elliptical coordinate system in the poloidal plane. This permits the simulations of magnetic configurations with more realistic elongation. We focus on the heat flux sharing between the four divertor legs, finding the more equal sharing in a balanced or USN configuration compared to a LSN configuration. This result is explained in terms of the $E \times B$, diamagnetic and parallel drifts.

One of the main advantages of a DN magnetic configurations that has not been considered in this thesis is the possibility of increased radiative losses due to the presence of two X points [73]. Future simulations including neutrals would therefore be greatly useful to decide if a DN configuration is preferable to SN in terms of the heat load dissipation in the SOL.

In addition, simulating balanced and unbalanced double null configurations including the core region, using the code upgrade presented in Ref. [33] could give important insights into the interplay between turbulence in the edge and in the SOL. Finally, it has been shown that the ion pressure can play an important role in the formation of $E \times B$ shear near the LCFS [101], so the inclusion of finite ion temperature would also be an interesting continuation of

this work.

Bibliography

[1] Patrick R. Amestoy et al. "A fully asynchronous multifrontal solver using distributed dynamic scheduling". In: *SIAM Journal on Matrix Analysis and Applications* 23.1 (2002), pp. 15–41.

[2] Patrick R. Amestoy et al. "Hybrid scheduling for the parallel solution of linear systems". In: *Parallel Computing*. Vol. 32. 2. North-Holland, 2006, pp. 136–156.

[3] J Ball, J and Parisi. *The Future of Fusion Energy*. London: World Scientific Publishing Europe Ltd, 2018.

[4] Camille Baudoin et al. "Turbulent heat transport in TOKAM3X edge plasma simulations". In: *Contributions to Plasma Physics* 58.6-8 (2018), pp. 484–489.

[5] Carrie F. Beadle and Paolo Ricci. "Understanding the turbulent mechanisms setting the density decay length in the tokamak scrape-off layer". In: *Journal of Plasma Physics* 86.1 (2020).

[6] Thomas Body et al. "Treatment of advanced divertor configurations in the flux-coordinate independent turbulence code GRILLIX". In: *Contributions to Plasma Physics* 60.5-6 (2020).

[7] J. A. Boedo et al. "Edge transport studies in the edge and scrape-off layer of the National Spherical Torus Experiment with Langmuir probes". In: *Physics of Plasmas* 21.4 (2014), p. 042309.

[8] J. A. Boedo et al. "Transport by intermittency in the boundary of the DIII-D tokamak". In: *Physics of Plasmas* 10.5 (2003), pp. 1670–1677.

[9] S I Braginskii. "Transport Processes in a Plasma". In: *Reviews of Plasma Physics* (1965).

[10] D. Brunner et al. "The dependence of divertor power sharing on magnetic flux balance in near double-null configurations on Alcator C-Mod". In: *Nuclear Fusion* 58.7 (2018), p. 076010.

[11] D. Carralero et al. "Experimental Validation of a Filament Transport Model in Turbulent Magnetized Plasmas". In: *Physical Review Letters* 115.21 (2015), p. 215002.

[12] D. Carralero et al. "Recent progress towards a quantitative description of filamentary SOL transport". In: *Nuclear Fusion* 57.5 (2017), p. 056044.

[13]   C. S. Chang et al. "Fast Low-to-High Confinement Mode Bifurcation Dynamics in a Tokamak Edge Plasma Gyrokinetic Simulation". In: *Physical Review Letters* 118.17 (2017), p. 175001.

[14]   D. A. D'Ippolito, J. R. Myra, and S. J. Zweben. "Convective transport by intermittent blob-filaments: Comparison of theory and experiment". In: *Physics of Plasmas* 18.6 (2011), p. 060501.

[15]   David Mackay. *Sustainable Energy without the Hot Air.* Cambridge: UIT Cambridge Ltd, 2009.

[16]   G. De Temmerman et al. "Heat load asymmetries in MAST". In: *Journal of Nuclear Materials.* Vol. 415. 1 SUPPL. Elsevier B.V., 2011, S383–S386.

[17]   M. A. Dorf et al. "Progress with the COGENT Edge Kinetic Code: Collision Operator Options". In: *Contributions to Plasma Physics* 52.5-6 (2012), pp. 518–522.

[18]   B D Dudson et al. "BOUT++: Recent and current developments". In: *J. Plasma Physics* 81 (2015), p. 365810104.

[19]   B.D. Dudson et al. "BOUT++: A framework for parallel plasma fluid simulations". In: *Computer Physics Communications* 180.9 (2009), pp. 1467–1480.

[20]   L. Easy et al. "Investigation of the effect of resistivity on scrape off layer filaments using three-dimensional simulations". In: *Physics of Plasmas* 23.1 (2016), p. 012512.

[21]   L. Easy et al. "Three dimensional simulations of plasma filaments in the scrape off layer: A comparison with models of reduced dimensionality". In: *Physics of Plasmas* 21.12 (2014), p. 122515.

[22]   F. Militello and J. T. Omotani. "On the relation between non-exponential scrape off layer profiles and the dynamics of filaments". In: *Plasma Physics and Controlled Fusion* 58.12 (2016).

[23]   D. M. Fan et al. "Effect of turbulent fluctuations on neutral particles transport with the TOKAM3X-EIRENE turbulence code". In: *Nuclear Materials and Energy* 18 (2019), pp. 105–110.

[24]   D.-M. Fan et al. "Self-consistent coupling of the three-dimensional fluid turbulence code TOKAM3X and the kinetic neutrals code EIRENE". In: *Contributions to Plasma Physics* 58.6-8 (2018), pp. 490–496.

[25]   N. Fedorczak et al. "A spectral filament model for turbulent transport and scrape off layer width in circular geometry". In: *Nuclear Materials and Energy* 19 (2019), pp. 433–439.

[26]   M. Francisquez, B. Zhu, and B. N. Rogers. "Global 3D Braginskii simulations of the tokamak edge region of IWL discharges". In: *Nuclear Fusion* 57.11 (2017).

[27]   G Fuchert et al. "Towards a quantitative prediction of the blob detection rate". In: *Plasma Physics and Controlled Fusion* 58.5 (2016), p. 054006.

[28] I. Furno et al. "Experimental Observation of the Blob-Generation Mechanism from Interchange Waves in a Plasma". In: *Physical Review Letters* 100.5 (2008), p. 055004.

[29] D. Galassi et al. "Drive of parallel flows by turbulence and large-scale E × B transverse transport in divertor geometry". In: *Nuclear Fusion* 57.3 (2017), p. 036029.

[30] D. Galassi et al. "Flux expansion effect on turbulent transport in 3D global simulations". In: *Nuclear Materials and Energy* 12 (2017), pp. 953–958.

[31] Davide Galassi et al. "Tokamak edge plasma turbulence interaction with magnetic X-point in 3D global simulations". In: *Fluids* 4.1 (2019).

[32] A Gallo et al. "Impact of the plasma geometry on divertor power exhaust: experimental evidence from TCV and simulations with SolEdge2D and TOKAM3X". In: *Plasma Physics and Controlled Fusion* 60.1 (2018), p. 014007.

[33] M. Giacomin and P. Ricci. "Investigation of turbulent transport regimes in the tokamak edge by using two-fluid simulations". In: *Journal of Plasma Physics* 86.5 (2020), p. 905860502.

[34] Maurizio Giacomin, Louis Stenger, and Paolo Ricci. "Turbulence and flows in the plasma boundary of snowflake magnetic configurations". In: *Nuclear Fusion* (2020).

[35] R. Häcker et al. "Estimation of the plasma blob occurrence rate". In: *Physics of Plasmas* 25.1 (2018), p. 012315.

[36] F D Halpern et al. "The GBS code for tokamak scrape-off layer simulations". In: *Journal of Computational Physics* 315 (2016), pp. 388–408.

[37] F.D. Halpern and P. Ricci. "Velocity shear, turbulent saturation, and steep plasma gradients in the scrape-off layer of inner-wall limited tokamaks". In: *Nuclear Fusion* 57.3 (2017), p. 034001.

[38] F.D. Halpern et al. "Theory of the scrape-off layer width in inner-wall limited tokamak plasmas". In: *Nuclear Fusion* 54.4 (2014), p. 043003.

[39] F.D. Halpern et al. "Theory-based scaling of the SOL width in circular limited tokamak plasmas". In: *Nuclear Fusion* 53.12 (2013), p. 122001.

[40] Federico D Halpern et al. "Outer midplane scrape-off layer profiles and turbulence in simulations of Alcator CMod inner-wall limited discharges". In: *Physics of Plasmas* (2017).

[41] M Hariri, Farah and Ottaviani. "A Flux Coordinate Independent Field-Aligned Approach to Plasma Turbulence Simulations". In: *Computer Physics Communications* (2013).

[42] J Horacek et al. "Multi-machine scaling of the main SOL parallel heat flux width in tokamak limiter plasmas". In: *Plasma Physics and Controlled Fusion* 58.7 (2016), p. 074005.

[43] *International Energy Outlook 2019*. Tech. rep. US Energy Information Administration, 2019.

[44] Sébastien Jolliet et al. "Aspect ratio effects on limited scrape-off layer plasma turbulence". In: *Physics of Plasmas* 21.2 (2014), p. 022303.

[45] A.Q. Kuang et al. "Plasma fluctuations in the scrape-off layer and at the divertor target in Alcator C-Mod and their relationship to divertor collisionality and density shoulder formation". In: *Nuclear Materials and Energy* 19 (2019), pp. 295–299.

[46] A. S. Kukushkin et al. "Finalizing the ITER divertor design: The key role of SOLPS modeling". In: *Fusion Engineering and Design* 86.12 (2011), pp. 2865–2873.

[47] B. LaBombard et al. "High-field side scrape-off layer investigation: Plasma profiles and impurity screening behavior in near-double-null configurations". In: *Nuclear Materials and Energy* 12 (2017), pp. 139–147.

[48] A Loarte et al. "Chapter 4: Power and particle control". In: *Nuclear Fusion* 47.6 (2007), S203–S263.

[49] J Loizu. "The role of the sheath in magnetized plasma turbulence and flows". PhD thesis. EPFL, 2013.

[50] J Loizu et al. "On the electrostatic potential in the scrape-off layer of magnetic confinement devices". In: *Plasma Physics and Controlled Fusion* 55.12 (2013), p. 124019.

[51] J. Loizu et al. "Boundary conditions for plasma fluid models at the magnetic presheath entrance". In: *Physics of Plasmas* 19.12 (2012), p. 122307.

[52] P. Manz et al. "Magnetic configuration effects on the Reynolds stress in the plasma edge". In: *Physics of Plasmas* 25.7 (2018), p. 072508.

[53] G F Matthews et al. "Overview of the ITER-like wall project". In: *Physica Scripta* 2007.T128 (2007), p. 137.

[54] R. M. McDermott et al. "Edge radial electric field structure and its connections to H-mode confinement in Alcator C-Mod plasmas". In: *Physics of Plasmas*. Vol. 16. 5. American Institute of PhysicsAIP, 2009, p. 056103.

[55] A Mosetto. "Turbulent regimes in the tokamak scrape-off layer". PhD thesis. EPFL, 2014.

[56] Annamaria Mosetto et al. "Finite ion temperature effects on scrape-off layer turbulence". In: *Physics of Plasmas* 22.1 (2015), p. 012308.

[57] Annamaria Mosetto et al. "Finite ion temperature effects on scrape-off layer turbulence". In: *Physics of Plasmas* 22.1 (2015), p. 012308.

[58] Annamaria Mosetto et al. "Low-frequency linear-mode regimes in the tokamak scrape-off layer". In: *Physics of Plasmas* 19.11 (2012), p. 112103.

[59] Annamaria Mosetto et al. "Turbulent regimes in the tokamak scrape-off layer". In: *Physics of Plasmas* 20.9 (2013), p. 092308.

[60] S H Müller et al. "Studies of blob formation, propagation and transport mechanisms in basic experimental plasmas (TORPEX and CSDX)". In: *Plasma Physics and Controlled Fusion* 51.5 (2009), p. 055020.

[61]   J. R. Myra, D. A. Russell, and D. A. D'Ippolito. "Collisionality and magnetic geometry effects on tokamak edge turbulent transport. I. A two-region model with application to blobs". In: *Physics of Plasmas* 13.11 (2006).

[62]   F Nespoli et al. "Blob properties in full-turbulence simulations of the TCV scrape-off layer". In: *Plasma Physics and Controlled Fusion* 59.5 (2017), p. 055009.

[63]   F. Nespoli et al. "Non-linear simulations of the TCV Scrape-Off Layer". In: *Nuclear Materials and Energy* 12 (2017), pp. 1205–1208.

[64]   F. Nespoli et al. "Understanding and suppressing the near scrape-off layer heat flux feature in inboard-limited plasmas in TCV". In: *Nuclear Fusion* 57.12 (2017), p. 126029.

[65]   A. H. Nielsen et al. "Simulation of transition dynamics to high confinement in fusion plasmas". In: *Physics Letters, Section A: General, Atomic and Solid State Physics* 379.47-48 (2015), pp. 3097–3101.

[66]   Q. Pan et al. "Full-f version of GENE for turbulence in open-field-line systems". In: *Physics of Plasmas* 25.6 (2018), p. 062303.

[67]   Paola Paruta. "Simulation of plasma turbulence in the periphery of diverted tokamaks". PhD thesis. EPFL, 2018.

[68]   Paola Paruta et al. "Blob velocity scaling in diverted tokamaks: A comparison between theory and simulation". In: *Physics of Plasmas* 26.3 (2019).

[69]   Paola Paruta et al. "Simulation of plasma turbulence in the periphery of diverted tokamak by using the GBS code". In: *Physics of Plasmas* 25.11 (2018), p. 112301.

[70]   T. W. Petrie et al. "The effect of divertor magnetic balance on H-mode performance in DIII-D". In: *Journal of Nuclear Materials* 290-293 (2001), pp. 935–939.

[71]   M. Podestà et al. "Cross-field transport by instabilities and blobs in a magnetized toroidal plasma". In: *Physical Review Letters* 101.4 (2008), pp. 16–19.

[72]   F. M. Poli et al. "Transition from drift to interchange instabilities in an open magnetic field line configuration". In: *Physics of Plasmas* 15.3 (2008).

[73]   R.Wenninger et al. "Power Handling and Plasma Protection Aspects that affect the Design of the DEMO Divertor and First Wall". In: *IAEA Conference Proceedings* (2016).

[74]   P. Ricci et al. "Simulation of plasma turbulence in scrape-off layer conditions: The GBS code, simulation results and code validation". In: *Plasma Physics and Controlled Fusion* 54.12 (2012).

[75]   Paolo Ricci and B. N. Rogers. "Plasma turbulence in the scrape-off layer of tokamak devices". In: *Physics of Plasmas* 20.1 (2013).

[76]   Paolo Ricci, B. N. Rogers, and S. Brunner. "High- and Low-Confinement Modes in Simple Magnetized Toroidal Plasmas". In: *Physical Review Letters* 100.22 (2008), p. 225002.

[77]   Fabio Riva et al. "Plasma shaping effects on tokamak scrape-off layer turbulence". In: *Plasma Physics and Controlled Fusion* 59.3 (2017), p. 035001.

[78]   Fabio Riva et al. "Three-dimensional plasma edge turbulence simulations of the Mega Ampere Spherical Tokamak and comparison with experimental measurements". In: *Plasma Physics and Controlled Fusion* 61.9 (2019), p. 095013.

[79]   Fabio Riva et al. "Verification methodology for plasma simulations and application to a scrape-off layer turbulence code". In: *Physics of Plasmas* (2014).

[80]   B. N. Rogers and W. Dorland. "Noncurvature-driven modes in a transport barrier". In: *Physics of Plasmas* 12.6 (2005), pp. 1–12.

[81]   A. Ross et al. "On the nature of blob propagation and generation in the large plasma device: Global GRILLIX studies". In: *Physics of Plasmas* 26.10 (2019), p. 102308.

[82]   Alexander Ross, Andreas Stegmeir, and David Coster. "Effect of the Boussinesq approximation: Turbulence studies with GRILLIX in slab geometry". In: *Contributions to Plasma Physics* 58.6-8 (2018), pp. 478–483.

[83]   D. A. Russell, J. R. Myra, and D. A. D'Ippolito. "Collisionality and magnetic geometry effects on tokamak edge turbulent transport. II. Many-blob turbulence in the two-region model". In: *Physics of Plasmas* 14.10 (2007), p. 102307.

[84]   J Schirmer et al. "The radial electric field and its associated shear in the ASDEX Upgrade tokamak". In: *Nuclear Fusion* 46.9 (2006), S780–S791.

[85]   D. Schwörer et al. *Dynamics of scrape-off layer filaments in detached conditions.* 2019.

[86]   D. Schwörer et al. "Influence of plasma background including neutrals on scrape-off layer filaments using 3D simulations". In: *Nuclear Materials and Energy* 12 (2017), pp. 825–830.

[87]   Bruce D Scott. "Three-dimensional computation of drift Alfvén turbulence". In: *Plasma Physics and Controlled Fusion* 39 (1997), p. 1635.

[88]   E. L. Shi et al. "Full-f gyrokinetic simulation of turbulence in a helical open-field-line plasma". In: *Physics of Plasmas* 26.1 (2019), p. 012307.

[89]   E. L. Shi et al. "Gyrokinetic continuum simulation of turbulence in a straight open-field-line plasma". In: *Journal of Plasma Physics* 83.3 (2017), p. 905830304.

[90]   A. Stegmeir et al. "Global turbulence simulations of the tokamak edge region with GRILLIX". In: *Physics of Plasmas* 26.5 (2019), p. 052517.

[91]   Andreas Stegmeir et al. "GRILLIX: a 3D turbulence code based on the flux-coordinate independent approach". In: *Plasma Physics and Controlled Fusion* 60.3 (2018), p. 035005.

[92]   P. Tamain et al. "The TOKAM3X code for edge turbulence fluid simulations of tokamak plasmas in versatile magnetic geometries". In: *Journal of Computational Physics* 321 (2016), pp. 606–623.

[93]   William Morris Tony Donné. *European Research Roadmap to the Realisation of Fusion Energy.* 2018.

[94]   C. K. Tsui et al. "Filamentary velocity scaling validation in the TCV tokamak". In: *Physics of Plasmas* 25.7 (2018).

[95] Nicola Vianello et al. "Scrape Off Layer (SOL) transport and filamentary characteristics in high density tokamak regimes". In: *Nuclear Fusion* (2019).

[96] N R Walkden et al. "Identification of intermittent transport in the scrape-off layer of MAST through high speed imaging". In: *Nuclear Materials and Energy* 12 (2016), pp. 175–180.

[97] N R Walkden et al. "Interpretation of scrape-off layer profile evolution and first-wall ion flux statistics on JET using a stochastic framework based on fillamentary motion". In: *Plasma Physics and Controlled Fusion* 59.8 (2017), p. 085009.

[98] A Zeiler. *Tokamak Edge Turbulence*. Max-Planck-Institut fur Plasmaphysik, 1999.

[99] W. Zholobenko et al. "Thermal dynamics in the flux-coordinate independent turbulence code GRILLIX". In: *Contributions to Plasma Physics* 60.5-6 (2020), e201900131.

[100] Ben Zhu, Manaure Francisquez, and Barrett N. Rogers. "GDB: A global 3D two-fluid model of plasma turbulence and transport in the tokamak edge". In: *Computer Physics Communications* 232 (2018), pp. 46–58.

[101] Ben Zhu, Manaure Francisquez, and Barrett N. Rogers. " Global 3D two-fluid simulations of the tokamak edge region: Turbulence, transport, profile evolution, and spontaneous E × B rotation ". In: *Physics of Plasmas* 24.5 (2017), p. 055903.

[102] Ben Zhu, Manaure Francisquez, and Barrett N. Rogers. "Up-down symmetry breaking in global tokamak edge simulations". In: *Nuclear Fusion* 58.10 (2018), p. 106039.

[103] H. Zohm et al. "On the physics guidelines for a tokamak DEMO". In: *Nuclear Fusion* 53.7 (2013), p. 073019.

Acknowledgements

First of all I would like to thank my thesis supervisor Paolo Ricci. Thank you for welcoming me into the field of plasma physics, about which I knew almost nothing when I came to SPC, and for your availability and enthusiasm to discuss my work during these four years. Your vast knowledge and open-mindedness to go in different directions have been essential for the completion of this thesis.

I would like to thank the other members of this group. First, thanks to Fabio for being great to work with on my internship project and motivating me to come back for a PhD! Huge thanks are due to Fabio, Christoph and Jorge for helping me with countless GBS issues, especially in the beginning. I'd like to thank Paola, my first officemate, for her great patience teaching me to run GBS, the matlab scripts and blob analysis routines, but moreover for being an all around fantastic human being and a great source of inspiration! I'd also like to thank Andre, with whom I've shared an office the past two years, for your enduring sense of humour and tales of cycling (mis)adventures.

I'd like to thank Sebastien Morel, with whom I worked with on the elliptical coordinates part of this project, your diligence and enthusiasm paid off and your contribution to this thesis was hugely helpful. Thank you. I'd also like to thank Maurizio and Baptiste for answering various questions on GBS, plasma physics, French language (in particular the abstract of this thesis), places to go hiking...

Thanks to Cedric Tsui and Olivier Fevrier for imparting your wisdom on all things experimental. Though the experimental comparison part of the project was not very successful, it was nonetheless very interesting to learn how things work beyond the world of simulations...

Thanks to all the other PhD students at SPC for making it a great place to work. The supportive atmosphere is one of the best things about working here, especially during the doctoral courses, such a collaborative approach to studying was new for me and a great experience. I'd also like to thank the other researchers, especially those who taught the doctoral courses, to Edith and Roxanne for their help with the administrative tasks and to Nathalie Ritter for her

invaluable advice.

I'd also like to thank my previous teachers and mentors: Dr Lester for being quite simply the best physics and maths supervisor imaginable, Dr Julia Riley for making the most basic parts of undergraduate physics come (literally) to life and later being a fantastic tutor and to Andrew Kavanagh and Mervyn Freeman for making my first experiences of research exciting enough to follow this path.

I feel it'd be amiss not to mention my climbing partners, in particular Aurelie, who have helped me keep the whole PhD process in perspective. We've shared the most incredible experiences, beyond anything I could previously have imagined. Thanks to Joe, for being hugely supportive during the writing up and vanishing any thesis-related misery like clouds on a sunny day. Finally I'd like to thank my family, who have also put a huge amount of effort as well as some unconventional wisdom into the completion of this PhD. Anything I write here will be cheesier than a Swiss fondue so I'll just leave it at: you're the best!

Lausanne, 09 Oct 2020   Carrie Beadle

+41 779622950

carrie.beadle@epfl.ch

Carrie Beadle

Experience

PhD student, Swiss Plasma Center, EPFL. September 2016 - November 2020

      Research in plasma physics using numerical simulations

      Teaching assistant for plasma physics and general physics courses

      Supervision of a master level student

Research Intern at Swiss Plasma Center, EPFL. June – September 2015

Summer Student at British Antarctic Survey, Cambridge. June – August 2014

Summer Student at British Antarctic Survey, Cambridge. July – September 2013

Education

MSc Physics, 2.1. University of Cambridge, 2015-2016. Master project on geophysical fluid dynamics with Dr. Jerome Neufeld.

BA Natural Sciences – Physical, 1st. University of Cambridge, 2012-2015

Languages

English (native), French (B2), German (A2)

Journal publications

- C. Beadle and P. Ricci. "Understanding the turbulent mechanisms setting the density decay length in the tokamak scrape-off layer." *Journal of Plasma Physics (2020)*
- P. Paruta, C. Beadle, P. Ricci, C. Theiler. "Blob velocity scaling in diverted tokamaks: A comparison between theory and simulation." *Physics of Plasmas (2019)*
- P. Paruta, P. Ricci, F. Riva, C. Wersal, C. Beadle, B. Frei. "Simulation of plasma turbulence in the periphery of diverted tokamak by using the GBS code." *Physics of Plasmas (2018)*
- F. Riva, C. Beadle, P. Ricci. "A methodology for the rigorous verification of Particle-in-Cell simulations." *Physics of Plasmas (2017)*

Conference participation

- C. Beadle, P. Ricci, P. Paruta, A. Calado, M. Giacomin, B. Frei. "Disentangling turbulence, transport and blobs in the periphery of double-null tokamak configurations" *Invited presentation at the 61st Annual Meeting of the APS Division of Plasma Physics. Fort Lauderdale, FL, 2019*
- C. Beadle, P. Ricci, P. Paruta. « Scrape-off layer simulations in a Double Null magnetic configuration." *Poster presented at Joint EU-US Transport Task Force Meeting. Seville, Spain, 2018*
- C. Beadle, P. Ricci, P. Paruta, F. Riva, C. Wersal. "Scrape-off layer simulations in a Double Null magnetic configuration." *Oral presentation at the European Fusion Theory Conference. Athens, Greece, 2017.*

83

Interests

Alpinism, ski touring, environmental activism, organising sports events.